2016

Contributions of cluster shape and intercellular adhesion to epithelial discohesion and emergent dynamics in collective migration

BOSTON UNIVERSITY

COLLEGE OF ENGINEERING

Dissertation

CONTRIBUTIONS OF CLUSTER SHAPE AND INTERCELLULAR ADHESION TO EPITHELIAL DISCOHESION AND EMERGENT DYNAMICS IN COLLECTIVE MIGRATION

by

DIEGO ALEJANDRO VARGAS ARANGO

B.S., University of Texas at Austin, 2009
M.S., Boston University, 2014

Submitted in partial fulfillment of the

requirements for the degree of

Doctor of Philosophy

2016

Approved by

First Reader

Muhammad H. Zaman, PhD
Professor of Biomedical Engineering
Professor, Howard Hughes Medical Institute

Second Reader

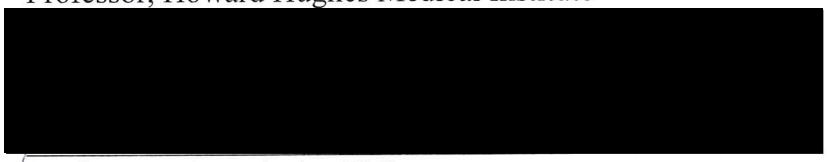

Maria A. Kukuruzinska, PhD
Associate Dean of Research
Professor of Molecular and Cell Biology
Henry M. Goldman School of Dental Medicine

Research Assistant Professor of Biochemistry
School of Medicine

Third Reader

James E. Galagan, PhD
Associate Professor of Biomedical Engineering

Associate Professor of Microbiology
School of Medicine

Fourth Reader

Béla Suki, PhD
Professor of Biomedical Engineering

Fifth Reader

Xaralabos G. Varelas, PhD
Assistant Professor of Biochemistry
School of Medicine

DEDICATION

A muchos Arango, unos Vargas,

un Imširović, una Kohen,

un Rajalingham, una Sharma,

un calvo y una chinchilla.

Sin ustedes no habría tenido la fortaleza.

ACKNOWLEDGEMENTS

My advisors, Dr. Muhammad Zaman and Dr. Maria Kukuruzinska, were fundamental to the development of this work. This work began as suggestion by Dr. Zaman, who pointed me towards the first studies on collective migration. It was also through him that I met Dr. Kukuruzinska. She was patient and incredibly persistent while I became acquainted with the minutiae of the N-glycosylation and Wnt signaling pathways. As a source of knowledge, she always lent a critical eye to check most theoretical results. Countless times they directed me in the direction of useful conversations and collaborations.

Some people were integral on the technical side of the work. On the computational work, Dr. Harikrishnan Parameswaran provided valuable information on sensitivity analysis and other analytical tools. Dr. Sam Isaacson in the Mathematics Department was very helpful through discussions on non-linear dynamics. Dr. Kadin Tseng from the Scientific Computing and Visualization group was very helpful in setting up the parallel computing simulations in the shared computer cluster.

Close collaborators included Dr. Oliver Bates and Dr. Yasha Sharma. Alongside me, Dr. Bates developed the epithelial to mesenchymal model. He taught me the basics of object oriented programming and setting up programming libraries. Dr. Sharma developed the protocol to grow clusters, and we had the first discussions on developing the multiscale cluster model. With her dedication and thoroughness, she was fundamental in analyzing the data and arriving to the major conclusions in this work. Along with them, many lab mates deserve recognition: Alex Bloom, Trevor Packer, Khalid Alamoud,

and Khikmet Sadykov for their help mastering immunoblotting and immunoprecipitation. Meng Sun came along for the ride and met many dead ends analyzing the biochemical pathway numerical description and took part of many valuable conversations.

Finally, the rest of the thesis committee, Dr. Bela Suki and Dr. James Galagan, were very helpful through conversations along the way. Dr. Suki was always available and suggested many alternatives to handle a large non-linear system. Dr. Galagan was very insightful and put results in perspective. Along with them Dr. Michael Smith and Dr. Parameswaran provided additional discussions on the value of the work and how to direct it.

CONTRIBUTIONS OF CLUSTER SHAPE AND

INTERCELLULAR ADHESION TO EPITHELIAL DISCOHESION AND

EMERGENT DYNAMICS IN COLLECTIVE MIGRATION

DIEGO ALEJANDRO VARGAS ARANGO

Boston University, College of Engineering, 2016

Major Professor: Muhammad H. Zaman, Ph.D., Professor of Biomedical Engineering, Professor, Howard Hughes Medical Institute

ABSTRACT

As a physical system, a cell interacts with its environment through physical and chemical processes. The cell can change these interactions through modification of its environment or its own composition. This dissertation presents the overarching hypothesis that both biochemical regulation of intercellular adhesion and physical interaction between cells are required to account for the emergence of cluster migration and collective dynamics observed in epithelial cells.

Collective migration is defined as the displacement of a group of cells with transient or permanent cell-cell contacts. One mode, cluster migration, plays an important role during embryonic development and in cancer metastasis. Despite its importance, collective migration is a slow process and hard to visualize, and therefore it has not been thoroughly studied in three dimensions (3D).

Based on known information about cluster migration from 2D studies of epithelial sheets and 3D single cell migration, this dissertation presents theoretical and experimental techniques to assess the independent contribution of physical and

biochemical factors to 3D cluster migration. It first develops two computational models that explore the interaction between cells and the ECM and epithelial discohesion. These discrete mechanistic models reveal the need to account for intracellular regulation of adherens junctions in space and time within a cluster. Consequently, a differential algebraic model is developed that accounts for cross-reactivity of three pathways in a regulatory biochemical network: Wnt/β-catenin signaling, protein N-glycosylation, and E-cadherin adhesion. The model is tested by matching predictions to Wnt/β-catenin inhibition in MDCK cells. The model is then incorporated into a self-propelled particle (SPP) model, creating the first SPP model for study of adhesive mammalian cellular systems.

MDCK cell clusters with fluorescent nuclei are grown, seeded, and tracked in 3D collagen gels using confocal microscopy. They provide data on individual cell dynamics within clusters. Borrowed from the field of complex systems, normalized velocity is used to quantify the order of both *in vitro* and simulated clusters. An analysis of sensitivity of cluster dynamics on factors describing physical and biochemical processes provides new quantitative insights into mechanisms underlying collective cell migration and explains temporal and spatial heterogeneity of cluster behavior.

Contents

List of Tables

List of Figures

List of Abbreviations

2D	-	Two dimensions
3D	-	Three dimensions
ABC	-	Active β-catenin
ADP	-	Adenomatous polyposis coli
AJ	-	Adherens junction
BDC	-	β-catenin destruction complex
CBP	-	Cyclic-AMP response element binding protein
CC	-	Constant cadherin concentration
CCM	-	Control conditioned media
CoM	-	Center of mass
CPM	-	Cellular Potts model
DAE	-	Differential algebraic equation
DC	-	Dynamic cadherin concentration
DMSO	-	Dimethyl sulfoxide
ECM	-	Extracellular matrix
EMT	-	Epithelial to mesenchymal transition
ER	-	Endoplasmic reticulum
ERC	-	Endocytic recycling compartment
FA	-	Focal adhesion
FACS	-	Fluorescent activated cell sorting

FOV	-	Field of view
FRP	-	Frizzled related protein
FTM	-	Force traction microscopy
GFP	-	Green fluorescent protein
GPT	-	Dolichol-P-dependent N-acetylglucosamine-1-phosphate-transferase
GSK	-	Glycogen synthase kinase
HF	-	High force
ID	-	Identifier
LLO	-	Lipid-linked oligosaccharide
LF	-	Low force
LRP	-	Lipoprotein receptor-related protein
LSA	-	Local sensitivity analysis
MDCK	-	Madin Darby canine kidney
MMP	-	Matrix metalloproteases
NLS	-	Nuclear localization signal
ODE	-	Ordinary differential equation
PBS	-	Phosphate buffered saline
PIV	-	Particle image velocimetry
PDE	-	Partial differential equation
RCN	-	Regulatory cell network
SDM	-	Squared displacement median
SPP	-	Self-propelled particle

TCF	-	T-cell factor
WCM	-	Wnt3a conditioned media

CHAPTER 1. Introduction

1.1 Problem Statement

Collective cell migration is a pervasive process in life. From slime mold coming together as a collective to follow the folic acid trail secreted by its prey (1) to human development where cell collectives form the tracheal and mammary ducts in the embryonic stage (2), a group of cells can distance itself from its neighbors to accomplish a myriad of objectives. Its pervasiveness in such distinct cell types demonstrates its relevance to sustain life, but also its complexity as cells communicate and navigate very different surroundings encompassing different physical and, in some cases, biochemical cues.

Complex motion patterns are also observed in simpler systems such as colloidal solutions and ferromagnetic spins (3, 4). Separating the contributions of physical interactions from the biochemical response by the individual cells is essential to understanding mechanisms central to our existence such as embryonic development, organ morphogenesis, emergence of tissue architecture, and wound healing. It is also important to understand when collective cell migration does not occur properly as in malformation diseases or cancer metastasis (5).

This dissertation focuses on collective migration of mammalian epithelial cells. After stroke and ischemic heart disease, cancers of the trachea, bronchus, and lung have the highest mortality rate in high-income countries (6). In 85-90% of cases, cancer in these structures occurs as carcinoma, cancer of the epithelium (7). Many epithelial and

cancer cell lines, both non-metastatic and metastatic, have been developed to study multiple aspects of epithelial cell behavior, including migration. This led to the development of *in vitro* and *in vivo* techniques to investigate pathways relevant to proliferation, invasion, and migration (2, 8, 9).

Furthermore, computational approaches have also been increasingly applied to study both tumor growth in the epithelium and dynamics of collective systems (10–12). Different scales define the architecture of the epithelial environment, including tissue, cellular, and molecular (intracellular and extracellular). Experimentally, these scales have been explored independently and some attempts have been made at probing two scales simultaneously (13, 14), but a comprehensive understanding is challenging due to technical limitations. Whereas computational approaches have been recognized as suitable to integrate experimental findings into a unifying model, the existing computational approaches do not fully acknowledge the contribution or impact of biological networks (13, 15).

Common to all instances of collective migration is the persistent physical and functional connection among cells (5). To study collective migration, bonds between cells must be considered. These bonds are also regulated by both physical and biochemical processes that regulate the force exerted between cells while their stability is determined by expression of regulatory proteins (16–18). This dissertation considers the internal biochemical regulation of cell adhesion molecules via a regulatory network of multiple pathways and the subsequent effect of molecular interactions between adhesion molecules in neighboring cells. By incorporating kinetics of regulatory biochemical

networks into existing computational models studying dynamics of multiple particle systems, this study provides a method to theoretically separate the contributions of physical and biochemical interactions to collective cell migration.

1.2 Hypothesis and Questions Addressed

This dissertation presents the overarching hypothesis that both biochemical regulation of intercellular adhesion and physical interaction between cells are required to account for the emergence of cluster migration and collective dynamics observed in epithelial cells

Specifically, the thesis addresses the following questions:

(i) *Does the geometry of a cell collective play a role in its interaction with the surroundings?* – Epithelial cells are found in a matrix of secreted extracellular molecules collectively known as the extracellular matrix (ECM). Because of the heterogeneous composition of the ECM, it interacts with cells in a dynamic manner and undergoes remodeling in response to physiological and environmental cues. By accounting for both chemical degradation of the matrix and changing physical interaction with changing cluster geometry, this work looks at the relative dependence of collective migration on these two factors through a mechanical numerical model.

(ii) *What drives the formation of cellular clusters?* – During physiological or pathological events, epithelial cells are first organized in stratified epithelium or in a tumor mass respectively. For the formation of clusters, cells have to disrupt these conformations by either detaching together or have collectives form from detached individuals. This work describes agent based simulations in 3D where cells are placed in a sheet and conditions

varied to study the emergence of invading cells and formation of clusters.

(iii) *Does post-translational modification of junctional proteins have a direct impact on regulation of cell-cell interactions in migrating clusters?* – Despite the extensive number of regulatory reactions taking place inside the cell, a small set of proteins are evolutionarily conserved. These proteins act in multiple pathways and play important roles in cells. One post-translational modification in particular, N-glycosylation, has been associated with epithelial discohesion and shown to add oligosaccharides to junctional proteins. In this dissertation the network dynamics of the N-glycosylation pathway in epithelial cells are explored using a system of differential algebraic equations and tested in cell culture through immunoblotting.

(iv) *Does regulation of junctional proteins affect specific physical characteristics and migrating dynamics?* – Local cell density, cluster displacement, and average cellular velocity are examples of quantities that can be used to characterize different clusters observed *in vitro*. To date, few studies look at migrating clusters in a 3D environment; this work presents a method to look at migrating clusters of epithelial cells and calculate these quantities. By using a multi-scale model that integrates agent-based particle modeling with pathway modeling, experimental results are used to correlate cluster dynamics with regulation of junctional proteins.

1.3 Structure of Thesis

Two background sections (Chapter 2) provide information on the biology of cell-cell junctions, the biology of the extracellular environment, the process of cell migration, and cancer, as well as, the background on computational approaches used to date to

explore systems of multiple cells. Next, a detailed description of the experimental methods and computational projects addressing the questions listed above along with the results is presented (Chapters 3-6). Finally, a last chapter summarizes conclusions of this study and potential directions for future work (Chapter 7).

CHAPTER 2. Background

2.1 Biological Background

As a physical system, a cell's interaction with its environment is dictated by physical and chemical reactions of the different components in the cell. In the process of signal transduction, a cell converts an external signal in the form of a chemical ligand or mechanical stimulus into a cellular response (17, 19, 20). The response in turns affects interaction of the cell with the outside through a feedback mechanism. This response can affect many different aspects of cell behavior such as proliferation, migration, differentiation, and cell death based on protein expression (21). Knowledge of cellular mechanisms describing cytoskeletal mechanics, cell-matrix interactions, and cell-cell interactions are necessary to form a comprehensive picture of collective cell migration and understand how theoretical models studying this phenomenon have been conceived.

2.1.1 Cell-Matrix Interactions

In the organism, most cells are found in a scaffold of proteins and polysaccharides known as the extracellular matrix (ECM). It is heterogeneous in composition, and its function ranges from providing structural integrity and aiding in tissue organization to signaling, guiding cell proliferation, differentiation, and survival (22).

The primary structural components of the ECM are collagen and elastin. Collagen, the more abundant of the two, is a protein that self-assembles triple-helical molecules into thicker fibrils (23). It is an adhesive component of the ECM, meaning cells can attach to it through formation of membrane complexes. Non-structural adhesive

components include the glycoproteins fibronectin, laminin, and vitronectin (23). The space in between the multiple proteins is occupied by hydrophilic glycosaminoglycans (GAGs) and water; however, the exact composition of the ECM is tissue-dependent. Based on its composition, mechanical properties change, providing a series of binding sites and a barrier to free diffusion of signaling molecules, such as growth factors (24). These soluble factors can be released upon local ECM degradation, creating concentration gradients important in cell signaling (24). This creates a gradient of morphogens that is used during developmental processes (24). In the process known as chemotaxis, cells move in the direction of a chemical gradient in the substrate.

Integrins constitute the principal cell surface adhesion molecule (22). In the cell membrane, an integrin receptor is active as a heterodimer, formed by selective pairing of one of 18 known α-subunits and one of 8 known β-subunits, producing 24 distinct receptors (23, 25). Named aptly, these receptors integrate the intracellular and extracellular environments by binding the cytoskeleton and the ECM and provide a bi-directional signaling path (22). The resulting transmembrane macromolecular complex is known as a focal adhesion (FA) (26). In a state of constant flux, focal adhesions recruit intracellular signaling kinases and promote cell polarization acting as constant sensors. Integrins bind specific amino acid sequences in adhesive components (*e.g.* R-G-D motif in fibronectin) (26). This sensing mechanism is necessary for cellular migration along the ECM.

2.1.2 Collective Cell Migration

Migration of animal cells has been observed in culture, where cells are exposed, and in the organism, through fluorescent tagging and two-photon microscopy (27). Different cell types have been found to migrate under different conditions and stimuli. Factors such as composition, structure, and dimensions of surroundings influence cellular migratory behavior, with a cell utilizing distinct molecular machinery (28). Thus, cell migration is a complex and heterogeneous phenomenon that has to be studied at different scales and in different systems. For most cells, including epithelial cells, migration is confined to morphogenesis and ends with differentiation. It can occur in later stages, however, when developmental pathways are reactivated in tissue regeneration or dysregulated, as is the case in cancer metastasis (5, 9).

The study of cell migration began with the observation of single cells and then cell sheets in 2D; extensive studies now exist on these systems (21, 29–31). The first study of an isolated collective was performed in 2D culture of poecelid fish melanoma (32), and similar clusters have been observed in 3D *in vivo* (27). Only until very recently have systematic tools to study 3D collective migration have been developed (33), and little is known about collective migration. In contrast, single cell migration has been well characterized. Given the heterogeneous character of the phenomenon, migration modes were originally classified based on morphology of migration patterns (28). This classification was later refined when molecular characteristics of the migrating cells were discerned, such as cytoskeletal organization, nature of cell-matrix interactions, and modification of surroundings. Two recurrent types of single cell migration are

mesenchymal and amoeboid; more recently migration modes that would fit within these categories have been induced and better characterized *in vitro* by engineering particular environments (34, 35). Cells have also been found to switch between migration modes. This switch is dependent on multiple factors, including ECM density, composition, and fiber orientation (36).

Mesenchymal migration is often described as a cyclical process consisting of distinct steps (37). Cells first become polarized forming actin-polymerization-driven membrane extension of the cell edge, known as the lamellipodium, in the direction of motion; this leading edge is formed by smaller protruding fibrillar actin spines, or filopodia, with a high concentration of FAs (38). The cell then contracts the network formed by fibers along the filopodia and its cell cortex, a network of actin, myosin, and associated proteins that lies under the plasma membrane (39). This contraction, performed through myosin-actin interactions, results in disassembly of FAs at the trailing edge, moving the cell body forward (24). Finally, free adhesion receptors in the rear can move towards the leading edge starting another migration cycle. While mesenchymal migration requires polarization, amoeboid migration is characterized by the lack of stress fibers and either weak or non-existent contacts to the surrounding matrix. Cell shape undergoes a non-adhesive conformational adaptation to the matrix, matching the path of least resistance. Then, displacement is achieved by propulsive squeezing pushing the cytoplasm through openings in the ECM (40).

Collective migration occurs when cells remain physically and functionally connected to each other during movement, either transiently or permanently.

Additionally, there is a supracellular organization of the actin cytoskeleton (5). Similar to single cell migration, it has been observed in 2D and 3D contexts (41). *In vivo*, collective migration has been found to serve mutually exclusive roles with single cell migration; collective migration is essential in building complex tissues, including epithelia, while single cells cover distances and integrate into already formed tissues (28). Similar to single cell migration, collective migration is classified according to the morphology of the collective: chain, detached cluster, keratocyte-like, and luminar migration are some examples (5).

Whether in single cell mesenchymal or collective migration modes, the migration process requires cells to navigate the ECM. This entails a dynamic deposition, rearrangement, cleavage, and degradation of components in the matrix. Deposition is performed not just by migrating cells but in some cases auxiliary cells such as fibroblasts (42). Degradation is performed by proteases, including matrix metalloproteinases (MMPs) (43). This family of functionally related zinc endopeptidases has been found to be involved in migration *in vivo* and *in vitro* (44). Focalized proteolysis is of particular importance in collective cell migration, in which migration is more space consuming within a tissue (45). In the case of migration in cancer, cells have been found to use surface localized as well as secreted MMPs, serine endopeptidases, and cathepsins to cleave ECM components, including collagen, laminin, and fibronectin (46, 47).

2.1.3 Intercellular Adhesion

Different types of multiprotein complexes constituting cell-cell adhesions exist in tissues with differing degree of strength and communication based on its components.

These include adherens junctions (AJs), desmosomes, gap junctions, and tight junctions (48). While gap and tight junctions provide communication for chemical and osmotic regulation of the intracellular environment, AJs and desmosomes anchor cells and provide mechanical communication. Further, desmosomes form patches that link cell-cell junctions to intermediate filaments, while AJs exist along the cell-cell boundary and bind to the actin cytoskeleton to form adhesion belts. In both AJs and desmosomes, members of the cadherin protein family bind to each other on opposing cells, forming homotypic bonds (49).

In collective migration, with transient cell-cell bonds and changing boundaries, AJs constitute the principal link between cells. Based on tissue type, different members of the cadherin family are found. This family includes N-cadherin, common in neural tissues, P-cadherin, originally found in the placenta but increasingly in other tissues, VE-cadherin in endothelial cells, and E-cadherin in epithelium (2, 50).

In epithelial tissue, E-cadherin structure consists of a cytoplasmic domain, a transmembrane domain, and an extracellular region comprised of five ectodomains (ECs) (51). Along with E-cadherin, AJs also include catenin molecules (52, 53). Catenin molecules are the link between AJs with the cytoskeleton. The individual or joint presence of the different catenin molecules in AJs indicates stability and maturity of junctions (54). β-catenin, γ-catenin, and p120 catenin can bind E-cadherin, with γ-catenin substituting β-catenin as a junction matures. α-catenin in turn binds either β-catenin or γ-catenin and the membrane-cytoskeletal protein vinculin, which in turns binds actin (54). AJs are dynamic structures, and regulation of their composition is determined by

different processes in the cell, including Wnt/β-catenin signaling, N-glycosylation of E-cadherin and other cellular components, and the transport of E-cadherin between different cellular pools (9, 55).

The Wnt/β-catenin signaling pathway is a key regulator of development and cell fate. First discovered in *Drosophila melanogaster*, this pathway is highly conserved in mammalian systems where it determines the patterning of the embryo and contributes to renewal of adult epithelium and stem cell homeostasis (56–60). Upon activation, the pathway upregulates the levels of the cytoplasmic non-E-cadherin-associated pool of β-catenin. This form of non-phosphorylated β-catenin is referred to as active β-catenin (ABC). In particular, the canonical Wnt ligand, Wnt3a, binds to the trans-membrane co-receptors lipoprotein receptor-related proteins 5 or 6 (LRP5/6) and the Frizzled receptors. Upon Wnt3a binding, β-catenin accumulates in the cytoplasm and moves to the nucleus where it acts as a transcriptional co-activator along with T-cell factor (TCF) to induce multiple Wnt target genes. It has been proposed that in the absence of Wnt3a, a β-catenin destruction complex (BDC) comprising Axin, adenomatous polyposis coli (APC), and glycogen synthase kinase 3β (GSK-3β) is free in the cytoplasm to phosphorylate β-catenin leading to its degradation. Instead, when Wnt3a is present and Wnt/β-catenin signaling activated, the destruction complex is sequestered in the membrane (61).

The number and complexity of N-glycans (*i.e.* oligosaccharides attached to asparagine (N) residues) in the ECs of E-cadherin modulate the force sensing ability and stability of AJs (62). Protein N-glycosylation, like Wnt/β-catenin signaling, has been identified as a fundamental process to eukaryotic life (63). This process consists of

synthesis of a lipid-linked oligosaccharide (LLO) precursor, its co-translational transfer in the ER to the polypeptide within the Asn-X-Ser/Thr consensus sequence, and further modification of the glycan through branching or addition of complex carbohydrates in the Golgi (64–67). There are four possible sites available for N-glycosylation along the ECs, although this may vary depending on species (68). Multiple glycosyltransferases have been identified in the N-glycosylation pathway; some are competing and have opposing effects on E-cadherin function (*e.g.* GnT-III, GnT-V) (63). Despite complexity of the pathway, early stages of N-glycan biosynthesis are highly conserved in eukaryotes. This suggests that mature LLOs play an important role in proper N-glycosylation, protein folding, and transport from the ER (67, 69). The first glycosyltransferase acting in the pathway is dolichol-P-dependent N-acetylglucosamine-1-phosphate-transferase (GPT), encoded by the gene *DPAGT1*. As expected, dysregulation of *DPAGT1* has been observed to affect organization and assembly of AJs (16, 62, 70).

As a Wnt target gene, *DPAGT1* acts as a common node between N-glycosylation and Wnt/β-catenin signaling. N-glycosylation of Wnt components impacts Wnt signaling as measured by the abundance of ABC. The extent of N-glycosylation regulates the strength of the Wnt signal as both Wnt3a and LRP5/6 are only efficiently secreted and positioned at the cell membrane, respectively, if properly N-glycosylated (62).

By affecting stability of AJs, N-glycosylation also affects E-cadherin recycling between cytoplasm and cell membrane. When unstable, AJs may disassemble and E-cadherin is internalized in endocytic recycling compartments (ERC), where it is either sent to a lysosome for degradation or sent back to the membrane where it can form new

AJs (55, 71). In this way, cell-cell adhesion is regulated by a regulatory cell network comprising different cross regulating pathways.

2.1.4 Cancer

While cancer can develop in many different tissues and subtypes recognized by diverse molecular footprints, it is a precise term that describes uncontrolled cell growth; the rules that govern the transformation into malignant cells are dictated by a small number of molecular, biochemical, and cellular traits shared by most cancers (72). In what is believed to be a process analogous to Darwinian evolution, cells become malignant by accumulating mutations that grant the growth advantages that eventually lead to death.

Tumorigenesis is the process by which uncontrolled proliferation and increased cell survival begins at a primary site, leading to formation of a tumor. Next, a subset of cells in the tumor gains the ability to invade neighboring stroma. When these cells migrate into the lymphatic or blood vessels, they can be quickly transported to distant sites where they can start secondary lesions, a process known as metastasis. Once metastasized, a series of secondary tumors cause organ dysfunction and eventually death (73).

To form a tumor, cells must evade apoptosis and gain self-sufficiency in growth signals, insensitivity to anti-growth signals, limitless replicative potential, and sustained angiogenesis (72). The first four of these capabilities acquired by malignant cells allow the tumor mass to form. Sustained angiogenesis, the formation of blood vessels from existing vessels, is required to maintain it and allows further growth of the tumor (74).

Angiogenesis is needed to prevent death of the tumor cells from hypoxia and lack of nutrients due to the difficulty in diffusion in a dense tumor mass. The size and shape of tumors are thus closely associated with angiogenesis.

Growth and structure of the tumor, and eventual exodus of invasive cells, are all dependent on the participation of auxiliary cells. Self-sufficiency of growth signals is achieved by malignant cells not only by generating their own, but by promoting release of signals by neighboring stromal cells (75). Intravasation, the process by with a cancer cell enters a lymphatic or blood vessel, has been seen to be aided in some cases by macrophages (76).

Because invasion is a crucial part of the evolution of cancer, the study of cell migration has at many points been tied to the study of cancer (77–80). Degradation of the ECM, for example, is a mechanism intrinsic to cell migration that is dysregulated in cancer. Overexpression of proteases, including MMPs, ADAMs, and ADAMTS is common to metastasis; this helps create an environment suitable for invasion (44). Additionally, cellular pathways important to development, specifically to migration during tissue formation, are deactivated after morphogenesis only to be reactivated in malignant cells (16, 81). Cancer has become a relevant model to study migration where cell migration occurs in the form of single cells, 3D invasive strands, or detached clusters from the transformed tissue. In carcinomas, disruption of the tissue occurs through a process known as epithelial to mesenchymal transition (EMT) (82, 83). The disrupted epithelium breaks up, giving rise to either single cells with mesenchymal phenotype or detached clusters (84).

In EMT, polarized cells undergo a transformation characterized by the loss of cell-cell junctions and increased migratory activity into dedifferentiated invasive cells (84). EMT was first identified in neural crest delamination, the developmental process by which cells at the interphase between nascent neural epithelium and ectoderm separate to migrate throughout the embryo and differentiate (85). It has been observed in other cellular processes of high physiological significance such as wound healing and gastrulation, were it is a temporary and reversible phenomenon (84, 85). In human cancers, evidence of EMT is seen in molecular signatures, such as the upregulation of proteins Ctgf, vimentin, and N-cadherin and simultaneous downregulation of E-cadherin (86–88). Yet, the molecular processes underlying the observed cellular change to a mesenchymal phenotype remain poorly understood.

2.2 Computational Background

The study of biological systems through computational modeling allows for easy quantification of parameters that are technically difficult to measure experimentally. Also, experiments that are financially prohibitive can be simulated repeatedly, and slight modifications on the reference experiment are easy. Specifically, computational modeling is widely applied in the study of mechanosensing and mechanotransduction in cell migration; it has been used to characterize mechanotaxis, durotaxis, and tensotaxis (89–92). Similarly, models of chemically induced migration (*e.g.* haptotaxis and chemotaxis) also exist (93, 94).

Efforts to model cell migration computationally can be broadly classified as either mechanistic or phenomenological. The first set looks to use biomechanistic interactions

of the different components of the cell and ECM to explain the system's behavior (*e.g.* migratory speed, direction) (95, 96). Because the molecular mechanisms behind single migration are understood, models addressing single cell migration usually belong to the mechanistic category. They tend to be detailed at the molecular scale. They have now, however, moved on to look at dynamics at the subcellular scale (97). Phenomenological models instead replicate the behavior of the whole cell to make conjectures on the mechanisms inside them (*e.g.* cytoskeletal dynamics) (98).

2.2.1 Cell Migration Models

The first model of single cell migration, DiMalli *et al.*, was based on the distinct steps describing mesenchymal migration. Using a Newtonian force-based approach, this model describes a two-dimensional cell in terms of cell-ECM interactions, polarization of adhesion receptors, and the resulting traction forces in the front and rear of the cell (96).

On a cell modeled as a two-dimensional rectangle, adhesion receptor dynamics are described as a reaction-diffusion problem that determines the distribution of cell adhesion receptors on the cell surface. Translocation occurs in opposition to the traction force that is determined based on the equilibrium FA concentration during sequential periods of lamellipodial extension, cytoskeletal contraction, and relaxation; the model accounts for endocytosis of unbound receptors and diffusion along the cell surface. A viscoelastic-solid model is used to describe force generation and distribution along the FAs. This modeled revealed a biphasic relationship between cell adhesion to the substratum and speed; a cell cannot move if too lightly or too strongly attached to the substratum. By also suggesting a relationship between cellular speed and cell stiffness for

a wide range of stiffness values, this model demonstrates the advantages of modeling systems where experimental measurements would be technically difficult.

The first model of cell migration in three-dimensional environments, Zaman *et al.*, was similar to the two-dimensional rectangle model. To scale to 3D, it incorporated the viscosity of the ECM and density of ligands along the cellular path (99). It was then expanded to include degradation of the surrounding matrix (14). Rather than calculate translocation as the response to traction, a drag force is included and the cell's forces are assumed to be balanced. More simplistic in its approach than the 2D rectangle model, instead of having freely diffusive receptors on the cell surface, receptor number was only considered at the leading and trailing edges of the cell, with separate functions determining the two concentrations. Also, the cell is modeled as a sphere, so the Stokes-Einstein equation is used to calculate speed and thus displacement of the cell (14). This model tested the implications of two experimentally supported relationships between MMPs and ECM ligands, helping discern the bidirectional coupling of cell-ECM adhesion and matrix degradation.

Currently, single cell models have expanded to include both time and spatial dynamics within the cell as well as the effect of biochemical rates of intracellular signaling networks in migration. By using partial differential equations (PDEs), these models explore intracellular pathways regulating cytoskeletal dynamics, including processes of protein diffusion and advection within the cytoplasm, actin polymerization, fiber crosslinking, and actin-myosin contraction, diffusion of proteins along the membrane, and formation of FA spatially along 2D representation of the cell (97, 100).

Other models have been developed studying not the effect of dynamics inside the cell but outside of it. A model focusing on cell-ECM interactions considers the effect of contact guidance and matrix remodeling, taking into account matrix stiffness and architecture (101).

Other models recreate specific phenomena of cell migration that occur in specific conditions and only in certain parts of the cell. Not all single cell models are mechanistic; some models explain migration by phenomenologically accounting for changing shape. This is the case of cellular Potts models (CPMs), in which cells are represented by multiple lattice based units, pixels or voxels base on dimensionality (102, 103). The boundaries of these units are grouped to represent a single cell and updated based on an energy minimization equation; each unit is assigned a spin. Factors relevant to cell migration, such as adhesion and cortical tension, are represented by a membrane tension parameter in terms of energy per unit length. Cell area or volume is constrained to a reference volume and compressibility. In this way, CPMs can distinguish between favorable and unfavorable cell configurations based on energy calculations. These models have effectively captured global features of tissue rearrangement but not capture its dynamics.

No models of collective migration exist, because the phenomenon is not as well understood as single cell migration. There are, nonetheless, models that look at multiple cells simultaneously. As with single cell migration, models of cell populations look at cancer as a model system. Tumor growth models, belonging to the phenomenological category, represent a wide portion of existing models (104–106).

2.2.2 Tumor Growth Models

Tumor growth models can be classified into agent-based models (or discrete) and continuum models. Much focus has been placed on the effect of proliferation, and the effect of nutrient availability, on tumor growth. By changing parameter values the models simulate different potential malignant phenotypes and assess the impact of the parameters on tumor growth rate, size, shape, and invasive potential.

Agent-based models treat cells as individual units interacting according to a set of rules. They are phenomenological and have been used to explain phenomena such as organ morphogenesis in addition to tumor growth (106, 107). Cells are represented in multiple manners, either as points, agglomerations of spatial units (*e.g.* CPM), elastic circles or spheres, or irregular partitioning of space (*i.e.* tessellation) (15, 107, 108). Agent-based models often include stochastic decisions, such as migration direction or daughter cell orientation upon cell division (15); a migration step of each cell is either taken or not based on a probability and availability of the destination volume. The volume occupied by cells was originally represented by lattice points, but lattice free models were later developed. CPM models are an example or lattice-free agent-based models; they are capable of recreating the phenomenon of cell streaming out of the tumor mass, probing the question of leadership in collective migration (103, 109). By simulating homotypic and heterotypic adhesion, these models have been able to simulate cluster detachment from tumor mass; however, they fail to account for dynamic regulation of adhesion at the single cell level (110).

Continuum models are deterministic in nature, often defined by a set of analytic

equations. They are historically inspired in models from ecology, describing the population of cancer cells using population growth models (111). Shape change is modeled as a flux of cells within the cell mass (112). Similarly, the use of diffusion-reaction equations simultaneously accounts for spatial variation in multiple factors external to the cell, including ECM components, MMPs, nutrients, growth factors, and oxygen (113, 114). Treating cell populations as a unit, continuum models have the ability to represent larger systems in a computationally efficient manner. They fail, nonetheless, to effectively take into account changing intercellular interactions (15). For instance, cell populations modeled as a continuum lack the ability to breakup or combine into new groups; crucial elements to collective migration, such as cell-cell adhesion, are not accounted for.

Hybrid approaches, combining agent-based and continuum models also exist (115). In these, a lattice free agent-based representation of cells is superposed on a lattice used for diffusion of soluble factors. The concentration of these factors at points outside the lattice, where cells are found, can be interpolated. The lattice is updated in between migration steps by an extrapolation. These approaches have the advantages of both types of models, but are more computationally intensive.

2.2.3 Self-propelled Particle (SPP) Models

Studies with phenomenological models of cell collectives have focused on recreating the extent of invasion; however, a few have raised the question about the existence of pioneer cells leading the way (116). With this question at the forefront,

researchers have sought to understand the dynamics cells in collectives (117). This endeavor, however, belongs to the realm of collective behavior.

Collective behavior can be defined as the emergence of complex migration patterns in scales larger than that of the individual elements forming the system (118). Observed naturally in swarms of fish or birds, for example, it can be simulated by restricting motion of a few particles with a small set of rules. This is demonstrated through self-propelled particle (SPP) models. SPP models are a specific class of agent-based model that, in its simplest form, consist of restricting the velocity of particles along a line with periodic boundary conditions to the average velocity of all other particles within a radius (119). This simple one-dimensional model shows that given this simple setup alignment can be reached by all particles. With increasing noise, the direction of the motion can be reversed.

Later expanded by others to two and three dimensions, SPP models have been widely used to study emergent complex behavior of multiple particle systems, including biological systems (12, 120). Parameters influencing dynamics include particle density, noise, and radius of interactions between particles. Analogous to phase transitions in physical systems, alignment of particles shows sharp transitions in parameter space (121). The behavior of the particles is also reminiscent of phase transitions with its sharp changes in internal diffusion, appearing to transition between states similar to crystal solids and fluids (12).

These models can also be made more intricate and used to model more complex biological systems, such as locusts and birds as well as streaming in mammalian cell

monolayers (120, 122). SPP models are highly flexible due to their simplicity and have been made more sophisticated by adding attraction and repulsion forces to simulate volume exclusion, restricting the radial range over which particles influence its neighbors, or making the scaling of velocity highly parametric (12, 120, 123). More recently, SPP models have been used to simulate dynamics in groups of eight hundred cells with two different adhesion capabilities on a 2D surface. This showed evolution of the system towards segregation of the two distinct populations (124).

2.3 Conclusion

The evolution of SPP models is representative of a trend observed in modeling of cell migration; with increasing understanding of both physical and biological mechanisms, modeling of cellular systems evolves from being descriptive towards mechanistic. This dissertation presents a further step in this direction, using knowledge gained about regulation of intercellular adhesion along with physical studies of cell-ECM interactions, to elucidate the contribution of physical and biological factors to collective cell migration.

CHAPTER 3. Rigid Cluster Model

This chapter presents a first forced-based dynamics computer model of a cell cluster moving collectively in a three-dimensional environment mimicking the ECM. Derived from forced based mechanistic models of single cell migration (14, 95), this model of five cells joined in a cluster was developed taking into consideration the impact of three major factors: ligand concentration, matrix metalloproteinase activity, and cluster geometry.

Existing efforts to quantify collective migration focus on groups of cells that arise from larger aggregates, as in tumors (110). There has been no effort, however, to quantify migration ability of detached groups of a few cells. This is the first attempt at doing so.

This is a model of a rigid cluster in the sense that the geometry is fixed for each migration step. In between steps, however, the cells constituting the cluster may rearrange to one of seven possible configurations. Each configuration affects differently the way the cluster interacts with its surrounding environment. The velocity profiles of different migration simulations were recorded and analyzed. In particular seven different profiles are observed based on different participation of ligands, proteinases, and mechanical forces involved. The model is successful in showing potential effects of altering single parameters describing internal and external factors in a migrating cell collective.

3.1 Introduction

Collective cell migration is a relevant part of the mechanisms for tissue repair, morphogenesis, and cancer invasion (125). Particularly in cancer, invasion occurs

through multicellular 3D strands as well as collective cell clusters (126). Because cancer is a slow process, these clusters have not been observed in detail. The prevalence of this migration mechanism, however, makes it a target for study.

Indeed the mechanism by which a cluster forms is unknown; it is suspected to require a polarization of multiple cells and physical coupling between the cells (126). Polarization occurs in the form of a leading edge similar to the lamellipodia in single cells, but that extends along multiple cells. This is evidenced by the formation a supracellular actin structure (5). Similarly, multiple cells also form a trailing edge. In contrast to single cell motion, where the back of the cell binds the substrate, the back of a cluster appears to be simply trailing the cells involved in protrusion. These characteristics are incorporated into the developed model to include their role in collective motion. Then the migration process additionally involves regulation of growth factor and chemokine expression, and formation of FAs (126). Accounting for all factors simultaneously is a challenging task that makes assessment of the influence of individual factors difficult. For this reason, this first model chooses to focus on polarization of forces for a fixed geometry during each migration step and degradation of the surrounding ECM. The latter is particularly important as this model broadens the understanding of cell migration specifically in three-dimensional environments.

While experiments exploring migration on two-dimensional substrates have provided a valuable foundation for migration studies in three dimensions, a more thorough understanding of invasion in morphogenesis, tissue regeneration, and cancer metastasis require studies exclusively looking at the effect of factors only existing in a

three-dimensional environment. In contrast to 2D migration, where cells are exposed on top of a substrate that does not necessarily require remodeling, 3D migration implies navigation through a dense surrounding matrix. Experiments in 2D and 3D have yielded different results; this indicates that different mechanisms may become active or inactive based on the dimensions of the substrate. The composition of FAs also varies based on whether a cell is in a 2D or 3D environment (127, 128).

Invasion by detached cell clusters has been observed in breast and colon carcinoma, prostate cancer, and melanoma. These cells retain high or intermediate levels of differentiation and are unlikely to disperse as individual cells (129). This has led to a hypothesis that cells move collectively because it provides mechanistic advantages such as maintaining high autocrine concentrations of pro-migratory factors, protecting inner cells from immunological assault, and allowing cells in a group to have different specialized functions advantageous to an invading body (129). Further understanding of this mechanism would provide new information on the molecular processes involved, and would be useful in characterizing more thoroughly all mechanisms of cell motion.

3.2 Model Formulation

3.2.1 Cluster Size and Geometry

Because little is known about collective migration of cellular clusters, the size of the clusters remains unknown. A cluster of five cells is chosen to develop a computationally tractable model based on observations in other systems of collective cell motion and 2D studies (32, 33, 130). This is small enough to keep the model versatile for

further changes based on desired complexity while allowing enough distinct geometries to draw meaningful conclusions from the simulations. The number of cells is kept constant because it has been observed that a cluster will keep its integrity for hours at a time (32). Similarly, simulated cells are spherical; the radius can be found in Table 3-1.

Simple constraints are used to determine the possible geometries: 1) Each cell can only be attached to a maximum of three cells. 2) Cells cannot come in contact unless they are connected (*i.e.* cluster is rigid). 3) There is a single trailing cell for each geometry, the cell at the end of the cluster along its longest dimension. While these assumptions may seem simple, they correspond to experimental observations on cluster geometry and size often seen in development and tumor growth and metastasis (32, 125, 130). Using these constraints, six distinct planar geometries are defined: These are designated as *linear geometries*. Two clusters are considered distinct if they cannot be superposed taking in consideration the identity of the trailing cell. A seventh geometry, free of the first constraint, is also considered which consists of placing the five cells in the vertices of the polyhedron formed by joining two tetrahedrons by one face. The length of the sides of the geometry was twice the radius of the cells. This is designated as *tetrahedral geometry*. The seven resulting cluster geometries are displayed in Figure 3-1. The center of mass is calculated for each cluster geometry.

Similar to previous work, each time step simulates the motion of the cell cluster over a large time step (~600s) to capture a complete migration cycle. After each migration step, based on a probability, the cluster either remains in the same geometry or changes to a geometry that would arise from formation or dissolution of a direct contact

between two cells. The change between geometries at every step is managed through a randomly selected probability based on the structural similarities of the chosen geometries; Table 3-2 contains the probability values used. An exception is the transition to the tetrahedral geometry, where two connections would have to be formed. No attempt at modeling cell-cell junction dynamics was made at this stage; however, it is assumed the probability of remaining in the same geometry is higher than that of changing [16].

3.2.2 Forces Acting on the Cluster

The model takes into consideration the distinct steps defining mesenchymal cell migration: polarization, contraction and resulting generation of traction forces, and retraction of the cell body (37). What this model introduces is the consideration that upon having multiple cells moving, these three major phases are modulated differently in different parts of the cluster (*i.e.* in different cells based on position within a cluster). The cluster geometry selected at each step determines how the forces acting on the body are defined.

The net force acting on the cluster is described by Equation 3-1:

$$\boldsymbol{F}_{drag} + \boldsymbol{F}_{traction} + \boldsymbol{F}_{protrusion} = \boldsymbol{0} \tag{3-1}$$

where $\boldsymbol{F}_{protrusion}$ is the sum of all the protrusion forces generated by each cell, $\boldsymbol{F}_{traction}$ is the opposing traction force generated by summing the traction force generated by each cell at both its front and back upon cytoskeletal contraction, and $\boldsymbol{F}_{drag}$ is the drag force experienced by the cluster as it retracts from the balance of protrusion and traction. The

protrusion and traction forces oppose each other in orientation. The traction force for each cell occurs due to the cytoskeletal contractile forces exerted against the adhesion sites; it is modeled as a fixed force scaled by a scaling factor defined as adhesivity (β), dependent on the number of ligands in the ECM and receptors on the cell membrane. A more thorough description of this force can be found in the work by Zaman *et al*. (99). Adhesivity is taken to be different in the front and the back of the cell to account for cell polarization. Adhesivity is defined in Equations 3-2 and 3-3:

$$\beta_f = k_1 \times n_f \times [L_f] \tag{3-2}$$

$$\beta_b = k_2 \times n_b \times [L_b] \tag{3-3}$$

where k_1 and k_2 are the binding constants for binding of integrin molecules in the front and back of the cell respectively, n_f and n_b the total number of receptors (*e.g.* integrins) available in the front and back of the cell respectively, and $[L_f]$ and $[L_b]$ the concentrations of ligand molecules in both the front and back of the cell respectively (*e.g.* peptides in the ECM that can be bound by integrins). In the present model 95% of the receptors were considered to be in the front of the cell and only 5% in the back. The binding constant for integrin was considered the same for molecules in the front and back of the cell. The initial value of the ligand concentration and the value of the binding constant for integrin can be found in Table 3-1.

These protrusion forces corresponding to each cell are added, as well as the

traction forces, forming a general force term for the whole cluster. This term is then set equal to the negative of the drag force for the whole cluster accordingly with Equation 3-1. In this case, the drag force for the whole cluster is then used to calculate the velocity using Equation 3-4:

$$|\boldsymbol{F}_{drag}| = \tfrac{1}{2}\rho \times |\boldsymbol{v}|^2 \times C_D \times A \tag{3-4}$$

where ρ is the density of the surrounding medium, $\boldsymbol{v}$ is the velocity of the cluster, C_D is the dimensionless drag coefficient dependent on geometry, and A is the reference area (projected frontal area of the cluster in the direction of motion). Table 3-1 contains the values used for C_D and ρ. How these quantities are approximated is briefly discussed in the next section.

Equation 3-4 describes the drag experienced by an object immersed in a fluid. For the case where the Reynolds number is very small (what is known as "creeping flow") and the geometry is simple, the body drag can be computed. This was the case in previous models, where the drag force had been calculated through the Stokes-Einstein equation since a single cell was being modeled as a sphere (14, 99). In general for "creeping flow", the drag coefficient if proportional to the Reynolds number, which when substituted into Equation 3-4 along with the known body drag simplifies the relationship, usually resulting in a proportional relationship between body drag and velocity. The proposed model, however, includes a varying geometry along with a changing environment which complicates calculation of the body drag. For this reason the more

general form of the drag equation was used, and an additional constant scaling factor was included to account for any shortcomings that arise for the unknown physical factors.

3.2.3 Force Modulation

As indicated previously, each of the main forces acting on every cell during motion is modulated based on the role of the specific cell in the cluster. These roles are not fully understood and subject to debate; some findings suggest this depends on the cell type from which the cluster originates and the tissue being transmigrated (126). For this reason, a series of assumptions based on observations on 2D and 3D *in vitro* experiments are used to define how forces are modulated in each cell in the cluster. This force modulation is intended to represent how forces, polarity, and adhesion affect cluster motion.

A cluster of cells behaves similarly to a single cell in that it has a polarity that defines the direction of protrusion and maintains a general direction. In the case of 2D motion, cells facing the direction of motion form a leading edge, in which most lamellae are found (32). Nonetheless, cells on the periphery of this edge also have some protrusion activity (131). Meanwhile, trailing cells are simply pulled in the direction of motion (131). Their role appears to be to create a force perpendicular to that of cluster motion to maintain certain firmness of the whole structure. They are maintained perpendicular to the direction of motion by the lamellipodia of cells at the edges surrounding the back part of the cluster. It is as if these border cells attempt to leave the cluster but are kept due to their junctions with trailing cells. It has been observed that trailing cells maintain their role throughout the life time of the cluster; they have an elongated shape which does not

allow them to generate protrusions of their own (32). The first assumption, based on these considerations, is that every cell that is not a trailing cell is taken to contribute to the protrusion force. Thus the ligand concentration and receptor number are of importance in the calculation of forces for every cell, not just the leader cell. The number of ligands and receptors will change for a cell with proteolytic activity, explained in section 3.2.4.

In a second assumption, the cell that acts as the leader is allowed to change with each migration step. This cell is selected based on the direction of the protrusion force in that step. A constant value was used for the protrusion force for the leader cell, and its direction was randomly selected from the center of mass of the cluster. Any cell except for the trailing cell can be selected as the leader cell. Similarly, a single trailing cell was selected in each geometry. Unlike the leader cell, which changes based on direction of motion, the trailing cell is never changed (Figure 3-1).

The model considers the possibility that every cell not acting as the leader has the potential to move within the cluster in each step, changing positions. This assumption accounts for the change of cell role within a cluster. For the case of five cell cluster, there are two pairs of cells that could exchange positions. For each pair there is a 10% probability of an exchange occurring. If an exchange occurs, then for each exchange event occurring, one less cell will be contributing to the protrusion force within the cluster since cells have been shown to translocate actively instead of passively within a cell collective (126).

When calculating $\boldsymbol{F}_{protrusion}$, the contribution of each non-trailing cell is scaled based on the role of cells within the cluster in each specific step. Every non-trailing cell

different from the leader contributes with 25% of the magnitude of the protrusive force exerted by the leader cell; this force is exerted in the direction of motion. This percentage of contribution was selected arbitrarily based on the approximate area of the cell surface exposed to the environment. When calculating $\boldsymbol{F}_{traction}$, only the non-trailing cells that do not change places within the cluster were considered to contribute to the force. Unlike the protrusion force, the traction force is not scaled based on whether the non-trailing cell is a leader cell or not because it does not depend on a membrane exposure criterion (*i.e.* filopodia extension), and receptor density along the cell membrane can itself be regulated by the cell.

Finally, calculation of the velocity (Equation 3-4) does not depend on the cell composition of the cluster but on the cluster geometry, because the drag coefficient and reference area are geometry dependent. In the model, the reference area was made to be a function of the direction at which the protrusion force acted on the cluster. This value was purposely made variant in order to counterbalance the rigidity of the cluster geometries and provide a more gradual change in the force values between geometries as would be expected for an actual cell cluster. More specifically, the reference area was made a function of the angle between the direction of motion and the line formed by joining the centers of two cells farthest apart from each other in each geometry; the reference area was calculated in each step based on the new randomly selected direction of cluster motion. For the drag coefficient the value selected was judged to be approximate to the average of the possible values that could arise for the different geometries.

3.2.4 Proteolytic Activity

Although the importance of proteolysis in collective cell migration is apparent, contact structures in three-dimensional movement remain poorly defined. This motivated the addition of proteolytic activity into the model.

From the different proteolytic species known, only the action of matrix metalloproteinases was considered because certain MMPs (*i.e.* MT1-MMP/MMP14) have been identified as the rate-limiting collagenases, and interference with their action prevents efficient motion *in vitro* (132). In accordance with the positive results of previous work, both soluble and membrane-bound MMPs were simulated using a single generic active MMP term (14). Proteolytic activity is effectively awarded to a single cell because force generation and ECM degradation are spatially separated for single moving cells, and different cells have different functions in a cluster (133). For this cell with proteolytic activity, the generic MMP concentration term [M] affects the ligand concentration and the number of receptors, thus affecting adhesivity and in both ways affecting the traction force contribution of that particular cell. The relationship between these quantities is described in Equations 3-5 and 3-6:

$$[L_{f2}] = [L_f] - [M] \tag{3-5}$$

$$n = r \times [M] \times 10^6 \tag{3-6}$$

where $[L_{f2}]$ is the ligand concentration at the front of the cell with MMP activity, r is the

fixed total number of receptors expressed on a cell, and n is used to define both n_f and n_b in Equations 3-1 and 3-2. For cells without proteolytic activity, n is constant throughout the simulation and n is equal to the total number of receptors on the cell (Table 3-1).

3.2.5 Ligand concentration

The biphasic effect of adhesion on velocity is extended in this model to cluster migration. To match the relation between speed and adhesion, ligand concentration is lowered with each step such that eventually the cluster comes to a stop. Equation 3-7 describes this decay in ligand concentration:

$$[L_f]_{s+1} = [L_f]_s - (5\times10^{-8}\times [L_f]_s\times10^{-16.5}\,(s\times10^5+1)) \tag{3-7}$$

In this equation s represents the step in the simulation. This amounts to a change in ligand concentration from the initial value of 10^{-5} M, as seen in Table 3-1, to 10^{-9} M after 100 steps of the simulation. Since $[L_b]$ is equal to $[L_f]$, this equation describes the decay in ligand concentration in the front and the back of each cell.

3.2.6 Model Implementation and Simulated Conditions

Computations were performed using Mathematica 7 software (Wolfram Research, Champaign, IL). Each simulation was run for 100 steps, and in each step the position of the center of mass and velocity were recorded. Due to the nature of the model, no singularities were observed.

Two sets of simulations were run. In the first set, only the tetrahedral geometry is

used with no reconfiguration of cluster geometry in between migration steps. This presents a preliminary or reference case for cluster migration. In the second set, both linear and tetrahedral geometries are used.

Initial implementations of the model resulted in the velocity becoming unbound due to the dynamic way in which ligand concentration and MMP concentration were defined (Equations 3-5 and 3-6). MMP activity overpowers the decay in ligand concentration and the force contribution of the cell with MMP activity would define the cluster behavior. This occurrence was addressed in multiple ways, providing the basis for different simulated conditions:

1) *Lowered MMP concentration*: Reduction of the initial concentration of MMP to maintain this concentration lower than that of the ligand throughout the simulation. Initial MMP concentration was reduced from 10^{-7} (as specified in Table 3-1) to 10^{-12} M; then MMP concentration was increased by 10% in each step, making the final concentration 10^{-8} M.

2) *Increased initial ligand concentration*: The initial ligand concentration was set to 5 M instead of 10^{-5} M. This value may seem high, but it is chosen such that it does not conflict with the changing MMP concentration. Additionally, the ligand concentration decreases in each step based on Equation 3-7.

3) *Modified traction force*: Changing the adhesivity proportionality constants (k_1 and k_2 in Equations 3-2 and 3-3) for the cell with MMP activity. The value of these constants was changed from 1 to 10^{-6}. Even if this condition does not correspond to a physiological state (*e.g.* change in [M] or [L]), it was still implemented because the contribution of each

cell to traction of a whole cluster has not been characterized and open to exploration.

4) *Complete localized ECM degradation*: Ignoring traction component of cell with MMP activity once overpowering occurs.

3.3 Results

3.3.1 Tetrahedral Cluster Has Widely Varying Speeds

Figure 3-2 displays the resulting velocity profiles in time corresponding to each of the four conditions simulated only using the tetrahedral geometry. It can be observed how a dual behavior is observed with the magnitudes for the speeds alternating between values differing by one order of magnitude. This may give the appearance of two separate lines being observed in Figure 3-2; however, all points in these plots correspond to a single simulation (*i.e.* velocities correspond to motion of a single tetrahedral cluster). This duality is expected for this geometry since the drag is calculated based on only two possible orientations of the cluster (*i.e.* only two constant reference areas); as opposed to, when using seven cluster geometries, where orientation is defined as a function of the direction of the protrusion forces. This significant difference in speed based on selection of the leader cell is reflected in the trajectory of the cluster (not shown). The trajectory is very straight because speed is greatest when the leader cell is that opposite edge of the cluster to the trailing cell and much lower when any other cell acts as leader. It is important to note that both sets of velocities appear to follow the same trend throughout the simulation. This would lead to believe that other than the orientation, other factors such as ligand density, adhesivity, MMP concentration, etc. are play a significant role in

determining the motion of a cell cluster.

Another important observation in the first set of simulations is that resulting velocities range between 0-0.5 μm/h for three sets of simulation conditions: Lowered MMP concentration (Figure 3-2a), modified traction force for cell with MMP activity (Figure 3-2c), and complete localized ECM degradation (Figure 3-2d). Meanwhile, the condition corresponding to an increased initial ligand concentration (Figure 3-2b) has significantly higher velocities ranging between 0-400 μm/h. The former are lower than the velocities expected for a cluster of five cells; the latter are higher than expected and closer to that of single cells. Although no *in vivo* recordings of the velocity of cell clusters in cancer exist, a cluster of around 15-30 cells is expected to move at approximately 66 μm/h (125). The velocity of single cells of the same type as those in the tumor was recorded to be approximately 193 μm/h. Although larger clusters of cells were recorded to move slower, there appears to be no proportionality between cluster size and velocity (32, 125). This model attempted to account for this as can be seen from Equation 3-4, in which the only term affected by the number of cells is the drag force, dependent on traction and protrusion forces, both a consequence of the sum of forces exerted by the number of non-trailing cells. However the parameters reference area and drag coefficient are dependent on geometry which has a more complicated relation to cell number. The values recorded were satisfactory, being these the upper and lower bounds of velocity observed in cells. These values are expected to change if the contribution of each cell to cluster motion is known and adjusted accordingly in the model. Overall, the velocity profiles presented in Figure 3-2 are relevant as they are preserved in the second set of

simulations with multiple cluster geometries. These trends may indicate how a cell cluster responds to each of the four changes or premises to the system, which can potentially be explored experimentally.

Additional simulations were run implementing two of the different conditions simultaneously. An exception was made for complete localized ECM degradation, since all other conditions imply active proteolysis. Any attempt to implement this condition simultaneously with any other would yield the velocity profile found in Figure 3-2d. Instead lowered MMP concentration was coupled first with increased initial ligand concentration (Figure 3-3a) and then with modified traction force (Figure 3-3b). Finally, another simulation was run with increased initial ligand concentration and modified traction force (Figure 3-3c).

The velocity profile for simultaneous lowering of MMP concentration and increased initial ligand concentration is significantly different from the profiles obtained when implementing the same conditions separately. This indicates that both proteinase activity and ligand presence significantly affect cluster motion to a similar degree.

The maximum velocity during the simulation is achieved relatively early, as is the case when only MMP concentration is altered. This is so because by that point in the simulation the increased ligand concentration has prevented MMP activity from significantly altering the force balance of the cells. However, the drop in velocity when including an increase in the initial ligand concentration is more drastic: This was expected since both concentrations are being altered, intensifying the lack of traction in the cell (MMP concentration although lower is still increasing). Interestingly, the profile

for a simultaneous increase in ligand concentration and altered participation of traction force for cell with MMP activity appears identical to that in which the two concentrations were changed. This can be explained by observing the profiles in Figure 3-2 for a lowered MMP concentration (Figure 3-2a) and a modified traction force applied individually (Figure 3-2c). The profiles are almost identical, except for a slight rise close to the end of the simulation in the second case. This suggests that the effect of changing the contribution of the traction force is equivalent to decreasing the MMP concentration. This also explains why the profile for lowered MMP concentration and modified traction force for cell with MMP activity (Figure 3-3b) is almost identical to that observed for each solution separately in Figures 3-2a and 3-2c. This is relevant because it shows the degree in which these quantities need to be changed to affect motility similarly.

3.3.2 Dynamic Clusters Are More Aimless

The second set of simulations is performed with a dynamic cluster that can potentially change geometries in every step; the cluster can adopt any of the seven geometries considered (linear and tetrahedral). Each of the four conditions considered to prevent the velocity from becoming unbound, along with the combinations of these, are implemented. Examples of the results for individual simulations for two conditions implemented individually can be observed in Figure 3-4. An average of the resulting velocity profiles over 100 simulations can be found for all conditions implemented individually (Figure 3-5) and of two conditions implemented simultaneously (Figure 3-6). The same pairs of conditions were implemented together as in the simulations with a single tetrahedral cluster geometry.

The trajectories followed by the clusters in this second set of simulations are not straight, compared to those using a single tetrahedral geometry (not shown). Instead the clusters moved with some directionality while having periods in which movement resembled a random walk. This can be attributed to the fact that the probability of remaining in the same geometry between steps is higher than that of changing into each of another possible one. Also, from one step to the next the geometries adopted are close to each other since they are based on formation of a single connection between two cells as explained in section 3.2.1. These trajectories are not meant to be realistic since choice of leader cell was performed based on a randomly selected direction of the protrusion force. In the future, directionality persistence can be analyzed in a model in which chemical or other environmental cues are used to define direction of this force.

As expected from the results of the first set of simulations (with a single tetrahedral geometry), the points are more scattered for each of the four simulations when using multiple geometries. This is evidenced by the non-smooth curves observed in Figure 3-4. This is explained because there are more possible configurations with respective reference areas defining the drag the cluster experiences. However, the same trends in the velocity graphs can be observed when comparing the corresponding graphs for the same solution in the two sets of simulations. To demonstrate this, simulations implementing each solution were run 100 times and the values for the cell cluster velocity at each step were averaged (Figures 3-5 and 3-6).

3.4 Discussion

Collectively, the results suggest that velocity is more dependent on cluster geometry and less on external conditions to which the cluster is exposed (*e.g.* ligand concentration) and other factors such as MMP activity. In comparing the velocity profiles obtained for simulations with a single geometry and a changing geometry, it can be observed that the latter are higher. This is so because the recorded values are averages, including velocities that may differ even by one order of magnitude as shown in Figure 3-2. Nonetheless, there is a significant difference in cluster speed between simulations with lowered MMP concentration (Fig. 3-5a), modified traction force (Fig. 3-5c), and complete localized ECM degradation (Fig. 3-5d) and the speed in the simulation with increased initial ligand concentration (Fig. 3-5b). The values are closer to those observed for cells *in vitro* for the former group (32): The velocity varied between 1-10 μm/h. For the simulations with increased initial ligand concentration (Fig. 3-5b) the velocity ranged between 1000-8000 μm/h. The velocity increases by the same factor as in simulations implementing the other three conditions compared to the simulations with only one geometry; however, these values are unreal. This occurs due to the very high, also unreal, ligand concentration used.

With the development of force traction microscopy (FTM) as well as super resolution microscopy, it has become possible to measure the different protrusion and traction forces in migrating single cells or cells collectives in 2D (134). With these techniques displacement of labeled elements by the cells can be converted into forces and resulting stresses. Recently, efforts have been made to expand this technique into either

setups that mimic a 3D environment, by exposing cells to ligands from top and bottom, or embed cells in actual 3D matrices (135, 136). These attempts simplify the conversion of displacement into stresses, but provide, nonetheless, a spatial map of protrusion and traction by cells. The knowledge gained from these studies can be implemented in the rigid cluster model to refine polarization of the cluster. The model currently shows the importance of geometry and leader cell selection; it does this by yielding very discrete migration steps that change direction and speed drastically. This is very revealing, but should be addressed if using this model further. Most recently, a first attempt at quantifying tensile forces in collective migration seeded mouse mammary epithelial cells in designed micrometer-scale cavities in type I collagen (137). With this approach, the authors tracked only protrusions of the cluster as the clusters themselves do not move. By designing the geometry of the cavity, the protrusions resulting from geometry and surrounding ECM can be used to refine how protrusion forces are modeled and possibly how leadership is first established.

With a constantly changing geometry also changes the probability of each cell being the leader cell, the reference area, and consequently the drag force experienced by the cluster. Even with so many variables affected by geometry of the cluster, the velocity profiles with changing environment or expression of receptors observed in the two sets of simulations are comparable if not equal in both shape and relative magnitude (compare Figures 3-2 and 3-5 or Figures 3-3 and 3-6). Independent of how speed is scaled, external parameters affect the cluster equally in all its conformations. This can play a role physiologically, where cells are many times forced to change or maintain a shape based

on the architecture of the surrounding tissue while still persisting in their movement. In this way, too the rigid cluster model is successful in creating cells with variable states that still present steady velocity profiles thus elucidating the relative importance of different environmental factors affecting cell locomotion.

In general, the comparison between the two sets of simulations and the results for each of the implemented conditions show that altering a single parameter (or physical condition) will result in a different plausible cell cluster behavior. The model is successful in showing potential effects of altering single variables in a system of cells in motion in a complex 3D environment. Changes in a single measurable parameter led to significantly different velocity profiles. Sometimes similar to each other, varying biochemical factors may have similar physical effects on a cell cluster.

3.5 Tables

Cell radius	25 μm
Density of ECM	1.5 kg/m^3
Drag coefficient	0.65
MMP concentration	10^{-7} M
Ligand concentration	10^{-5} M
Number of receptors (r)	10^7 receptors/cell
Binding constant for integrin	10^8 M^{-1}

Table 3-1: Order of magnitude estimate of model parameters

GEOMETRY	A	B	C	D	E	F	G
a	0.4	0.2	0.2	0.2	0	0	0
b	0.3	0.4	0	0	0.3	0	0
c	0.3	0	0.4	0	0	0.3	0
d	0.4	0	0	0.4	0	0	0.2
e	0	0.4	0	0	0.4	0	0.2
f	0	0	0.4	0	0	0.4	0.2
g	0	0	0	0.2	0.2	0.2	0.4

Table 3-2: Probabilities of changing cluster geometry between migration steps

Geometries are denominated as in Figure 3-1. Lower and upper case symbolize initial and final geometries respectively.

3.6 Figures

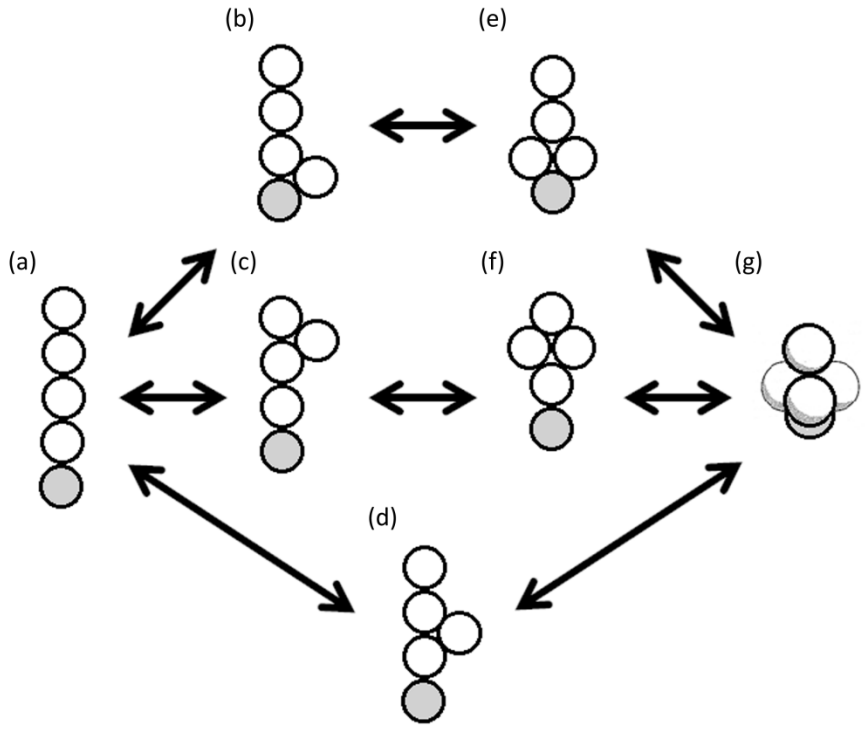

Figure 3-1: Schematic representation of the cluster geometries

Each circle represents a spherical cell. a-f represent the "linear geometries", g the "tetrahedral geometry." The shaded circle in each geometry represents the trailing cell. The double-sided arrows between geometries represent the possible transitions that may occur between steps in the simulation.

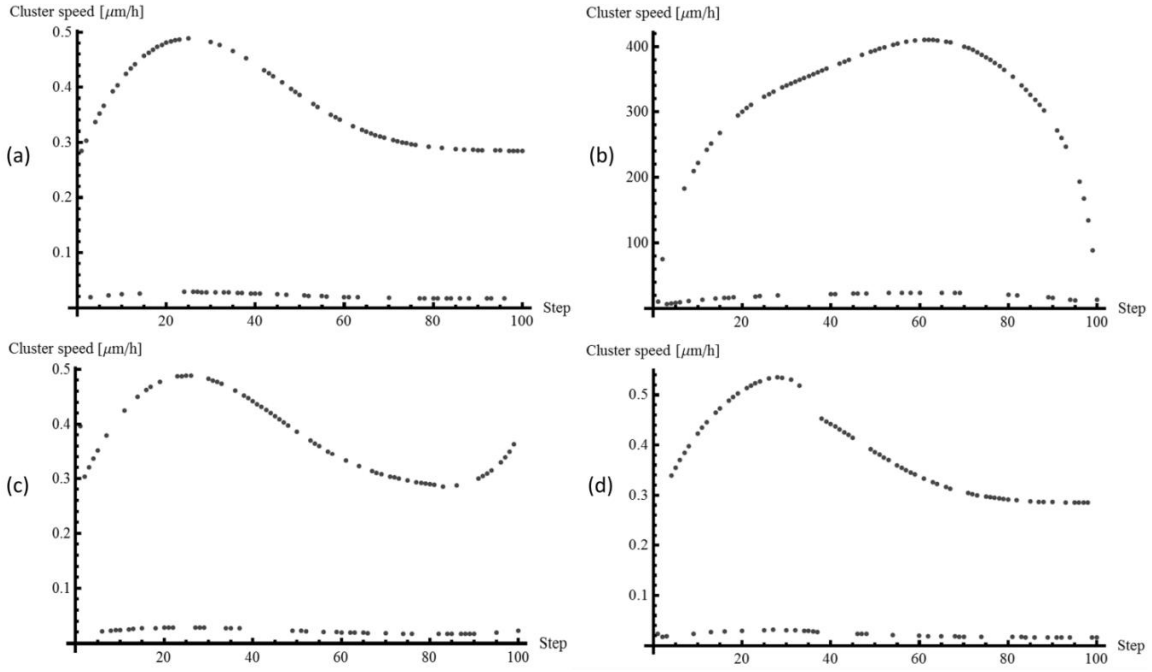

Figure 3-2: Velocity profiles implementing individual conditions

Simulations were run using a tetrahedral geometry. Each graph represents a different simulation in which each of four different conditions to address overpowering of ligand presence by MMP activity: a) Lowered MMP concentration. b) Increased initial ligand concentration. c) Modified traction force for cell with MMP activity. d) Complete localized ECM degradation.

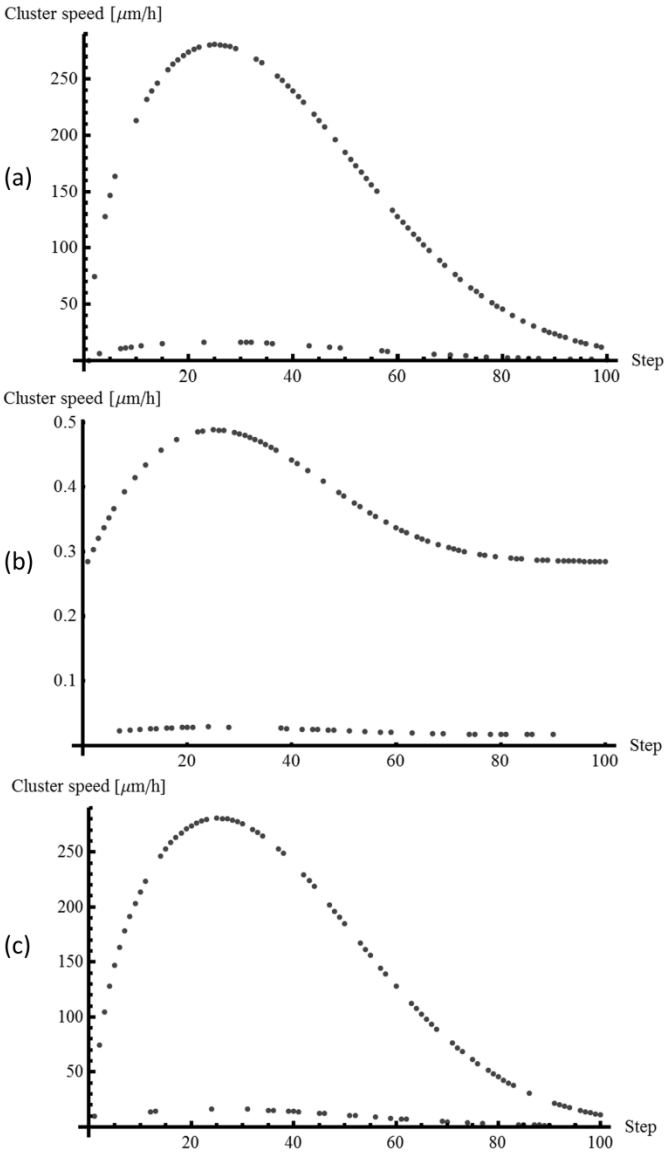

Figure 3-3: Velocity profiles implementing two conditions

Simulations were run using a tetrahedral geometry. Each graph represents a different simulation in which two conditions to address overpowering of ligand presence by MMP activity were simultaneously implemented: a) Lowered MMP and increased initial ligand concentrations. b) Lowered MMP concentration and modified traction force. c) Increased initial ligand concentration and modified traction force.

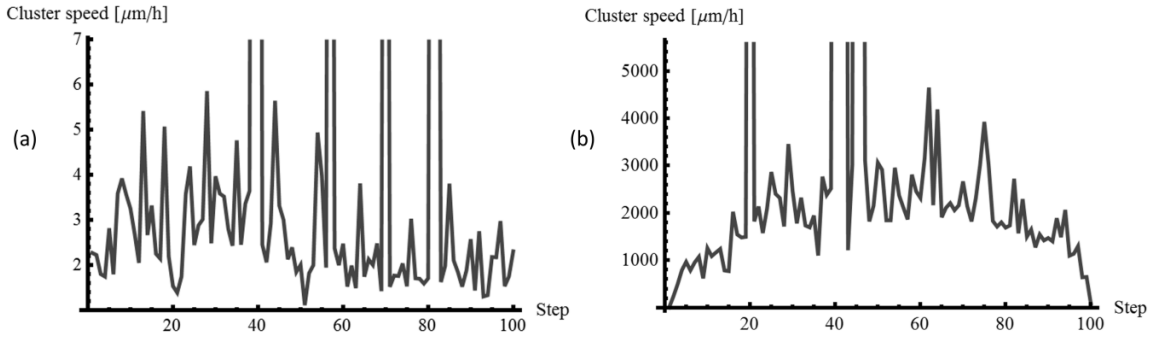

Figure 3-4: Sample simulations using multiple cluster geometries

Each run implements one of two of the four conditions (individually) used to address overpowering of ligand presence by MMP activity: a) Lowered MMP concentration. b) Increased initial ligand concentration.

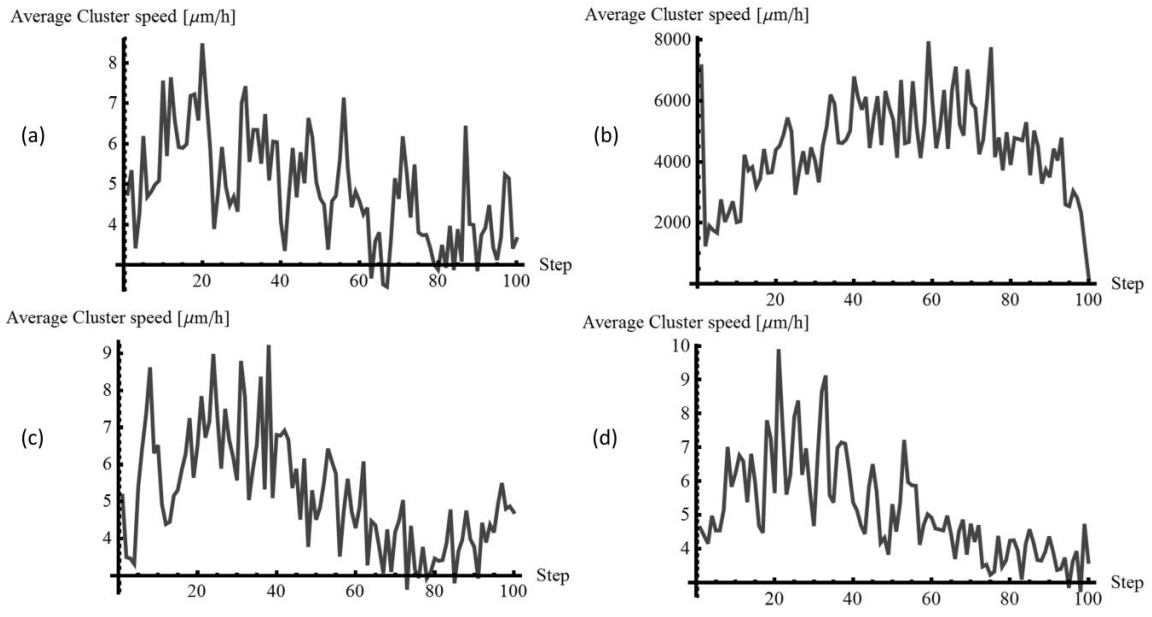

Figure 3-5: Average velocities for simulations implementing individual conditions for multiple cluster geometries

The simulations implement each of four different conditions to address overpowering of ligand presence by MMP activity: a) Lowered MMP concentration. b) Increased initial ligand concentration. c) Changing participation of traction force for cell with MMP activity. d) Complete localized ECM degradation. Averages are taken over 100 runs.

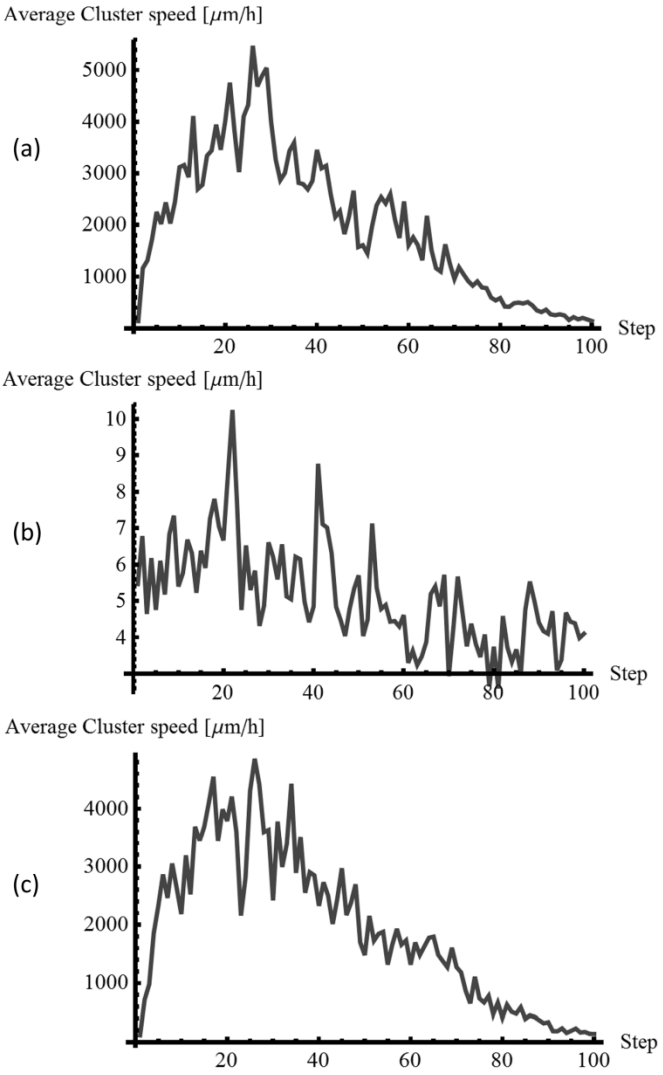

Figure 3-6: Average velocities for simulations implementing two conditions for multiple cluster geometries

Each graph represents a different simulation in which two solutions to address overpowering of ligand presence by MMP activity were simultaneously implemented: a) Lowered MMP and increased ligand concentrations. b) Lowered MMP concentration and complete localized ECM degradation. c) Increased initial ligand concentration and modified traction force for cell with MMP activity. Averages are taken over 100 runs.

CHAPTER 4. Epithelial to Mesenchymal Transition (EMT) Model

This chapter presents an agent-based model of the epithelial to mesenchymal transition (EMT), the process by which a whole epithelium loses its integrity and gives way to highly migrating cells or groups of cells (84). Characterized by the loss of cell-cell junctions and increased migratory activity, this process has not been fully described molecularly and the term is descriptive for epithelial discohesion; nonetheless, it is believed to occur in physiological process during development, such as in neural crest delamination, and the disruption of epithelium in carcinomas is indicative of a similar process (86, 87, 138).

Most experimental studies on EMT search for molecular markers indicating an epithelial or mesenchymal conformation, they focus on afferent signaling pathways received by cells undergoing this transformation; however, these approaches are unable to track mechanical changes in the cell and the possible role this plays in EMT (88). In order to address this gap in our understanding, a quantitative approach is developed to study population level effects of single cell changes typically occurring during EMT.

Similar to existing tumor growth computational models of cancer, the model presented in this chapter partitions space to define a cell and uses an elastic core to ensure volume exclusion. Cells are setup in a two-dimensional sheet over a discrete representation of the ECM. EMT is modeled by allowing cells to interact with each other and ECM fibers, dynamically forming cell-cell and cell-matrix adhesion complexes. By modulating the strength of cell protrusive force and different cell-cell adhesion dynamics,

the model reveals the impact of these factors on epithelial integrity and invasive capacity in EMT.

4.1 Introduction

During development of an organism or repair of many tissues, the ability of cells to change their behavior is crucial; cells can differentiate and dedifferentiate based on environmental cues to fulfill different tasks at different times. Although, both differentiation and migration are well known and studied processes, the exact quantitative nature of their relationship remains elusive. EMT is an example of an instance where modulation of this relationship can lead to very different and impactful outcomes. In EMT, polarized cells in the epithelium can undergo a transformation characterized by the loss of cell-cell junctions and increased migratory activity into non-polarized invasive cells (84).

The complexity of the changes that a cell must undergo to alter its phenotype reveal how difficult it is to define EMT specifically. One of the more characteristic changes cells undergo during EMT is the reduction of cell-cell adhesions (139, 140). Cells undergo what is known as the *cadherin switch*; in the epithelium, cell typically express E-cadherin, whereas mesenchymal cells express N-cadherin. This switch can be induced by either intrinsic or extrinsic signals (84). This step is believed necessary for epithelial coherence to be lost. Because cadherin molecules through catenin molecules are connected to the cytoskeleton, including F-actin, it is believed that changes in adhesion can activate pro migratory pathways. Specifically, p120-catenin represses the activity of RhoA and activates Rac1; both actions aide cell migration by contributing to

the formation of migratory membrane protrusions (141). Additionally, movement of β-catenin into the nucleus is associated with increased migration by modulating the expression of molecules such as L1-CAM, matrix-metalloproteases (MMP), and fascin (13).

Changes in cells during EMT affect mechanical properties of the cytoskeleton, cell-ECM, and cell-cell signaling, as well as genetic regulation. Furthermore, these are highly interrelated aspects of cellular life, governed by complicated quantitative relationships. It is for these reasons that a computational study may provide an avenue for investigating EMT. Until now, little has been done to study EMT from a computational perspective. Among the few studies reported, Ramis-Conde *et al.* present briefly an application of an agent-based model of tumor growth in the context of EMT. They model the kinetics of the E-cadherin and β-catenin binding and track waves of a rise in intracellular β-catenin concentration across cellular populations in a sheet (13). When briefly applying their model to a migratory population, the potential for disruption of the epithelial layer is shown, but they abstain from quantifying their results in this regard. The model presented in this chapter take advantage of both single cell migratory models and agent-based cell population models to explore molecular processes that coordinate and affect cellular behavior and interactions during EMT. The model was developed along with Dr. Oliver Bates and published in *Cells Tissues Organs* (142).

4.2 Model Formulation

4.2.1 Mechanical Representation of Cells and ECM

Similar to existing agent-based models, this model keeps track of individual cells using a Delaunay triangulation to partition space and track neighboring relations among cells (108, 143). Each cell is modeled as a sphere with an elastic spherical core with a radius of 75% of the total cell radius. This allows cells to come into contact while guaranteeing volume exclusion through repulsion forces that emerge when the elastic cores come together; corresponding area of interaction is approximated based on spherical contacts.

In addition to the position of the center of the elastic sphere, each cell is defined by its radius and concentration of cell membrane receptors (c_{rec}) and integrin concentration (c_{int}). c_{rec} and c_{int} are normalized relative to a maximum concentration, and therefore vary from 0 to 1. c_{rec} represents the relative presence of generic receptors for cell-cell interaction; c_{rec} can be taken to be the E-cadherin concentration in the simulations here presented. c_{int} represents the relative concentration of generic integrins that interact with the extracellular matrix (ECM) for cellular migration. Cell proliferation is ignored in these simulations to isolate the effects of a limited set of cellular properties.

The ECM is modeled as a set of discrete fibers, a novel approach compared to other studies where ECM is modeled as a continuum. The fiber network is created by first connecting all points of a cubic lattice with cylinders; the positions of the lattice points are shifted in a random direction by the same distance, and then each fiber is potentially cut based on a probability. The radius of each fiber is kept constant because the area of

interaction between cells and fibers is important in determining cellular traction forces. Each fiber has a quantity c_{lig} associated with it; this represents the concentration of peptides to which cells can attach through integrins. This quantity is normalized relative to a maximal value and kept constant for all fibers. Fibers do not move or change throughout the simulations.

4.2.2 Force Calculation and Migration

A force-based dynamics approach, similar that outlined in Chapter 3 for a cell cluster, was used to define motion of the cells. Each time step simulates the motion of each cell over 30s, during which all forces acting on the cell are summed. The sum of the forces is described by Equation 4-1:

$$\boldsymbol{F}_{tot} = \boldsymbol{F}_{prot} + \boldsymbol{F}_{el} + \boldsymbol{F}_{fib} + \boldsymbol{F}_{det} \tag{4-1}$$

$\boldsymbol{F}_{prot}$ results from the sum of protrusion forces due to lamellipodial extension and traction forces generated by each cell due to its attachments to the ECM fibers. Its initial direction is chosen at random at the beginning of each step. Because this force would only lead to movement if there is a substrate for the cell to exert force on, it is broken down into components by projecting the force onto the planes of each ECM fiber in contact with the cell ($\boldsymbol{F}_{pproj}$). At each point where force is exerted, a traction force opposing it is generated, so the projections are scaled based on two factors affecting traction: The first factor (A_r) is the ratio of the cell surface area of interaction with a particular attachment point over the area of interaction with all fibers. The second factor (β) is an adhesivity

parameter similar to that presented in Chapter 3 defined as the product of ligand concentration on the fiber and integrin concentration on the cell. Once scaled, the resulting forces are added to obtain the final protrusion force acting on the cell. Equations 4-2 and 4-3 display how this force is calculated for each cell; the subscript *f* is used to describe the identity of a specific fiber in contact with the cell:

$$\boldsymbol{F}_{prot} = \sum_{f=1}^{N} \beta_f A_{r,f} \boldsymbol{F}_{pproj\,f} \tag{4-2}$$

$$\beta_f = c_{int} c_{lig,f} \tag{4-3}$$

$\boldsymbol{F}_{el}$ represents the elastic repulsion forces that come into action if two cells come too close together. Equation 4-4, from contact mechanics, has been used in cell models (143) and describes the magnitude of the elastic repulsion force for two spheres *i* and *j* (in this case two cells):

$$|\boldsymbol{F}_{el}| = \frac{h_{ij}^{3/2}}{\frac{3}{4}\left(\frac{1-\upsilon_i^2}{E_i}+\frac{1-\upsilon_j^2}{E_j}\right)\sqrt{\frac{1}{R_i}+\frac{1}{R_j}}} \tag{4-4}$$

where h_{ij} represents the maximum overlap sphere *i* and *j* would have if they penetrate each other instead of deforming, *E* is the Young's modulus of the elastic mini-sphere, υ is the Poisson ratio, and *R* is the radius. Similarly, $\boldsymbol{F}_{fib}$ represents the elastic repulsion force

that comes into action if a cell and a fiber come to close together. Unlike cells, fibers are considered to be all rigid (no elastic core) and have a higher Young's modulus. This force prevents cells from moving across fibers. Its magnitude was approximated by calculating it with Equation 4 without using an elastic core for the fiber but using the actual radius of the fiber for *R*.

Finally, $\boldsymbol{F}_{det}$ is a small force acting on each cell pushing it towards all fibers with which it is in contact. Its magnitude is 10% of the projection of $\boldsymbol{F}_{prot}$ in the cell-fiber direction (closest distance); it is also scaled based on A_r and β. This force, with its small magnitude, is meant to compliment the pulling force moving each cell along a fiber since a cell cannot move along a fiber without attaching to it and changing shape. This force also prevented cells from becoming detached from the ECM in cases where elastic repulsion is high.

The displacement of each cell is calculated based on the total force acting on the cell. By taking into account that the Reynolds numbers for cellular motion in tissue are very small, an overdamped approximation is used, and the total force felt by the cell is related to the displacement $\dot{r}$ by Equation 4-5, where *r* is cell position (14, 99, 143).

$$\dot{r} = \frac{\boldsymbol{F}_{tot}}{\gamma_{tot}} \tag{4-5}$$

γ_{tot} represents the friction experienced by the cells upon motion. This term is a sum of multiple friction terms because hindrance in motion can be attributed to cell-cell attachments (γ_{cell}), cell-fiber attachments (γ_{fib}), and viscosity of the environment (γ_{visc})

due to extracellular fluid, hyaluronic acid, other glycosaminoglycans, and smaller fibrilar components of the ECM. These are defined in Equation 4-6, 4-7, and 4-8 for a cell *i*, where *j* and *f* are subindices to indicate adjacent cells and touching fibers respectively:

$$\gamma_{cell\ i} = \gamma_{max} \sum_{j=1}^{N} A_{s,ij} \frac{1}{2} \left(1 - \frac{\boldsymbol{F_{tot\ i}} \cdot \boldsymbol{n_{ij}}}{|\boldsymbol{F_{tot\ i}}|}\right) \left(c_{rec,i} c_{rec,j}\right) \tag{4-6}$$

$$\gamma_{fib\ i} = \sum_{f=1}^{N} \varphi A_{r,f}\ c_{int,i} c_{lig,f} \tag{4-7}$$

$$\gamma_{visc} = 6\pi\eta r_0 \tag{4-8}$$

Equation 4-6 was taken from the work by Schaller *et al.* (143); here $A_{s,ij}$ is the contact surface area of the two spheres *i* and *j*, γ_{max} is a friction parameter, and $\boldsymbol{n}_{ij}$ is the vector from the center of cell *i* to cell *j*. In Equation 4-7, φ is a parameter representing the contribution to friction by each ligand-integrin bond. Following the Stokes-Einstein equation, because cells are modeled partly by spheres, Equation 4-8 uses the viscous resistance of the ECM, η.

A check is in place before finalizing the migration step for each cell. This check ensures that the cell would potentially be able to move from the new position, specifically whether a fiber would be close enough for the cell to reach it with its protrusions. If no fiber is within the cell radius, then the movement is recalculated without the protrusion

force; that is only the elastic forces with respect to other cells and fibers are taken into account. This part of the simulation makes the assumption that a cell moves no more than as far as it could prod with its membrane projections; this is particularly true when the time step chosen (30s) is equivalent to a fraction of the cell's total migration cycle (~600s).

4.2.3 Model Implementation and Simulated Conditions

The system is initialized by creating a sheet of cells representing the epithelial layer over a dense set of fibers representing the ECM underneath the epithelium. In the plane of the sheet (referred to as xy-plane), cells are placed in a hexagonal lattice initially equidistant from each other. The cells have a radius of r_0 = 4.9 μm, and each cell is placed at $0.98 \times r_0 \times \sqrt{3}$ μm from each other and then moved randomly in both the x- and y-positions by a randomized fraction of the distance 0.5μm. Similarly their z-position is randomized within 1μm of the plane. It is the initial z-position before randomization of the cells that is used to track invasion of the invasive cells leaving the layer into the ECM. The layer is formed by 418 cells and is close to squared; cells at the edge of the sheet are not allowed to move. This initial configuration was chosen such that cells would all start tightly packed to prevent the sheet from losing its shape by expanding its boundaries.

The fiber network was initialized at the beginning of every simulation as well. Figure 4-1 depicts this initial configuration. The lattice points defining the fiber network were positioned 11 μm from each other and displaced by 9 μm. There was a 30% chance of each fiber being cut. These numbers were chosen such that the resulting fiber network

would have an approximate average fiber length of 15 μm as was found by confocal reflectance microscopy in collagen gels used in *in vitro* cell migration studies (144). This resulted in approximately 8000 fibers in a space of approximately 5×10^{-3} mm^3. The extent of the matrix in x- and y- directions was the same as the epithelial layer, and it was 200 μm in the z-direction (arbitrary choice such that no cell would migrate to the end of the matrix in this direction). The radius of the fibers was chosen to be 0.5 μm.

Each simulation consisted in setting up the epithelial layer over the ECM and letting the cells move for equivalent to 3 days (8640 steps). Two different parameters were changed in the different simulations: First, magnitude of $\boldsymbol{F}_{prot}$ and, secondly, the mechanism by which E-cadherin concentration is controlled. Two different constant values of the protrusion force magnitude were used, defined from now on as the low force and high force: Low value is $|\boldsymbol{F}_{prot}|$ = 0.0025 μN, and the high value is $|\boldsymbol{F}_{prot}|$ = 0.005 μN. These values were chosen heuristically; the low magnitude represents the lowest protrusion value with which a cell may detach from a cell mass (*e.g.* tumor or cell sheet), and the high magnitude represents the highest possible force with which cells move without causing high repulsion elastic forces with fibers.

The E-cadherin concentration was either left constant at c_{rec} = 1.0 or allowed to vary for each cell moved based on the changing surface area of interaction with all neighboring cells as described by Equation 4-9. These settings will be referred to from here on as *constant cadherin concentration* (CC) and *dynamic cadherin concentration* (DC), respectively.

$$\Delta c_{rec} = \sqrt{\frac{\Delta A_s}{4\pi r_0^2}} \tag{4-9}$$

where ΔA_s is the change in area of interaction with all neighboring cells at each step. $4\pi r_0^2$ represents the maximum change in area of interaction (*i.e.* surface area of the cell).

By considering all combinations of the protrusion force magnitude and E-cadherin concentration regulatory mechanisms, four different conditions are simulated. Each condition is run ten times and three quantities measured every 2880 steps (1 day): 1) Number of cells that leave the layer, defined as number detached cells at least at three cell radii distance from the initial z-position. 2) Percentage of initial number of cells that remain in layer, defined as percentage of cells within 2 μm from initial layer z-position. This is meant as an approximate measure of epithelial layer disruption. 3) Average depth of penetration of invasive cells.

4.3 Results

4.3.1 Intercellular Adhesion Impacts Invasion More than Membrane Protrusion

First, the number of cells that detached from the cell sheet are quantified in the different conditions. Figure 4-2 shows the number of cells that detach from the epithelial layer and make it a distance of at least three cell radii from the initial position into the fiber network (*i.e.* in the z-direction).

These results show how having a high protrusion force or being able to reduce, even temporarily, cell-cell attachments is enough to cause a cell to leave the epithelial layer; Figure 4-2 shows how individually these characteristics are enough to trigger

cellular exodus. No cell left the layer in the CC/LF condition. Also, in all simulations implementing the CC/HF condition, only a single cell left the epithelial sheet in a single simulation. This suggests that a cell losing its cadherin junctions is more relevant to EMT than increased migration activity; however, the average number of invasive cells, taking into account variance of the results, is close in the CC/HF and DC/LF conditions.

4.3.2 Epithelial Disruption Occurs Soon After Dysregulation

The results also suggest that there is no significant increase in the number of invasive cells as a function of time; most cells leave the epithelial sheet in the first day. The progression of epithelial sheet deformation reveals a possible reason for this observation. Figure 4-3 shows images of the system at day 3 for each of the four conditions used in the simulations. The epithelial sheet breaks up into cell clusters as a function of time. The progression of cell detachment with time suggests that a cell is more likely to detach from a single-cell layer than a circular cluster.

This is explained by the difference in total contact area between cells in a sheet versus in a bulb shaped cluster. This result may be a model-specific observation that does not hold true if cells are not modeled as elastic spheres. Progressive clustering of cells in the sheet seems to be more drastic in the simulations where cells move with the high protrusion force (HF) and especially with the CC/HF condition (Figure 4-3b). When the protrusion force is high, but cells still have strong cell-cell junctions, it may be more likely for cells to move towards other cells than away into the ECM.

4.3.3 Epithelial Sheet Disruption Evolves Independently of Cadherin Regulation

Figure 4-4 shows the average fraction of cell remaining in the epithelial sheet for each condition and characterizes the sheet's shape change for all simulations. This is a metric inversely related to membrane disruption. Membrane disruption seems to advance at the same rate independently of the method of cadherin regulation. Taking into account the observed clustering, it is not immediately apparent that at every checkpoint (*i.e.* each day), the average values of the fraction remaining in the sheet are practically equal for simulations where cells have the same protrusion force independently of cadherin regulation. This suggests it may be the high protrusion force that causes the clusters to grow in the z-direction away from the ECM and pushes cells off the plane even when a high and constant cadherin expression leads to clustering. Additionally, there is less layer disruption in the conditions where cells move with the low protrusion force (LF). This occurs because it would be less likely for cells to return to the layer if the cell sheet itself has not clustered reaching deeper into the fiber network.

Membrane disruption due to single cell migration into the ECM appears to be minimal. Even in cases where a relatively high number of cells leave the sheet it is merely ~2% of all cells; most of the disruption is due to cell rearrangement within the sheet. While Figure 4-2 shows no significant change at each checkpoint after day 1, Figure 4-4 shows a steady decline for all conditions in the average fraction of cells remaining in the layer.

This steady decline confirms that while cells are active all throughout the simulation they can only escape the sheet in the first part of it. It is much harder for a cell

to leave a cluster than a sheet because the part of its surface area that interacts with other cells is much higher than when in a sheet. This new position within the cell collective hinders its motion due to the increased cell-cell attachments as well as the more limited access to fibers. Nonetheless, even if cells cannot move as easily individually, those at the edges of a cluster do impart force and, due to volume exclusion, the repulsion forces continue to push the cluster away from the fiber network causing the progressive drop of the fraction remaining in the sheet.

4.3.4 Hindered Transport Plays a Role in Single Cell Migration

Finally, the depth of migration of cells into the fiber network is quantified. Figure 4-5 shows the average penetration depth for all cells along with the maximal penetration observed during all simulations for the four conditions considered. Most surprising is that the average invasion depth for simulations with the DC/LF condition was comparable to the two conditions where cells attempted to move with the high protrusion force (CC/HF and DC/HF). This can be attributed to the phenomenon of *hindered transport*, previously observed in studies of motion of spherical particles in fibrous media; this phenomenon consists of a deeper penetration by the particles in question when there are fewer other particles in its surroundings to collide hindering each other's movements (145).

4.4 Discussion

The EMT model suggests cell clustering is important in epithelial sheet disruption. It demonstrates the ability to probe the impact of cell-cell adhesion and protrusive forces in epithelial integrity. Specifically, it shows how cell-cell adhesion

impacts invasion more than the strength of the membrane protrusion force. More importantly, it shows that both physical and biochemical regulation of interactions in cell collectives can account for the rise of collectivity. This is a difficult relationship to discern experimentally in 3D. Recent work placing collagen matrices between microfluidic channels, has provided a way to measure to effect of chemotaxis in 3D (146). This work has revealed the effect of growth factor concentration gradients on a brain cancer cell line (U87MG). By using coupled convection-diffusion equations solved with commercial finite element solvers, it shows how the spread of factors can be modelled in collagen type I gels. These same methods could be applied to our EMT model to study the combined effects of paracrine signaling, MMP secretion, and chemotaxis on epithelial cell invasion.

Evidence that *hindered transport* plays a role in single cell migration demonstrates the importance of accounting for physical phenomena when studying cells. In the simulations analyzed in this chapter, although the ECM was randomized in every simulation, the distribution of fiber length and diameter always matched *in vitro* measurements. Additional factors not considered, such as matrix remodeling, are examples of biochemical contributions not exclusively physical, that define the cellular environment that certainly impact cell migration. Measurements done with confocal reflectance microscopy have revealed the change in fibril fraction and pore size in collagen gels with the presence of cells (144). These measurements can be used to model matrix remodeling realistically; however, such an effort should take into account the mechanical effect of remodeling. Cells sense their environment and reorient based on

mechanical stretch (147). Remodeling of the environment will affect strain of the fibrillary structures of the ECM, which in turn will affect the behavior of the epithelial cells. Calculating the change in stresses that come with remodeling of the ECM is a difficult tax given the heterogeneous nature of the ECM. Such models looking at the change in mechanical properties of a fibrillary network have been developed for 2D systems (148). Their expansion to 3D would be rewarding given that metastatic cells are known to migrate down density gradients (149). Inclusion of these considerations in the EMT model would provide a way to spatially monitor the relation between ECM density, ECM remodeling, and cell migration. Currently, only well-defined interphases between different environments have been studied experimentally. The model here presented has the potential to look at migration in a simulated environment accounting for the dynamic nature of the ECM.

The results displayed in Figure 4-4 raise the question as to whether or not EMT causes an epithelial layer disruption, since most of the disruption occurs due to cell rearrangement within the sheet. Boyden chamber experiments analyzing the genetic expression of factors associated with EMT in the more migratory cells (*i.e. snail* and *slug*) have helped characterize what characteristics make epithelial cell more invasive, confirming the downregulation of E-cadherin in invasive cells (150). The results obtained in our simulations suggest that epithelial sheet disruption can evolve independently of cadherin regulation; however, there is little invasion unless cell-cell junctions are broken and then reformed.

Collectively, the observations presented in this chapter show that the EMT model

can provide insight into epithelial dysregulation, but similar to the rigid cluster model presented in Chapter 3, it lacks a more realistic description of cell-cell junctional regulation, necessary for the emergence of cell collectives. Nonetheless, the EMT model is computationally intensive, with its demanding partitioning of space and discrete ECM. To exclusively describe collective motion, a computational model could focus on intracellular regulation of cell-cell adhesion rather than cell-matrix interactions.

4.5 Tables

Parameter	Value	Units	Reference
Integrin concentration on cell, c_{int}	1.0	No.	Fixed
Ligand concentration on fiber, c_{lig}	0.5	No.	Fixed
Cellular (mini sphere) Young's modulus, E	5×10^{-3}	MPa	(151)
Fibrilar Young's modulus, E	1×10^{-2}	MPa	Assumption
Cellular (mini sphere) Poisson ratio, υ	0.5	No.	Assumption
Fibrilar Poisson ratio, υ	0.5	No.	Assumption
Cell-cell friction parameter, γ_{max}	5×10^{-3}	kg / μm^2 / s	Estimated
Ligand-integrin friction per bond, φ	1.0	kg / s	(99)
Viscosity of ECM, η	1×10^{-3}	kg / μm / s	(151)

Table 4-1: Parameter values for force calculation in EMT model

4.6 Figures

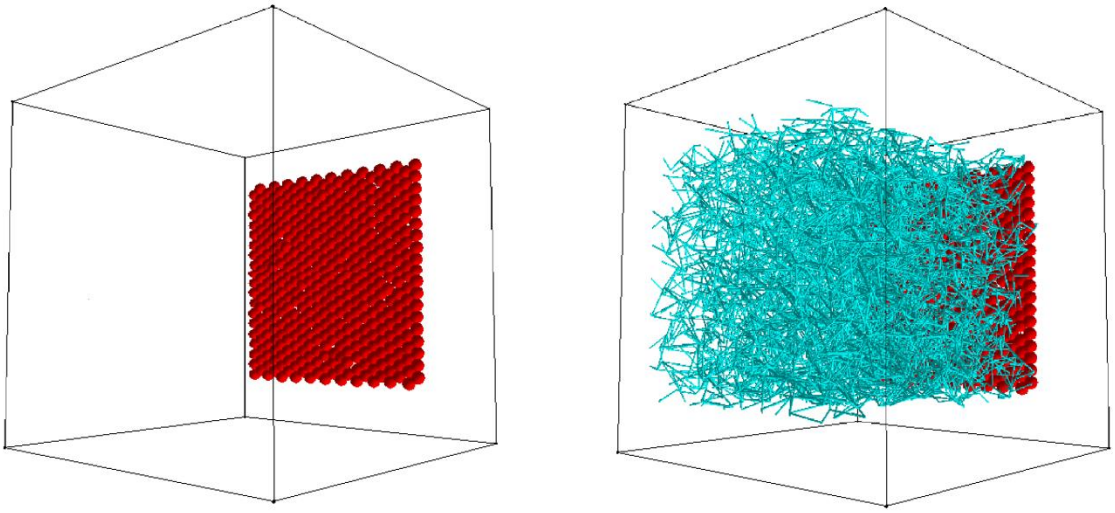

Figure 4-1: Initial configuration of EMT simulation

Cells, shown in red, in a hexagonal lattice forming a sheet (left) over discrete fibers, shown in cyan, representing the ECM (right).

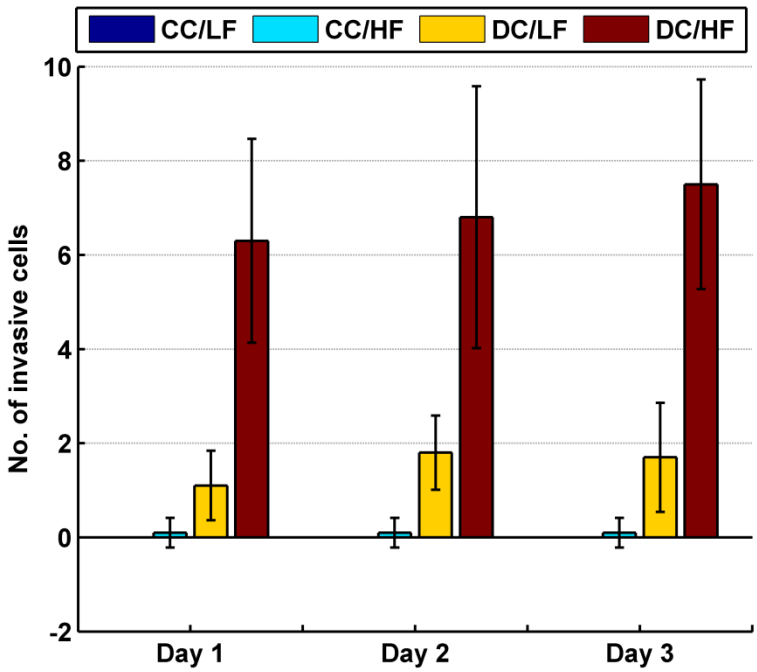

Figure 4-2**:** Number of cells leaving epithelial layer

Values recorded at 1, 2, and 3 days for the four different conditions. CC = constant cadherin concentration, DC = dynamic cadherin concentration, LF = low protrusion force magnitude, HF = high protrusion force magnitude. Average was calculated over ten simulations; error bars represent one standard deviation.

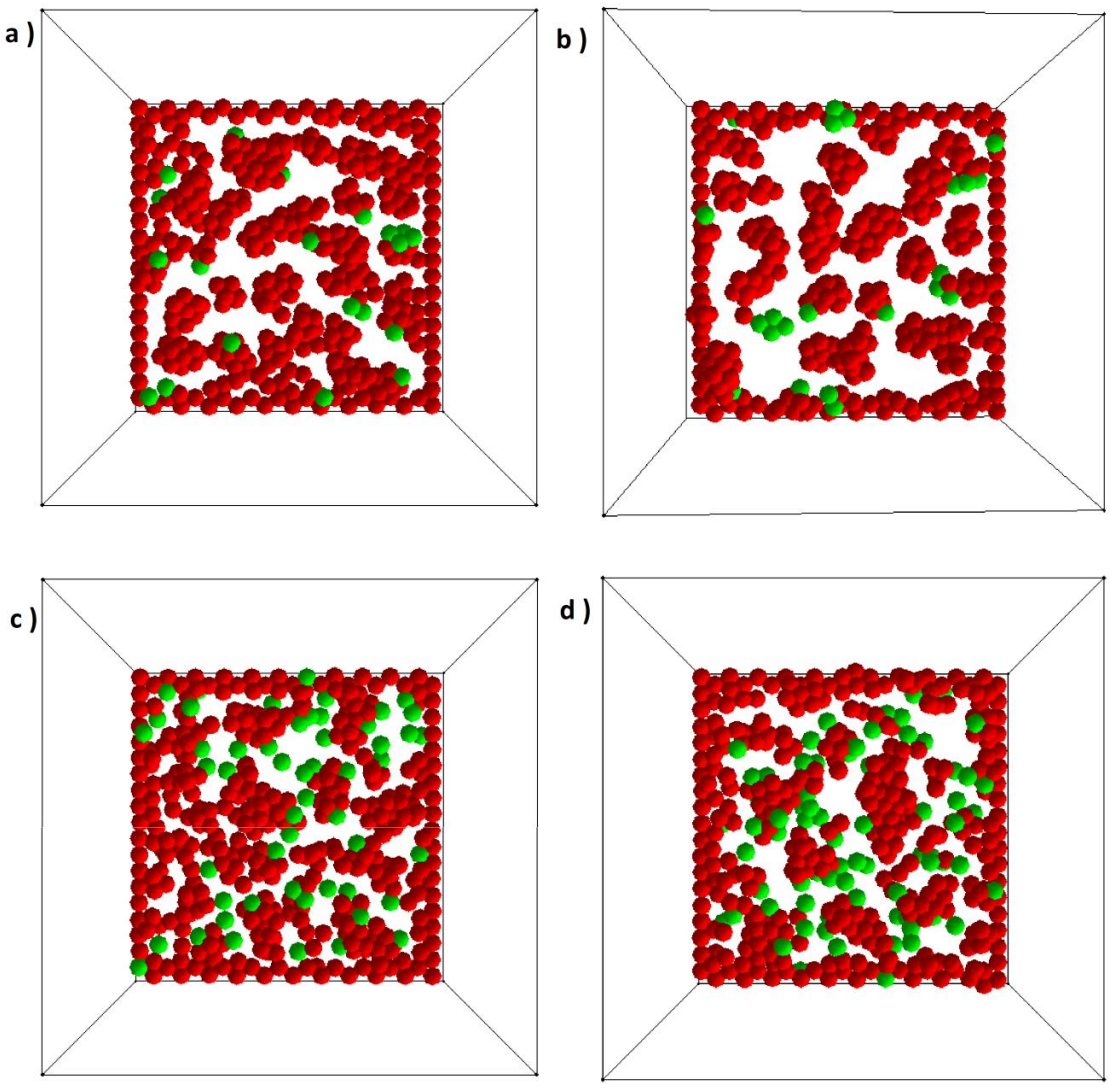

Figure 4-3**:** Final conformation of the cell sheet in EMT simulations

Each image shows a sample conformation at day 3 for the four different conditions used in the simulations: a) Constant cadherin and low protrusion force (CC/LF). b) Constant cadherin and high protrusion force (CC/HF). c) Dynamic cadherin and low protrusion force (DC/LF). d) Dynamic cadherin and high protrusion force (DC/HF). Red cells are under tension above a certain value (1 Pa) and less likely to become loose than green cells, with tension below this value.

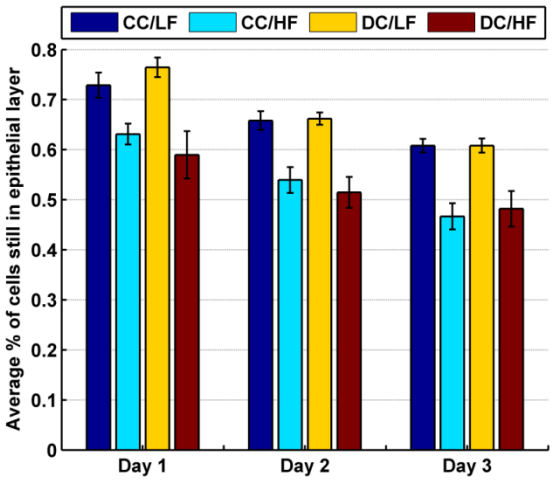

Figure 4-4**:** Cells maintaining epithelial integrity

Values correspond to cells within 2 μm from initial layer z-position at 1, 2, and 3 days for the four different conditions. CC = constant cadherin concentration, DC = dynamic cadherin concentration, LF = low protrusion force magnitude, HF = high protrusion force magnitude. Average was calculated over ten simulations; error bars represent one standard deviation.

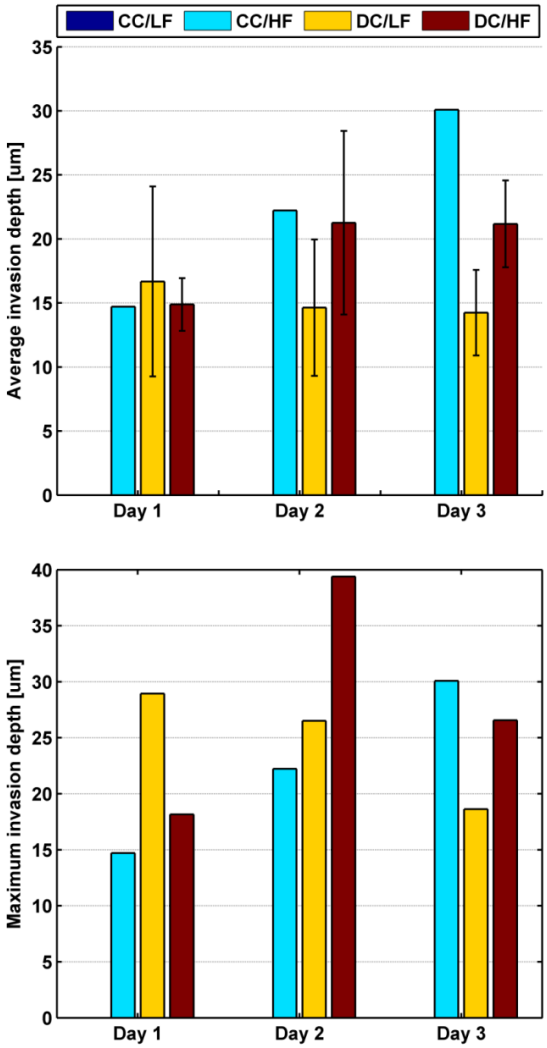

Figure 4-5**:** Cellular invasion into ECM

Values correspond to average invasion depth of cells that left the epithelial layer into fiber network at 1, 2, and 3 days for the four different conditions (top) and maximum invasion depth for all simulations at 1, 2, and 3 days for the four different conditions (bottom). CC = constant cadherin concentration, DC = dynamic cadherin concentration, LF = low protrusion force magnitude, HF = high protrusion force magnitude. For top graph, average was made over ten simulations; error bars represent one standard deviation.

CHAPTER 5. Intracellular Regulation of Intercellular Adhesion

This chapter presents a first numerical model of the network composed of the evolutionarily conserved Wnt/β-catenin signaling pathway, protein N-glycosylation, and E-cadherin-mediated intercellular adhesion. This regulatory cell network (RCN) plays pivotal roles in determining the balance between proliferation and adhesion during development and in maintaining homeostasis in differentiated tissues (56, 58). The different pathways have been studied independently; however, little insight has been gained about the dynamics of their interaction.

Considering the large number of molecules involved and their changing levels of expression with time, the wide range of plausible cellular states are evident. Thus, the study of the network merits use of mathematical modeling, allowing for quantification of any molecule included in the model. A system of ordinary differential equations (ODEs) was used to describe the reactions using kinetic reaction rates obtained from literature. Activation of the Wnt/β-catenin pathway with Wnt3a was simulated to determine the resulting fold-change in the molecular concentrations at multiple time points.

Local sensitivity analysis (LSA), performed on the mathematical description of the network, reveals the importance of N-glycosylation in the regulatory network, confirms the importance of the molecule axin in β-catenin degradation, and provides a measure of the relative importance of the component pathways. The model's predictions are validated by inhibiting β-catenin co-activation of *DPAGT1* in MDCK cells with a small molecule inhibitor. Notably, the model predicts the relative change in stability of cell-cell junctions with inhibition. Through this numerical exploration of the dynamic

regulation of AJs in epithelial cells, the model can be further used to gain insight into intercellular interactions in cell collectives.

5.1 Introduction

Many cellular processes are highly conserved in evolution with a small set of proteins constituting a regulatory skeleton of cellular control (152). These regulatory proteins have been shown to exhibit pathway fidelity; however, due to their limited number, it is increasingly clear that different pathways form intricate regulatory networks that share these proteins. Understanding these regulatory mechanisms is likely to provide important new insights into interactions among multiple pathways in physiological and pathological processes. Here focus is placed one such RCN formed by the pathways: Wnt/β-catenin signaling, protein N-glycosylation, and E-cadherin-mediated adhesion. Study of this network is critical because of its functions in building and preserving tissue, and when awry, it has been associated with detachment of cells from the epithelium and increased cellular migration (16, 153).

Figure 5-1 provides a broad representation of the relation between the pathways constituting the network (9, 16). This representation is insufficient to predict cellular behavior when we consider the large number of interacting molecules, their spatial organization, and the extensive crosstalk. Furthermore, rather than considering the effect of one pathway on another static, the varying molecular concentrations in time can cause the pathways to affect each other in contradictory ways at different times. For this reason, study of the network merits use of mathematical modeling allowing quantification of any reaction and molecule in the RCN. In a first model of the Wnt/β-catenin signaling

pathway, the Lee model, reaction kinetics were used to describe the concentration and effective half-life of ABC (154). This RCN model is based on the Lee model and "descendant models" and has been expanded to explore the feedback loops in the network; it is the first cellular network numerical model to take into account the cross-talk between Wnt/β-catenin signaling and N-glycosylation. The effect of this cross-talk on E-cadherin mediated intercellular adhesion is analyzed and used to predict the effect of inhibiting β-catenin co-activation of *DPAGT1*. Agreement between simulated and experimental responses to activation with Wnt3a provides confidence about the predictive capability of the model.

5.2 Model Formulation

A reaction scheme was designed according to the current understanding of pathways comprising the RCN (Figure 5-2). The entire scheme comprises 26 processes. In broad terms, the reactions can be classified as those pertaining to Wnt/β-catenin signaling and β-catenin regulation (reactions 1-10), genetic activation of *DPAGT1* and N-glycosylation (reactions 11-19), and E-cadherin recycling and AJ formation (reactions 20-26).

Reactions 1-10 are a simplified version of the Lee model (154), differing in its simplification based on results obtained by Benary *et al.* from a minimal model (155). Additionally, the RCN model differs from the Lee model in two ways: First, whereas the Lee model uses Wnt3a presence as a switch that when "ON" it activates the protein Dishevelled, which facilitates the interaction between axin and LRP5/6 (156), the proposed scheme assumes a direct interaction between Wnt3a, LRP5/6, and the BDC

(157). Second, the RCN model includes another source of β-catenin accounting for early association of β-catenin and E-cadherin in the ER (55, 158, 159). To ensure that these changes did not affect the output of the model, the steady state concentrations of the shared variables in the Lee and the RCN models in the presence and absence of Wnt3a were compared. No major discrepancies were observed (Table 5-1).

The reaction scheme was first represented mathematically as a set of ODEs with kinetic rates derived from literature (55, 154, 155, 158–161). When the system is solved with these parameter values, it is said to be in the *reference condition*. The complex formed by β-catenin and TCF was assumed to function as a transcription factor complex, driving the expression of GPT: Transcriptional induction was modeled as a Hill-type activation. This has been demonstrated to be appropriate for this system (155). The transport of E-cadherin between the cellular pools was modeled with fixed rates. A list of the ODEs can be found in section 5.7.1.

The rates at which membrane E-cadherin/β-catenin complexes can assemble into or disassemble from AJs were made functions of an adhesivity factor (σ) for the pools of E-cadherin in the membrane and AJs, respectively. This time-dependent factor is calculated for E-cadherin pool in the ER upon synthesis as a function of GPT concentration and updated for other pools based on E-cadherin transport rates. This value is normalized to the maximum concentration of N-glycosylated E-cadherin that can be synthesized in a single step (heuristically determined). The value is 0 when E-cadherin is the least adhesive, and it is 1 when the most adhesive. A detailed explanation about this factor can be found in section 5.7.1.

To reduce the number of parameters, the ODEs were simplified into a system of differential algebraic equations (DAEs) based on two assumptions: rapid equilibrium approximation for reactions 1, 2, 6, 8, and 11 (Figure 5-2) and conservation of constitutive molecules (*i.e.* Wnt3a, APC, TCF, Axin/GSK-3β complex). The system of DAEs consists of 15 ODEs and 9 algebraic equations with 15 independent variables and 9 dependent variables and can be found in section 5.7.3. The dynamics are described by 35 parameters; a complete list of parameter values along with their sources is included in Table 5-2. For further explanation of how parameter values were chosen, see section 5.7.4.

5.3 Numerical Analysis

With a mathematical description of the system, robustness to variations in parameters is tested. The different values correspond to different cellular conditions. Fold-change in the levels of β-catenin, rather than absolute abundance, determines the extent of Wnt/β-catenin signaling activation and its effects on downstream targets (155, 162); for this reason, fold-change was used to test system response to different conditions. Fold-change is defined as the ratio of the concentration for the molecule after stimulation with Wnt3a (Wnt "ON" state) to the equilibrium concentration for the molecule before stimulation (Wnt "OFF" state).

System sensitivity was tested by performing a LSA. This consists in varying kinetic parameter values independently for Wnt "ON" and Wnt "OFF" states. The system of DAEs was solved for specific time points after activation with Wnt3a, and the corresponding fold-change values were calculated. This approach finds which reactions

in the scheme are the most relevant in determining the fold-change response of individual molecules in the RCN. Two parameters were excluded from LSA: total amount of Wnt3a (WNT^0) and the Hill coefficient describing binding of the co-transcription factors to *DPAGT1*. The former was excluded because it is used to define fold-change, the metric used for analysis. The latter was excluded because as a power term, it significantly complicates analysis, and because Benary *et al.* showed the relative insensitivity of the system to this parameter (155).

Individual parameter values were varied over two orders of magnitude in a uniform logarithmic distribution, one above and one below the physiological value. For this variation, sensitivity of each variable to change in a parameter was defined by Equation 5-1 (163):

$$S_{ij}(t) = \frac{\frac{(X^{Wnt}/X^0)_{ij}}{(X^{Wnt}/X^0)_{ip}} - 1}{F - 1} \tag{5-1}$$

where X^{Wnt}/X^0_{ij} is the fold-change in variable X (defined as the ratio of the value of X in the Wnt "ON"case to the value of X in the Wnt "OFF" state) calculated for variation in the ith parameter over j values. F is the factor by which the physiological parameter value ($j = p$) has been multiplied to get the jth parameter value. To reach a single value of sensitivity of a variable to a single parameter, the values of S_{ij} are averaged over all j. Steady-state concentrations for both Wnt "OFF" and "ON" conditions were calculated using a numerical solver in Mathematica 10.2 (Wolfram Research, Champaign, IL).

5.4 Experimental Validation

5.4.1 Cell Culture, Transfections, and Lysing

For protein quantification, MDCK cells (NBL-2, ATCC) were plated at $3x10^4$cells/cm^2 in DMEM media (Gibco) supplemented with 10% fetal bovine serum (FBS) and 1% penicillin/streptomycin. To determine the effect of activating Wnt/β-catenin signaling, cells were serum starved (1% serum) for 24h then grown in two separate states: a *constitutive state* with endogenous Wnt3a expression and an *activated state* with added Wnt3a in the form of conditioned media. The *constitutive state* implied using 50% conditioned medium isolated from either L-mouse fibroblasts (control conditioned media or CCM), while the *activated state* implied using 50% conditioned medium from L-mouse fibroblasts stably expressing Wnt3a cDNA (Wnt3a conditioned media or WCM) (ATCC). These conditions are equivalent to the simulated Wnt "OFF" and Wnt "ON" states, respectively, in the numerical simulations.

To determine the effect of dysregulation of the RCN, cells were either treated with 25 μM ICG-001 in 0.05% DMSO (Selleck Chemicals, Houston, TX) or only DMSO as a control. ICG-001 is a Wnt/β-catenin inhibitor that acts by binding cyclic AMP response element binding protein (CBP) antagonizing β-catenin/TCF-mediated transcription; by binding CBP, ICG-001 prevents its binding to β-catenin (164). When cells reached no more than 30% confluency (3 days), cells were processed for preparation of total cell lysates (TCLs).

For assessment of the effect of *DPAGT1* upregulation on ABC expression to fit parameters from the N-glycosylation pathway, MDCK cells (NBL-2, ATCC) expressing

recombinant *DPAGT1*, were obtained by transfection of passage 2 cells with *DPAGT1* cDNA (Refseq NM_001382, Origene) at 80–90% confluence using Lipofectamine 2000. Controls included untransfected cells and cells transfected with a control pCMV6-Entry vector. After 14 h, the media were changed, and cells were divided into several plates. Media were changed every 2–3 days and supplemented with G418. After two weeks, cells were processed for RNA isolation and preparation of TCLs.

To record collective migration dynamics, MDCK cells (II-G) with green fluorescent protein (GFP) conjugated E-cadherin (gift of James Nelson, Stanford University) were plated at $6x10^4$cells/cm^2 in a 24-well plate. Cells were kept in DMEM media supplemented with 10% FBS and 1% penicillin/streptomycin. Cells were serum starved (1% serum) for 24h then grown in the presence of 50% conditioned medium (controlled conditioned media or Wnt3a conditioned media) (ATCC). To determine the effect of a perturbation in the RCN, cells were either treated with 10 μM ICG-001 in 0.1% DMSO (Selleck Chemicals, Houston, TX) or only DMSO as a control. When cells became confluent (3 days), the scratch-wound assay was performed.

5.4.2 Immunoprecipitation

Aliquots of TCLs containing 250μg of protein were used for each immunoprecipitation reaction. First aliquots were precleared with protein A/G PLUS-agarose beads (Santa Cruz Biotechnology) and anti-fibronectin antibody (BD Biosciences, mouse monoclonal) for 30 min at 4°C. Next, 2μg anti-E-cadherin antibody (BD Biosciences, mouse) was used for immunoprecipitation (2h at 4°C) followed by adsorption to protein A/G PLUS-agarose beads (1h at 4°C). The immunoprecipitate was

recovered via centrifugation (12,000×G), then washed thrice with 1X-PBS, and then boiled twice in 25μL 2X-SDS sample buffer. Elutions for each sample were combined and saved for immunoblot.

5.4.3 Immunoblots

TCLs were fractionated on 4-20% gradient SDS-PAGE, transferred onto PVDF membranes and processed as described (70). The following antibodies were used: anti-E-cadherin (Millipore, rabbit polyclonal), anti-α-catenin (BD, mouse monoclonal), anti-ABC (Millipore, mouse monoclonal), and anti-GAPDH (Novus Biologicals, mouse monoclonal).

5.4.4 Scratch-wound and Imaging

When cells were confluent, approximately 3 days after exposure to conditioned media and ICG-001, the cell monolayer was scratched with a 200μL pipette tip. Immediately following this, cells were washed with media with same contents of conditioned media and ICG-001 to clear debris before replenishing media. Cells are placed on a stage incubator and imaged every 30 minutes for 15 hours. The field of view (FOV) was chosen such that the wound split the FOV in half. Bright field and fluorescent images are acquired with a DMI600B Microscope (Leica, Solms, Germany) and ImagEM EM-CCD Camera (Hamamatsu Photonics, Hamamatsu, Japan) using a spinning disk confocal setup (Yokogawa, Tokyo, Japan). Micro-Manager 1.4 Software (http://www.micro-manager.org) employs a 10X 0.3 NA objective lens to image multiple ~576 × 576 μm^2 FOV.

For leading edge speed quantification, the fluorescent images of the wound edge are analyzed using a custom script developed in MATLAB (Mathworks, Natick MA): The leading front is defined as the average foremost detected fluorescence along the wound. Leading edge speed is calculated by looking at the time it takes for the average front to reach the end of the FOV.

5.4.5 Particle Image Velocimetry

PIV analysis is performed on bright field images. The displacement field (optic flow) was calculated using an ImageJ plugin (165). This PIV code uses an iterative scheme; in three subsequent iterations, the displacement is calculated by a normalized correlation coefficient algorithm that compares displacement in an individual interrogation window with a larger searching window. This method avoids a false correlation peak due to insufficient features (166).

5.5 Results

5.5.1 LSA and Processes Ranking

Focus is placed on the fold-change in ABC, GPT, AJ, and the adhesivity factor (σ) for different values of the parameter describing the binding between β-catenin and TCF (reaction 11, Figure 5-2). These four variables were chosen because they represent common nodes to the different component pathways of the RCN. Fold-change was calculated at multiple time points after activation with Wnt3a: every 100min from 1-900min and every 12h between 24-72h. Figure 5-3 shows the resulting fold-change values. In the *reference condition* (*i.e.* parameter values derived from literature and

corresponding to physiological values), the system reached steady-state at t=35h. Analyses at 48h and 72h are included because the time it takes for the system to reach a steady-state is not measured for the different parameter values tested.

Sensitivity of these molecules to changes in all other reaction kinetics were calculated at steady-state and shown as bar graphs in Figure 5-3. For corresponding results for all other variables see Figure 5-4. These relative sensitivity values of a molecule to a single process can be averaged over all molecules to provide a global ranking of the robustness of the RCN to each process. This ranking can be found in Table 5-3. The network is the least robust to changes the processes with the highest sensitivities and most robust against changes in processes with the lowest sensitivities. Figure 5-5 classifies processes as either having a high or low impact on each variable based on whether the corresponding relative sensitivity values were twice as high or half as the average over all processes, respectively. Along with Table 5-3, it provides a more global depiction of the system's sensitivity to perturbations.

5.5.2 Wnt3a Elicits Increase in ABC and Decrease in AJ Stability

Fold-change in ABC and AJs were measured in TCLs, and quantifying the difference of expression in the different conditions through immunoblot (IB) or immunoprecipitation (IP). Because α-catenin is recruited to mature junctional complexes, the stability of AJs was measured through the ratio of α-catenin to E-cadherin in E-cadherin immunoprecipitates. This provides the response of the system to activation with Wnt3a at the *reference condition* (*i.e.* without perturbation of individual processes in the system).

The abundance of ABC increased on average by 3.08 fold in the *activated state* compared to the *constitutive state*. An increase in the concentration of ABC was expected based both on the simulation predictions (Figure 5-3) and reports in the literature (154). Meanwhile, the ratio of α-catenin to E-cadherin dropped to 0.61 in the *activated state* compared to the *constitutive state.* This means that treatment with Wnt3a caused intercellular adhesion to drop as expected from the numerical simulations (Figure 5-3). Blots and quantification can be seen in Figure 5-6.

5.5.3 ICG-001 Counteracts Effect of Wnt3a on RCN

To obtain the fold-change values in a *dysregulated condition* (*i.e.* with perturbed reaction rates) and test the effectiveness of the RCN model, *constitutive* and *activated states* were treated additionally with the small molecule inhibitor ICG-001. Addition of ICG-001 can be simulated as an increase in the equilibrium constant that describes the binding equilibrium between β-catenin and TCF (reaction 11, Figure 5-2).

In the presence of ICG-001, the abundance of ABC dropped to 0.22 fold in the *activated state* compared to the *constitutive state*. This is consistent with the simulations in that there is no longer an increase in ABC abundance with Wnt3a; however, simulations predicted no change in ABC abundance instead of the observed drop (Figure 5-3). Experimental results matched simulated predictions for abundance of α-catenin in E-cadherin immunoprecipitates, which only dropped to 0.83 of the constitutive abundance compared to 0.6 in the *reference condition*. This indicates that in the with ICG-001 treatment, Wnt3a reduces the change in stability of AJs with Wnt3a. This matches theoretical predictions (Figure 5-3). Representative blots and average

quantification for multiple experiments are shown in Figure 5-6.

5.5.4 β-catenin Confirmed as Key Node in RCN

Table 5-3 indicates that β-catenin synthesis, TCF expression, and affinity of β-catenin to the BDC are the main regulatory processes in the RCN. This confirms the importance of β-catenin as a key node in the network. As such, it makes sense for β-catenin to be one of the few molecules whose concentration is robust to changes in kinetics of these three processes (Figure 5-3); given that that these processes directly involve β-catenin and they regulate most of the RCN dynamics, then the β-catenin with Wnt3a should be regulated independently. Instead β-catenin fold-change is most sensitive the processes directly related to N-glycosylation, specifically the degradation rates of *DPAGT1* mRNA and GPT.

While our model differs from others accounting for co-synthesis of β-catenin with E-cadherin (reaction 20, Figure 5-2) and two separate fates for β-catenin once dissociated from AJs (reactions 25 and 26), this additional pool of β-catenin does not impact cellular response to Wnt3a activation. LSA suggests that degradation via the BDC is the only process by which β-catenin can be effectively degraded. Although still debated, many models have used β-catenin released from AJs as a determining factor in determining cellular response and regulating cell-cell adhesion (13, 159).

Simultaneously, our studies suggest that processes that affect the system the least include those describing non Axin-dependent β-catenin degradation (reaction 10, Figure 5-2), APC availability and BDC assembly dynamics (reactions 3 and 8), and E-cadherin transport to the membrane (reactions 20-23, 25-26). Looking at the process ranking

(Table 5-3), Wnt/β-catenin signaling is the most influential pathway in the regulatory network, followed by N-glycosylation; E-cadherin-mediated adhesion, meanwhile, is the least influential.

5.5.5 Adhesion is Regulated by Multiple Pathways Alike

Analysis reveals that regulation of adhesion through Wnt/β-catenin signaling occurs via complex interactions of multiple pathways rather than through direct control of E-cadherin synthesis. In the case of AJs, analysis shows that AJs are very sensitive to changes in Wnt/β-catenin signaling. Regarding N-glycosylation, AJs are sensitive to the efficiency with which *DPAGT1* is transcribed (reaction 12, Figure 5-2) and the rate of E-cadherin N-glycosylation (*i.e.* parameter $V_{max}t/G_{max}$, see section 5.7.1). This is in accordance with the overexpression of *DPAGT1* and increased N-glycosylation observed together with epithelial discohesion in cell samples collected from oral tumors in oral squamous cell carcinoma (9, 16).

Adhesivity (σ) appears to be slightly less sensitive than AJs to dysregulation of the RCN. Figure 5-3 shows how adhesivity responds in a similar but more attenuated manner to changes in β-catenin/TCF binding. Adhesivity appears to be only highly sensitive to changes in TCF total abundance, the efficiency with which *DPAGT1* is transcribed, and the rate of N-glycosylation, but not to changes in Wnt/β-catenin signaling. Overall, the sensitivity values for AJ were higher than those for adhesivity, meaning N-glycosylation regulates adhesion through the number of cellular junctions rather than stability of junctions.

Figure 5-3 also indicates that AJs and adhesivity reach equilibrium at different

times after activation with Wnt3a; AJ reaches a steady-state faster than adhesivity in both the *reference* and *dysregulated conditions*. This means that cells regulate the number of contacts much faster, and it is later that the stability of these contacts is determined with a period of hours in between the two events. The slower regulation of adhesivity compared to AJ coincides with in vitro observations where cells will become less N-glycosylated with time as density of cultures increases and boundaries exist for longer (153, 167). Despite the similarities in the curves for AJs and adhesivity in Figure 5-3, the minimum value in fold-change does not correspond to the same parameter value (*i.e.* extent of dysregulation). By shifting the equilibrium between β-catenin and TCF towards unbinding, the drop in AJs is sharper and occurs first; however, if further dysregulation occurs, recovery of junctions begins with decreased N-glycosylation before restoring AJs. This suggests that in dysregulated epithelium, regulation of E-cadherin N-glycosylation can act against discohesion.

5.5.6 RCN is Insensitive to E-cadherin Recycling

Despite considering the additional process β-catenin co-synthesis with E-cadherin (compared to other models), AJs and adhesivity were independent of most processes involving E-cadherin. In general, all molecular concentrations were robust to changes in E-cadherin recycling (reactions 21-25, Figure 5-2) with the exception of E-cadherin/β-catenin complexes in the membrane and ERC. These two E-cadherin pools were sensitive to changes in the rate at which membrane E-cadherin is internalized (reaction 22). Sensitivity to this process is still significantly lower than to those corresponding to Wnt/β-catenin signaling and protein N-glycosylation (Figure 5-4).

Insight into why this may be the case physiologically could come from the difference in response by AJs and adhesivity with dysregulation (Figure 5-3). The drastic fold-change in AJs and adhesivity with Wnt3a is enough to regulated adhesion as it is independent of the concentration of E-cadherin in the membrane remaining constant. We see evidence of this when no difference is seen in E-cadherin localization within the cells in the scratch-wound assay despite the observed significant differences in speed (not shown).

5.5.7 Model Predicts Response to RCN Dysregulation

Validation of a mathematical model of a cellular system is challenging because measurements of cellular concentrations in time and space are difficult. The use of the small molecule inhibitor ICG-001 provides a way to perturb the system in a controlled way by targeting a single process; we recreated the simulated condition in which the equilibrium binding between β-catenin and TCF was shifted away from formation of the protein complex.

Figure 5-3 shows how the equilibrium binding between TCF and β-catenin plays a role in determining fold-change of GPT, AJs, and E-cadherin adhesivity (σ). A perturbation of the equilibrium in any direction implies an immediate change in response to Wnt/β-catenin activation. There is a significant fold-change in both AJ and adhesivity only for perturbations around the reference value; for extreme values the fold-change are 1. This suggests that AJ and adhesivity are responsive to β-catenin translocation to the nucleus only within a certain range. In contrast, fold-change in ABC is sensitive to the shift in the direction of unbinding of β-catenin and TCF but insensitive when equilibrium

shifts towards formation of a stable complex.

In general, the immunoblots reveal that experimental findings support the model's predictions, other than the drop in ABC when treating with Wnt3a in the *dysregulated condition*. Relative to the *constitutive state* (no additional Wnt3a) in *reference condition*, addition of ICG-001 elicits no significant change in ABC abundance. The increase in ABC abundance with addition of ICG-001 in the *constitutive state* (Figure 5-6) indicates that another pathway may be playing a role in regulation of β-catenin. With the addition of ICG-001, CBP is inhibited from interacting with β-catenin; however, β-catenin can still interact with the CBP homolog p300 causing transcription of different Wnt target genes. A switch to use p300 is associated with changes in cell potency and initiation of differentiation (168). Another factor making assessment of effectiveness of the prediction difficult is the biphasic response to changes in the parameter value of the fold-change curves for GPT, AJ, and adhesivity (Figure 5-3). Nonetheless, treatment with ICG-001 is expected to only shift parameter value slightly, as any drastic change would probably result in cell death. It is likely, that in reality the *reference condition* would be better described by scaling the parameter by a factor of approximately 2 in Figure 5-3. If treatment with ICG-001 is simulated as multiplying the parameter by a factor ~2, then IB results match the decrease in fold-change in ABC and increase in fold-change in AJs with ICG-001 treatment.

5.5.8 Wnt3a Inhibition Hinders Collective Migration

The effects of dysregulation of the RCN were noticeable at the population level; measurements of cellular speed in epithelial cell layers changed significantly with ICG-

001 treatment. A scratch-wound assay provided a measure of collective speed, and PIV was used to look at the optic flow within the cell sheet.

In the *reference condition*, both speed of the leading edge and optic flow dropped upon activation with Wnt3a. The drop was more dramatic within the cell sheet than at the wound edge. Speed dropped by 33% within the cell sheet, while in the *dysregulated condition* it was only 14%. Table 5-4 displays the speed of the leading edge and the average optic flow speed for constitutive and activated states both in the presence (*i.e. dysregulated condition*) and absence (*i.e. reference condition*) of ICG-001. Figure 5-7 shows the corresponding plot of magnitude of optic flow.

5.5.9 AJ Stability and Cell Speed Respond Analogously to ICG-001

RCN regulation of cellular speed may be indirect through the effect on adhesion, but a significant change in speed with Wnt3a and ICG-001 treatment demonstrates the importance of the RCN to tissue architecture. Analysis of cellular speed through PIV in the scratch-wound assay reveals two things: First, the change in speed due to ICG-001 treatment matches the changes in AJ stability. Second, the speed of the leading edge does not match speed of cells within the sheet.

Comparing the graphic in Figure 5-6b with Figure 5-7, the analogous trend in AJ stability and cellular speed within the sheet is evident. This indicates that less attached cells move slower within the cell sheet. In the presence of the same substrate, it is possible that highly migratory cells need adhesion to guide each other and reach higher speeds. This is in accordance with findings in MCF10A epithelial sheets showing that cell-cell adhesion is necessary to relay information about substrate stiffness by cells on

the edge to cells further back and promote migration (169). The drop in speed with ICG-001 in the conditions with no Wnt3a, indicate that adhesion is reduced by ICG-001 alone. This supports the idea that adhesion is necessary for faster migration within the sheet; by preventing β-catenin/TCF binding, ICG-001 could promote *DPAGT1* transcription and AJs with more N-glycosylated E-cadherin would be less adhesive and thus slower.

Table 5-4 reports how in the *reference condition*, Wnt3a treatment caused only a slight change in speed of the leading edge (9.1%), but a significant change speed within the sheet (33.2%). In the *dysregulated case*, there is no evident change in speed in either the wound edge or behind it. A possible explanation for this discrepancy is that despite the drop in general speed caused by the drop in adhesion, the cells can still move coordinately to keep the leading edge speed high. This hypothesis was tested by measuring the correlation length in the monolayer; however, no significant difference was observed (not shown). This drop in speed can be associated with the potential differentiation triggered by exposure to ICG-001 and the switch to use p300 in β-catenin mediated transcription. This decrease in potency is associated with changes in motility, proliferation, and survival which would all affect speed.

5.6 Discussion

This chapter examines the cross-talk among Wnt/β-catenin signaling, protein N-glycosylation, and E-cadherin mediated adhesion by expanding previous models of Wnt/β-catenin signaling. In addition to identifying key nodes in the RCN, the model provides potential answers to questions that remain in the field. Many models have used β-catenin released from AJs as a determining factor in determining cellular response and

regulating cell-cell adhesion (13, 159), despite no direct observation. We show that given our understanding of the transport of E-cadherin within the cell and E-cadherin/β-catenin association, dissociation of β-catenin from E-cadherin upon AJ disassembly will not impact Wnt/β-catenin signaling. Similarly we explore the relative importance of two molecules that make part of the BDC, axin and APC. Experimental studies have suggested that APC dysregulation is important in epithelial discohesion, particularly in cancer (16, 170–175). Our results raise the question if this is a response to other changes that are directly responsible for disruption of cell-cell contacts. Meanwhile, we show that Axin availability is crucial in determining the regulation of AJs, DPAGT1 transcription, and expression of the enzyme GPT.

Because this network playing a central role in development, we put the results of our theoretical analysis in the context of cell collectives and think about its implications to cell-cell adhesion and cell migration. The model matches the drop in adhesion expected of Wnt/β-catenin activation, but also predicts how this drop changes with specific changes in the network. Going beyond describing the change in AJ formation, the adhesivity factor is defined to account for the effect of N-glycosylation of E-cadherin on adhesion at the molecular level. To date this has been studied experimentally in single molecule force spectroscopy studies that isolate E-cadherin molecules from the rest of the junctional complex (62).

In our protein quantification experiments, despite being performed days after perturbation of the system, it cannot be assumed that cells were at equilibrium. Many processes remain unaccounted for when looking at pathways within a single cell

compared to a cell population. Further, the abundance of different components in the network varies among cells. For this reason, protein quantification and sheet migration experiments were not expected to reveal the dynamics of the RCN, but together provide a window into the cross-reactivity of the component pathways. The observed change in speed, though, corroborate that a change in a key node in the RCN will lead to significant changes in cell-cell interactions.

The concerted effect of Wnt/β-catenin signaling, protein N-glycosylation, and E-cadherin-mediated adhesion on the is complex, but with a theoretical representation in place, we can predict changes in abundance of the key regulatory molecules that affect how a cell behaves in physiological and pathological conditions. With this description of such a regulatory network in place, we can easily simulate the response of healthy and diseased cells to specific treatments. It can be used a framework to choose therapeutics based on predicted effectiveness of promotion or inhibition of specific processes that may be used to prevent problems during development or prevent invasion of the neighboring stroma in carcinomas. This model can be integrated into agent-based models to account for the complex dynamics that arise from the intersection of three essential pathways during collective processes such as morphogenesis.

5.7 Mathematical Description and Simplification of RCN

5.7.1 Network Description as Set of ODEs

In the set of ODEs, binding and dissociation processes are described by the rate equations: $k_i \cdot X \cdot Y - k_{-i} \cdot (X/Y)$ where X and Y denote the free concentrations of the binding

partners, *(X/Y)* the concentration of the complex, and k_i and k_{-i} the association and dissociation rates respectively of the complexes formed by the proteins (*i* denotes the reaction number as specified in Figure 5-2). Syntheses of proteins are described by constant rates (v_i). Phosphorylation and dephosphorylation processes are described by linear rate equations $(k_i \cdot X)$. All rate constants along with their sources are included in Table 5-2.

The following are the variables in the system:

X_1 - Wnt3a

X_2 - (Wnt3a/LRP^)

X_3 - (Wnt3a/LRP^/APC/Axin/GSK3)

X_4 - (APC/Axin/GSK3)

X_5 - (APC*/Axin*/GSK3)

X_6 - (Axin/GSK3)

X_7 - APC

X_8 - (β-cat/APC)

X_9 - (β-cat/APC*/Axin*/GSK3)

X_{10} - β-cat

X_{11} - TCF

X_{12} - (β-cat/TCF)

X_{13} – *DPAGT1* mRNA

X_{14} – GPT

X_{15} - LRP

X_{16} - LRP^

X_{17} – (E-cad/ β-cat)$_{ER}$

X_{18} – (E-cad/ β-cat)$_{M}$

X_{19} – (E-cad/ β-cat) $_{ERC}$

X_{20} – AJ

σ_{ER} - Adhesivity of E-cadherin in ER

σ_{M} - Adhesivity of E-cadherin in M

σ_{ERC} - Adhesivity of E-cadherin in ERC

σ_{AJ} - Adhesivity of E-cadherin in AJ

Transcriptional activation by a single activator (i.e. (β-cat/TCF) or X_{12}) is modeled as a Hill-type activation. This has been demonstrated to be appropriate for this system, recreating published experimental data (155, 176). This is shown in Equation 5-2:

$$\varphi(X_{12}, K_{TmRNA}, \nu) = \frac{X_{12}^{\nu}}{(K_{TmRNA}^{\nu} + X_{12}^{\nu})} \quad (5\text{-}2)$$

where K_{TmRNA} is the activator concentration at which transcription proceeds at half of its maximal rate and ν describes the degree of nonlinearity in the activation (cooperativity or Hill coefficient). Subsequent translation of the resulting *DPAGT1* mRNA is modeled with enzyme synthesis being determined by the amount of mRNA (X_{13}) and a maximum rate of translation (P_{max}). Equation 5-3 describes their relation:

$$\chi(X_{13}, P_{max}) = P_{max} X_{13} \quad (5\text{-}3)$$

For the N-glycosylation of LRP (X_{15}), it is assumed that binding of GPT (X_{14}) and LRP is non-reversible and conversion into N-glycosylated LRP or LRP^ (X_{16}) occurs much faster than the binding between substrate and enzyme. This results in Equation 5-4:

$$\psi(X_{14}, X_{15}, k_{17}) = k_{17} X_{14} X_{15} \tag{5-4}$$

Enzymatic activity of GPT on E-cadherin was modeled differently, because the extent of N-glycosylation of E-cadherin modulates homotypic binding of E-cadherin rather than determine whether it will be transported to the membrane or not (as with LRP5/6). To model this effect an adhesivity factor was introduced (σ): This value is normalized to the maximum concentration of N-glycosylated E-cadherin that can be synthesized in a single step (heuristically determined); when σ = 0, the E-cadherin is completely non-adhesive, and when σ = 1, it is the most adhesive. This time varying factor is calculated for each of the four pools included in the reaction scheme: endoplasmic reticulum (ER), membrane (M), endocytic recycling compartment (ERC), and adherens junctions (AJ). The change over time in E-cadherin adhesivity for each pool is calculated based on the fraction of incoming E-cadherin to the new total concentration of E-cadherin in the pool (f_{gain}) and the adhesivity of the incoming and receiving E-cadherin, σ_{source} and $\sigma_{destination}$ respectively. This change is described by Equation 5-5:

$$\frac{d\sigma_{destination}}{dt} = (f_{gain})(\sigma_{source} - \sigma_{destination}) \tag{5-5}$$

Because E-cadherin in the ER pool is synthesized and not transported from a source pool, σ_{ER} is dependent on the concentration of GPT at the time of synthesis. The rate at which E-cadherin in the ER is N-glycosylated is calculated assuming Michaelis-Menten kinetics of GPT with no cooperativity.

Starting with the Michaelis-Menten equation (Equation 5-6):

$$\nu = \frac{V_{max}[S]}{K_M + [S]} \tag{5-6}$$

Because the substrate to GPT is a LLO and cells are not being modeled under a shortage of carbohydrates, it is assumed that it is the availability of enzyme and not the substrate what determines the kinetics of the reaction. In this case, to adapt Michaelis-Menten kinetics to this system, two assumptions are made: First, a quasi-steady state of the substrate (*i.e.* the concentration of the substrate/product changes much more slowly than that of the enzyme). Second, the substrate (*i.e.* N-glycans) is unlimited.

Both sides of Equation 5-6 are multiplied by time (t) to get the amount of product on the LHS and divide by G_{max} (the maximum possible concentration of N-glycosylated E-cadherin in the ER) to normalize the amount of product. Because E-cadherin is more adhesive when extent of N-glycosylation is low, and *vice versa*, the ratio of product is subtracted from 1 to define σ at the time of synthesis (Equation 5-7):

$$\sigma_{synthesis} = 1 - \frac{vt}{G_{max}} = 1 - \frac{t}{G_{max}} \frac{V_{max}[GPT]}{K_M + [GPT]} \tag{5-7}$$

Thus the change in σ_{ER} over time is given by Equation 5-8:

$$\frac{d\sigma_{ER}}{dt} = \left(f_{gain}\right)[(1 - \frac{V_{max}t}{G_{max}}\frac{X_{14}}{K_M + X_{14}}) - \sigma_{ER}] \tag{5-8}$$

V_{max} represents the maximum rate of N-glycosylation of E-cadherin by GPT in the ER. K_M represents the GPT concentration at which enzymatic activity is half-maximal.

To describe the dependence of the rate of AJ formation (k_{24}) on σ_M, a simple linear relation was chosen due to the difficulty in defining this relation experimentally as cellular environment is believed to be highly variable and influential to this relation. Similarly, an inverse linear relation was chosen for the dependence of the rate of AJ dissociation (k_{-24}) on σ_{AJ}. Equations 5-9 and 5-10 describe these relations:

$$k_{24}(\sigma_M) = k_{aj}\,\sigma_M \tag{5-9}$$

$$k_{-24}\left(\sigma_{AJ}\right) = -k_{daj}\,\sigma_{AJ} + k_{Mdaj} \tag{5-10}$$

k_{aj} represents the fastest possible rate of AJ formation (when σ_M = 1), k_{daj} is the drop in rate of AJ disruption when going from minimal to maximal E-cadherin adhesivity, and k_{Mdaj} is the fastest possible rate of AJ disruption (set equal to k_{daj} in model for reported results).

The complete system of ODEs is presented below in Equations 5-11 through 5-34:

$$\frac{dX_1}{dt} = k_{-1}X_2 - k_1X_1X_{16} \quad (5\text{-}11)$$

$$\frac{dX_2}{dt} = k_1X_1X_{16} - k_{-1}X_2 + k_{-2}X_3 - k_2X_2X_4 \quad (5\text{-}12)$$

$$\frac{dX_3}{dt} = k_2X_2X_4 - k_{-2}X_3 \quad (5\text{-}13)$$

$$\frac{dX_4}{dt} = k_{-2}X_3 - k_2X_2X_4 - k_4X_4 + k_5X_5 + k_3X_6X_7 - k_{-3}X_4 \quad (5\text{-}14)$$

$$\frac{dX_5}{dt} = k_4X_4 - k_5X_5 + k_7X_9 + k_{-6}X_9 - k_6X_5X_{10} \quad (5\text{-}15)$$

$$\frac{dX_6}{dt} = k_{-3}X_4 - k_3X_6X_7 \quad (5\text{-}16)$$

$$\frac{dX_7}{dt} = k_{-3}X_4 - k_3X_6X_7 + k_{-8}X_8 - k_8X_7X_{10} \quad (5\text{-}17)$$

$$\frac{dX_8}{dt} = k_8X_7X_{10} - k_{-8}X_8 \quad (5\text{-}18)$$

$$\frac{dX_9}{dt} = k_6X_5X_{10} - k_{-6}X_9 - k_7X_9 \quad (5\text{-}19)$$

$$\frac{dX_{10}}{dt} = \nu_9 + k_{-6}X_9 - k_6X_5X_{10} + k_{-8}X_8 - k_8X_7X_{10} + k_{-11}X_{12} - k_{11}X_{10}X_{11} + k_{25}X_{19} - k_{10} \quad (5\text{-}20)$$

$$\frac{dX_{11}}{dt} = k_{-11}X_{12} - k_{11}X_{10}X_{11} \quad (5\text{-}21)$$

$$\frac{dX_{12}}{dt} = k_{11}X_{10}X_{11} - k_{-11}X_{12} \quad (5\text{-}22)$$

$$\frac{dX_{13}}{dt} = T_{max}\left[\frac{X_{12}^{\nu}}{(K_{TmRNA}^{\nu} + X_{12}^{\nu})}\right] - k_{13}X_{13} \quad (5\text{-}23)$$

$$\frac{dX_{14}}{dt} = P_{max}X_{13} - k_{19}X_{14} \quad (5\text{-}24)$$

$$\frac{dX_{15}}{dt} = v_{15} - k_{17}X_{14}X_{15} - k_{16}X_{15} \quad (5\text{-}25)$$

$$\frac{dX_{16}}{dt} = k_{17}X_{14}X_{15} - k_{18}X_{16} + k_{-1}X_2 - k_1X_1X_{16} \quad (5\text{-}26)$$

$$\frac{dX_{17}}{dt} = v_{20} - k_{21}X_{17} \quad (5\text{-}27)$$

$$\frac{dX_{18}}{dt} = k_{21}X_{17} - k_{22}X_{18} + k_{23}X_{19} + k_{-24}(\sigma_{AJ})X_{20} - k_{24}(\sigma_M)X_{20} \quad (5\text{-}28)$$

$$\frac{dX_{19}}{dt} = k_{22}X_{18} - k_{23}X_{19} - k_{25}X_{19} - k_{26}X_{19} \quad (5\text{-}29)$$

$$\frac{dX_{20}}{dt} = k_{24}(\sigma_M)X_{18} - k_{-24}(\sigma_{AJ})X_{20} \quad (5\text{-}30)$$

$$\frac{d\sigma_{ER}}{dt} = \left(\frac{\nu_{20}}{X_{17}}\right)\left[\left(1 - \frac{V_{max}t}{G_{max}}\frac{X_{14}}{K_M + X_{14}}\right) - \sigma_{ER}\right] \quad (5\text{-}31)$$

$$\frac{d\sigma_M}{dt} = \left(\frac{k_{21}X_{17}}{X_{18}}\right)(\sigma_{ER} - \sigma_M) + \left(\frac{k_{23}X_{19}}{X_{18}}\right)(\sigma_{ERC} - \sigma_M) + \left(\frac{k_{-24}(\sigma_{AJ})X_{20}}{X_{18}}\right)(\sigma_{AJ} - \sigma_M) \quad (5\text{-}32)$$

$$\frac{d\sigma_{ERC}}{dt} = \left(\frac{k_{22}X_{18}}{X_{19}}\right)(\sigma_M - \sigma_{ERC}) \quad (5\text{-}33)$$

$$\frac{d\sigma_{AJ}}{dt} = \left(\frac{k_{24}(\sigma_M)X_{18}}{X_{20}}\right)(\sigma_M - \sigma_{AJ}) \quad (5\text{-}34)$$

5.7.2 From ODEs to DAEs

Two assumptions were used to simplify the system from a system of ODEs to a system of DAEs. First, a fast equilibrium approximation was used for reactions i = 1, 2, 6, 8. Their equilibrium constants can be described algebraically by Equation 5-35:

$$K_i = \frac{k_{-i}}{k_i} = \frac{X \cdot Y}{(X/Y)} \quad (5\text{-}35)$$

The resulting equations are shown as Equations 5-36 through 5-40:

$$X_2 = \frac{X_1 X_{16}}{K_1} \quad (5\text{-}36)$$

$$X_3 = \frac{X_2 X_4}{K_2} \quad (5\text{-}37)$$

$$X_9 = \frac{X_5\, X_{10}}{K_6} \tag{5-38}$$

$$X_8 = \frac{X_7\, X_{10}}{K_8} \tag{5-39}$$

$$X_{12} = \frac{X_{10}\, X_{11}}{K_{11}} \tag{5-40}$$

The individual forward and backward rates, k_i and k_{-i}, were removed from the ODEs by linearly combining equations with these rate constants, reducing the number of parameters needed to describe these reactions from two to one. More specifically, the following linear combinations of ODEs were performed:

$$-\frac{dX_1}{dt} + \frac{dX_3}{dt} + \frac{dX_4}{dt} + \frac{dX_{16}}{dt} = \cdots \tag{5-41}$$

$$-\frac{dX_5}{dt} + \frac{dX_8}{dt} + \frac{dX_{10}}{dt} + \frac{dX_{12}}{dt} = \cdots \tag{5-42}$$

$$\frac{dX_5}{dt} + \frac{dX_9}{dt} = \cdots \tag{5-43}$$

$$\frac{dX_7}{dt} + \frac{dX_8}{dt} = \cdots \tag{5-44}$$

The second assumption was the conservation of a set of molecules assumed to be expressed constitutively in cells. These molecules were Wnt3a, APC, TCF, and (Axin/GSK3). Their total concentration was represented by the parameters WNT^0, APC^0, TCF^0, and $(Axin/GSK3)^0$, respectively. The resulting conservation equations are presented as Equations 5-45 through 5-48:

$$X_1 + X_2 + X_3 = WNT^0 \tag{5-45}$$

$$X_3 + X_4 + X_5 + X_7 + X_8 + X_9 = APC^0 \tag{5-46}$$

$$X_3 + X_4 + X_5 + X_6 + X_9 = (Axin/GSK3)^0 \tag{5-47}$$

$$X_{11} + X_{12} = TCF^0 \tag{5-48}$$

Given that $APC^0 >> (Axin/GSK3)^0$, Equation 5-46 was simplified to Equation 5-49:

$$X_7 + X_8 = APC^0 \tag{5-49}$$

5.7.3 Network Description as Set of DAEs

The system of DAEs can be classified into algebraic equations (Equations 5-50 through 5-58), differential equations (Equations 5-59 through 5-70), and implicit differential equations (Equations 5-71 through 5-73):

$$X_1 = \frac{WNT^0 K_1 K_2}{K_1 K_2 + K_2 X_{16} + X_4 X_{16}} \quad (5\text{-}50)$$

$$X_2 = \frac{WNT^0 K_2 X_{16}}{K_1 K_2 + K_2 X_{16} + X_4 X_{16}} \quad (5\text{-}51)$$

$$X_3 = \frac{WNT^0 X_4 X_{16}}{K_1 K_2 + K_2 X_{16} + X_4 X_{16}} \quad (5\text{-}52)$$

$$X_6 = (Axin/GSK3)^0 - \left(1 + \frac{WNT^0 X_{16}}{K_1 K_2 + (K_2 + X_4) X_{16}}\right) X_4 - (1 + \frac{X_{10}}{K_6}) X_5 \quad (5\text{-}53)$$

$$X_7 = \frac{APC^0}{1 + \frac{X_{10}}{K_8}} \quad (5\text{-}54)$$

$$X_8 = \frac{X_7 X_{10}}{K_8} \quad (5\text{-}55)$$

$$X_9 = \frac{X_5 X_{10}}{K_6} \quad (5\text{-}56)$$

$$X_{11} = \frac{TCF^0 K_{11}}{K_{11} + X_{10}} \quad (5\text{-}57)$$

$$X_{12} = \frac{TCF^0 X_{10}}{K_{11} + X_{10}} \quad (5\text{-}58)$$

$$\frac{dX_6}{dt} = k_{-3}X_4 \; - \; k_3X_6X_7 \tag{5-59}$$

$$\frac{dX_{13}}{dt} = \; T_{max} \left[\frac{X_{12}^{\nu}}{(K_{TmRNA}^{\nu} + X_{12}^{\nu})} \right] \; - \; k_{13} \, X_{13} \tag{5-60}$$

$$\frac{dX_{14}}{dt} = \; P_{max} \, X_{13} \; - \; k_{19} \, X_{14} \tag{5-61}$$

$$\frac{dX_{15}}{dt} = \; v_{15} \; - \; k_{17} \, X_{14} \, X_{15} - k_{16}X_{15} \tag{5-62}$$

$$\frac{dX_{17}}{dt} = \; v_{20} \; - \; k_{21}X_{17} \tag{5-63}$$

$$\frac{dX_{18}}{dt} = \; k_{21} \, X_{17} - \; k_{22}X_{18} + \; k_{23}X_{19} + \; k_{-24}(\sigma_{AJ}) \, X_{20} - \; k_{24}(\sigma_M) \, X_{18} \tag{5-64}$$

$$\frac{dX_{19}}{dt} = \; k_{22}X_{18} - \; k_{23}X_{19} - \; k_{25}X_{19} - \; k_{26}X_{19} \tag{5-65}$$

$$\frac{dX_{20}}{dt} = \; k_{24}(\sigma_M)X_{18} - k_{-24}(\sigma_{AJ}) \, X_{20} \tag{5-66}$$

$$\frac{d\sigma_{ER}}{dt} = \left(\frac{v_{20}}{X_{17}}\right) [(1 - \frac{V_{max}t}{G_{max}} \frac{X_{14}}{K_M + X_{14}}) - \sigma_{ER}] \tag{5-67}$$

$$\frac{d\sigma_M}{dt} = \left(\frac{k_{21}X_{17}}{X_{18}}\right)(\sigma_{ER} - \sigma_M) + \left(\frac{k_{23}X_{19}}{X_{18}}\right)(\sigma_{ERC} - \sigma_M) + \left(\frac{k_{-24}(\sigma_{AJ})X_{20}}{X_{18}}\right)(\sigma_{AJ} - \sigma_M) \quad (5\text{-}68)$$

$$\frac{d\sigma_{ERC}}{dt} = \left(\frac{k_{22}X_{18}}{X_{19}}\right)(\sigma_M - \sigma_{ERC}) \quad (5\text{-}69)$$

$$\frac{d\sigma_{AJ}}{dt} = \left(\frac{k_{24}(\sigma_M)X_{18}}{X_{20}}\right)(\sigma_M - \sigma_{AJ}) \quad (5\text{-}70)$$

$$-\frac{dX_5}{dt} + \frac{dX_{10}}{dt}\left[\frac{\delta X_8}{\delta X_{10}} + \frac{\delta X_{12}}{\delta X_{10}} + 1\right] = -k_4X_4 + k_5X_5 - k_7X_9 + \nu_9 + k_{25}X_{19} - k_{10} \quad (5\text{-}71)$$

$$\frac{dX_5}{dt}\left[\frac{\delta X_9}{\delta X_5} + 1\right] + \frac{dX_{10}}{dt}\left[\frac{\delta X_9}{\delta X_{10}}\right] = k_4X_4 - k_5X_5 \quad (5\text{-}72)$$

$$\frac{dX_4}{dt}\left[-\frac{\delta X_1}{\delta X_4} + \frac{\delta X_3}{\delta X_4} + 1\right] + \frac{dX_{16}}{dt}\left[-\frac{\delta X_1}{\delta X_{16}} + \frac{\delta X_3}{\delta X_{16}} + 1\right] = k_{17}X_{14}X_{15} - k_{18}X_{16} - k_4X_4 + k_5X_5 + k_3X_6X_7 - k_{-3}X_4 \quad (5\text{-}73)$$

5.7.4 Parameter Value Selection and Estimation

The values for the multiple parameters in the DAEs were chosen based on experimental findings in the literature or estimation in related models. Additional parameter values were estimated by setting constraints between parameters or between steady-state variable values and parameters (based on observations in the literature). Parameters for which no measurement or approximation was found, remained "free" and

were estimated by varying them over a wide range and choosing the value that would fit experimental findings.

This was done in steps: First, focusing on parameters describing Wnt/β-catenin signaling and β-catenin regulation. Next, focusing on parameters describing E-cadherin recycling. Lastly, parameters describing *DPAGT1* expression its effect on ABC concentration and AJ formation were approximated.

Regarding parameters describing Wnt/β-catenin signaling and β-catenin regulation: Parameter values describing the dynamics of reactions 3-11 (Figure 5-2) were either taken from the Lee and minimal models or taken to maintain steady-state values of molecules considered in these studies (154, 155). Table 5-1 shows how steady-state concentration of the all variables for Wnt "ON" and Wnt "OFF" cases compare in our study to the Lee model.

It can be observed in Table 5-2 that of all parameters taken from the Lee model, only K_6 and v_9 were changed. K_6 was reduced from 120 to 100 nM, which is still the same order of magnitude and had been estimated rather than measured by Lee *et al.* It was changed such that the total amount of β-catenin when there was no Wnt3a present would be 35 nM, which is measured and conserved in the RCN model.

v_9 was changed because the RCN model has two sources of β-catenin: reactions 9 and 20 (Figure 5-2). There is an ongoing debate as to whether once dissociated from E-cadherin, β-catenin can then feed into Wnt/β-catenin signaling (159). However, as long as $v_9 >> v_{20}$, the results of the Lee model were recreated by the RCN model. It was the ratio of the rates that was changed to obtain the expected concentrations of E-cadherin in the

system. The resulting values of v_9 and v_{20} were thus 0.6 nM/min and 0.6 × (0.006/100) nM/min, respectively, suggesting that as little as 0.006% of synthesized β-catenin with E-cadherin.

The value of K_1, which represents the affinity between Wnt3a and membrane receptor in general, was approximated from surface plasmon resonance studies on secreted Frizzled-related proteins (sFRPs) (177). Although in the RCN model Wnt3a binds to LRP5/6, this is meant to represent the Frizzled LRP5/6 co-receptor. Additionally, the paper looks at affinity of Wnt3a with secreted FRPs, not membrane bound Frizzled receptors. However, this was the only study found looking at affinity of Wnt3a with a receptor involved in Wnt/β-catenin signaling. The study revealed that the equilibrium constant for binding of these two molecules ranges from 4.1-11.2 nM. The value of 6 nM was chosen for the RCN model as it recreated the results of the Lee model.

Regarding parameters describing E-cadherin recycling: The E-cadherin recycling pathway in the RCN network is described by reaction 20-26. First, the following rates and concentration were taken directly from experimental studies:

$$k_{21} = \frac{1}{60} \tag{5-74}$$

$$k_{22} = 0.00231 min^{-1} \tag{5-75}$$

$$k_{26} = \frac{0.6}{225} \tag{5-76}$$

$$X_{18ss} = 0.0695\ nM \tag{5-77}$$

Equation 5-74 is based on the observation by Shore *et al.* that newly synthesized E-cadherin was maximally detected at the cell surface after a chase period of approximately 60 min (161). The value of k_{22} was preliminarily calculated from the observations by Chen *et al.* that the half-life of E-cadherin from membrane to lysosome is of < 5h (158). Equation 5-76 is based on the observation by Chen *et al.* that 60% of E-cadherin is degraded in 225 min via lysosome from the ERC (158). The steady-state concentration of E-cadherin at the membrane (X_{18}) was approximated from findings by McCrea *et al.* when identifying and isolating β-catenin in MDCK cells confluent monolayers (178).

Next, two constraints were considered based on observations reported in the literature:

$$0.47 = \frac{X_{18ss}}{X_{17ss} + X_{18ss} + X_{19ss}} \tag{5-78}$$

$$k_{23} + k_{25} + k_{26} = \frac{1}{15} \tag{5-79}$$

Equation 5-78 is based on the observation by Le *et al.* that in confluent MDCK cells approximately 47% of all E-cadherin in the cell was biotinylated on the cell surface (55). Meanwhile, Equation 5-79 is based on the observation that internalized E-cadherin accumulated at a cold temperature gradually disappeared from the internal pool over 15 min once the cell was placed in regular conditions (55).

Finally, the system of DAEs used to define the RCN (section 5.7.3) was considered. Equation 5-80 through 5-82 describe rate of change of E-cadherin at the ER (X_{17}) and the membrane (X_{18}) and adherens junctions (X_{20}) at steady-state:

$$\frac{dX_{17}}{dt} = 0 = v_{20} - k_{21}X_{17ss} \tag{5-80}$$

$$\frac{dX_{18}}{dt} = 0 = k_{21}\,X_{17ss} - k_{22}X_{18ss} + k_{23}X_{19ss} + k_{-24}(\sigma_{AJss})\,X_{20ss} - k_{24}(\sigma_{Mss})\,X_{18ss} \tag{5-81}$$

$$\frac{dX_{20}}{dt} = 0 = k_{24}(\sigma_M ss)X_{18ss} - k_{-24}(\sigma_{AJss})\,X_{20ss} \tag{5-82}$$

Since the rate of E-cadherin co-synthesis with β-catenin was already estimated, and Equation 5-82 can be substituted into Equation 5-81 to avoid considering reaction 24 and AJs, Equations 5-74 through 5-82 form a system of linear equations from which most missing parameters (*i.e.* k_{23}, k_{25}, k_{26}) can be approximated.

Some of the parameter values used at the *reference condition* (*i.e.* values leading to normal physiological concentrations), reported in Table 5-2, vary from those calculated above. This is because a series of perturbation studies were performed to ensure that not only the steady-state concentration of molecules involved in E-cadherin recycling would match experimental data, but also their change of concentration in time. For this purpose the kinetics of E-cadherin degradation in MDCK cells reported by Shore

et al. were recreated by varying the values of k_{22} and k_{25} without changing the order of magnitude (161).

The value of the parameters describing dynamics of reaction 24 (AJ formation by membrane E-cadherin and AJs dissociation) were then approximated to fit the dynamics of E-cadherin degradation. As presented in section 5.7.1, these rates were made dependent on an adhesiveness factor (σ), itself dependent on the extent of N-glycosylation. Equations 5-9 and 5-10 describe these relations.

Based on observations made by Kam *et al.* in which AJs began to disintegrate between 30-90 min after treatment of cells with LPA (159), Relation 5-83 is used for an initial estimation of k_{daj}:

$$\frac{1}{90} < k_{daj} < \frac{1}{30} \tag{5-83}$$

The value of k_{daj} was estimated to be 0.02 min^{-1} to fit dynamics of E-cadherin degradation. Observations made by Kam *et al.* also suggest that reconstruction of AJ after disruption with LPA treatment take twice as long as disruption, hence the value of and k_{aj} was set as half that of k_{daj}, as shown in Equation 5-84:

$$k_{aj} = \frac{k_{daj}}{2} \tag{5-84}$$

Regarding parameters describing *DPAGT1* expression its effect on ABC concentration and AJ formation: No kinetic studies were found on the N-glycosylation of

LRP5/6. Also, the RCN model is the first numerical model to look at the interaction between Wnt/β-catenin signaling and N-glycosylation. For this reason, no prior estimation exists of how *DPAGT1* expression affects N-glycosylation of LRP5/6 and E-cadherin, or how this modulates Wnt3a binding and AJ formation respectively. Parameters representing *DPAGT1* transcription and translation (*i.e.* T_{max}, K_{TmRNA}, P_{max}. k_{13}), LRP5/6 N-glycosylation (*i.e.* v_{15}, k_{16}-k_{19}), and GPT activity on E-cadherin (*i.e.* $V_{max}t/G_{max}$, K_M) had to be estimated.

Values were chosen heuristically to recreate measured fold-change in protein expression of selected molecules in MDCK cells upon causing known perturbations in *DPAGT1* expression (Table 5-5). In the case of *DPAGT1* downregulation, details on perturbation experiments can be found in the literature (70, 153). In the case of *DPAGT1* upregulation, resulting blots and quantification can be found in Figure 5-8.

By solving for the steady-state of σ_{ER}, it can be seen that the dependence of σ_{ERss} on the steady-state of GPT (X_{14ss}) is given by Equation 5-85:

$$\sigma_{ERss} = 1 - \frac{V_{max}t}{G_{max}} \frac{X_{14ss}}{K_M + X_{14ss}} \tag{5-85}$$

The values of $V_{max}t/G_{max}$ and K_M were chosen such that a 4.5 fold increase in X_{14ss} leads to a corresponding change in σ_{Mss} from 0.4424 → 0.09529 (at steady-state adhesivity (σ) has the same value for all E-cadherin pools), which recreates the 3 fold increase measured experimentally in the steady-state concentration of AJs (X_{20ss}).

5.8 Tables

Molecule/Variable	Wnt "OFF"		Wnt "ON"	
	Lee model	**RCN model**	**Lee model**	**RCN model**
Wnt3a	N/A	0	N/A	26.7565
(Wnt3a/LRP^)	N/A	0	N/A	1.2912
*(Wnt3a/LRP^/APC/*Axin/GSK3)*	N/A	0	N/A	0.01427
(APC/Axin/GSK3)	0.00483	0.005525	0.000729	0.0009212
(APC/Axin*/GSK3)*	0.00966	0.01105	0.00146	0.001842
(Axin/GSK3)	N/A	0.0005668	N/A	0.0001064
APC	98	97.4809	88.7	86.5796
(β-cat/APC)	2.05	2.519	11.3	13.4204
(β-cat/APC/Axin*/GSK3)*	0.00202	0.002855	0.00186	0.002855
β-cat	25.1	25.8418	153	155.006
TCF	8.17	8.0584	2.46	2.4323
(β-cat/TCF)	6.83	6.94152	12.5	12.5676
$\beta\text{-cat}^0$	35	35.3053	178	180.997
DPAGT1 mRNA	N/A	0.01265	N/A	0.03356
GPT	N/A	0.003422	N/A	0.00908
LRP	N/A	4.9158	N/A	4.7828
*LRP^*	N/A	0.1121	N/A	0.2895
$(\text{E-cad}^\wedge/\beta\text{-cat})_{ER}$	N/A	0.3742	N/A	0.3742
$(\text{E-cad}^\wedge/\beta\text{-cat})_{M}$	N/A	0.2597	N/A	0.2597
$(\text{E-cad}^\wedge/\beta\text{-cat})_{ERC}$	N/A	0.096	N/A	0.096
AJ	N/A	0.294	N/A	0.1034
$\sigma_{ER}, \sigma_{M}, \sigma_{ERC}, \sigma_{AJ}$	N/A	0.6936	N/A	0.4434

Table 5-1: Comparison of steady-state values from Lee model and RCN model

All values reported refer to concentrations and have units of nM, except for those for the adhesivity parameter (σ) for E-cadherin in endoplasmic reticulum (ER), membrane (M), and endocytic recycling compartment (ERC) pools. This parameter is dimensionless and has a value between (0,1). N/A is used for entries of molecules non-existent in the Lee model. For RCN model, Wnt "ON" condition corresponds to a total concentration of Wnta of WNT0 = 28.062 nM.

Parameter	Value	Units	Source	Cell type
WNT^0	0 (off), 28.062 (on)	nM	estimated	
APC^0	**100**	nM	Lee *et al.*	*Xenopus* oocyte
TCF^0	**15**	nM	Lee *et al.*	*Xenopus* oocyte
$(Axin/GSK3)^0$	**0.02**	nM	Lee *et al.*	*Xenopus* oocyte
$\beta\text{-}cat^0$	**35** (off)	nM	Lee *et al.*	*Xenopus* oocyte
K_1	**6**	nM	Wawrzak *et al.*	purified protein
K_2	1/12	nM	estimated	
k_4	0.26	min^{-1}	Lee *et al.* (estimated)	
k_5	0.13	min^{-1}	Lee *et al.* (estimated)	
k_3	0.091	$nM^{-1}\ min^{-1}$	Lee *et al.* (estimated)	
k_{-3}	0.91	min^{-1}	Lee *et al.* (estimated)	
K_6	100	nM	estimated	
k_7	210	min^{-1}	Lee *et al.* (estimated)	
K_8	**10 K_6**	nM	Salic *et al.*	*Xenopus* oocyte
v_9	0.6	nM min^{-1}	estimated	
k_{10}	**0.00026**	min^{-1}	Lee *et al.*	*Xenopus* oocyte
K_{11}	30	nM	Lee *et al.* (estimated)	
T_{max}	0.005946	nM min^{-1}	estimated	
K_{TmRNA}	10	nM	estimated	
v	**3**		Benary *et al.*	*Xenopus*, zebrafish
P_{max}	0.025	min^{-1}	estimated	
k_{13}	0.11781	min^{-1}	estimated	
v_{15}	0.1	$nM^{-1}\ min^{-1}$	estimated	
k_{16}	0.02	min^{-1}	estimated	
k_{17}	0.1	$nM^{-1}\ min^{-1}$	estimated	
k_{18}	0.015	min^{-1}	estimated	
k_{19}	0.0924	min^{-1}	estimated	
v_{20}	0.000036	nM min^{-1}	estimated	
k_{21}	1/60	min^{-1}	Chen *et al.*	MDCK
k_{22}	**0.0123**	min^{-1}	Kam *et al.*, Shore *et al.*	MDCK
k_{23}	0.0005	min^{-}	Chen *et al.*, Shore *et al.*, Le *et al.*	MDCK
k_{25}	0.02	min^{-1}	Chen *et al.*, Le *et al.*	MDCK
k_{26}	0.01	min^{-1}	estimated	
$V_{max}t/G_{max}$	1.1		estimated	
K_M	0.00887	nM	estimated	
k_{aj}	**0.01**	min^{-1}	Kam *et al.*	A431
k_{daj}	**0.02**	min^{-1}	Kam *et al.*	A431

Table 5-2: Parameter values and sources for RCN model

Parameters are grouped in the following categories from top to bottom: constitutive protein concentrations, Wnt3a binding, active β-catenin regulation, *DPAGT1* expression, N-glycosylation, E-cadherin recycling, and AJ formation/dissociation. Values in bold are those measured experimentally. Those with a reference for source but not in bold were estimated based on an experimental relation contained thereof. Those with corresponding source "estimated" and a reference were estimated for a model contained thereof. Those with corresponding source "estimated" and no reference were estimated in this model: Details about this estimation process can be found in section 5.7.4.

Rank	Reaction number	Parameter	*Avg. sensitivity*	Rank	Reaction number	Parameter	*Avg. sensitivity*
1)	9	ν_9	0.6	*17)*	4	k_4	0.26
2)	0 (b)	TCF^0	0.59	*18)*	18	k_{18}	0.26
3)	6	K_6	0.53	*19)*	16	k_{16}	0.26
4)	12 (b)	K_{TmRNA}	0.45	*20)*	20 (b)	$V_{max}\ t/G_{max}$	0.14
5)	0 (c)	$(Axin/GSK3)^0$	0.43	*21)*	20 (c)	K_M	0.06
6)	7	k_7	0.43	*22)*	3 (a)	k_3	0.03
7)	12 (a)	T_{max}	0.42	*23)*	0 (a)	APC^0	0.03
8)	14	P_{max}	0.42	*24)*	8	K_8	0.02
9)	15	ν_{15}	0.37	*25)*	3 (b)	k_{-3}	0.02
10)	17	k_{17}	0.36	*26)*	20 (a)	ν_{20}	0.0017
11)	5	k_5	0.35	*27)*	22	k_{22}	0.0016
12)	11	K_{11}	0.31	*28)*	25	k_{25}	0.0006
13)	13	k_{13}	0.3	*29)*	26	k_{26}	0.0005
14)	19	k_{19}	0.3	*30)*	10	k_{10}	0.0002
15)	2	K_2	0.29	*31)*	21	K_{21}	0
16)	1	K_1	0.26	*32)*	23	k_{23}	0

Table 5-3: Ranking of processes of RCN

Ranking of parameters based on average relative sensitivity values over all variables. Reaction number refers to the numbering scheme used in Figure 2 to describe all processes of the RCN: "0" is used to label parameters describing total amount of conserved molecules, while letters are used to differentiate between parameters that describe a single processes.

Condition	Leading edge speed [μm/h]	Optic flow magnitude [μm/h]
DMSO / CCM	20.39 ± 6.78	10.92 ± 1.62
DMSO / WCM	18.53 ± 3.60	7.30 ± 2.34
ICG-001 / CCM	4.53 ± 4.14	6.56 ± 1.48
ICG-001 / WCM	8.86 ± 4.23	5.67 ± 1.27

Table 5-4: Speed of MDCK monolayers

Leading edge speed values correspond to average and standard deviation of measurements made in three independent experiments (N=3). Optic flow magnitude values correspond to average and standard deviation of measurements made in three independent experiments for 27 time points in each (N=81). CCM stands for Control Conditioned Media (constitutive condition) and WCM for Wnt3a Conditioned Media (activated condition). No inhibitor condition has DMSO (0.1% V/V); ICG-001 is added at 10μM.

Molecule measured / Variable calculated	Recreated condition	Experimental	Theoretical	source
α-catenin / $(\text{E-cad}^{\wedge}/\beta\text{-cat})_M$ + AJ	Reducing GPT by 0.4	1.8	1.48	Nita-Lazar *et al.*
γ-catenin / AJ	Reducing GPT by 0.4	2.5	2.66	Sengupta *et al.*
ABC / ABC	Reducing GPT by 0.45	0.4	0.56	Sengupta *et al.*, Nita-Lazar *et al.*
β-catenin / (β-cat/APC) + (β-cat /DC*) + (β-cat/TCF) + β-cat	Reducing GPT by 0.45	0.65	0.59	Sengupta *et al.*, Nita-Lazar *et al.*
β-catenin / (β-cat/APC) + (β-cat /DC*) + (β-cat/TCF) + β-cat	Increasing GPT by 4.5	3	2.86	Sengupta *et al.*
ABC / ABC	Increasing GPT by 4.5	3	3	Figure 5-8

Table 5-5: Matching experimental and theoretical results for parameter estimation

Values correspond to fold-change in steady-state concentrations upon downregulation or upregulation of DPAGT1 expression. Experimental results were obtained through Western blots or immunoprecipitation. Theoretical results correspond to steady-state solutions to RCN model. *denotes a phosphorylated species. ^ denotes an N-glycosylated species. All theoretical predictions were carried out for activated Wnt/β-catenin signaling (*i.e.* WNT^0 = 28.062 nM). Not all concentrations measured experimentally correspond to a simulated node in the network; the model cannot include all molecules in the cell. For example, experimental concentration of AJs was considered to be indicated by γ-catenin, a catenin associated with mature junctions [1].

5.9 Figures

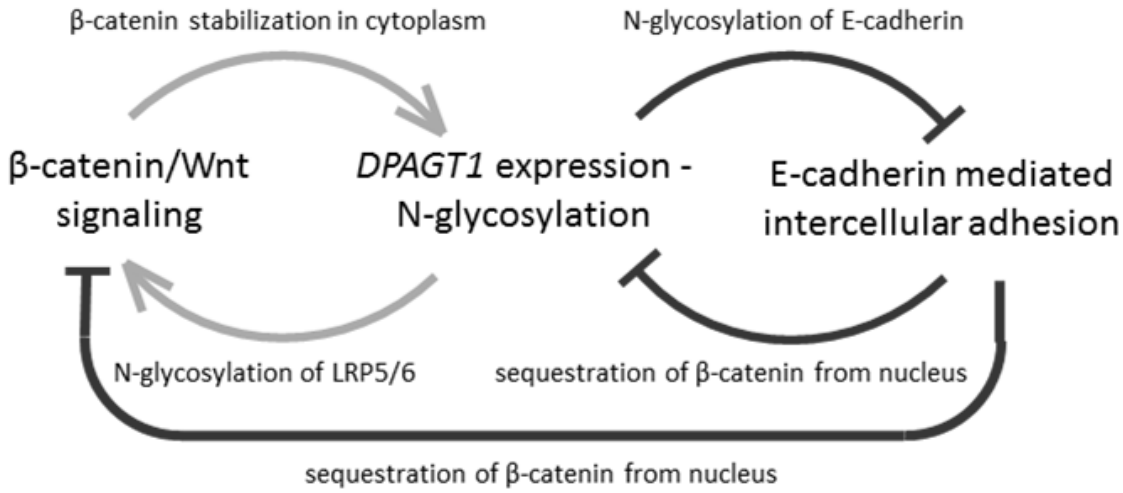

Figure 5-1: Schematic of general relationship between component pathways

Image adapted from (54).

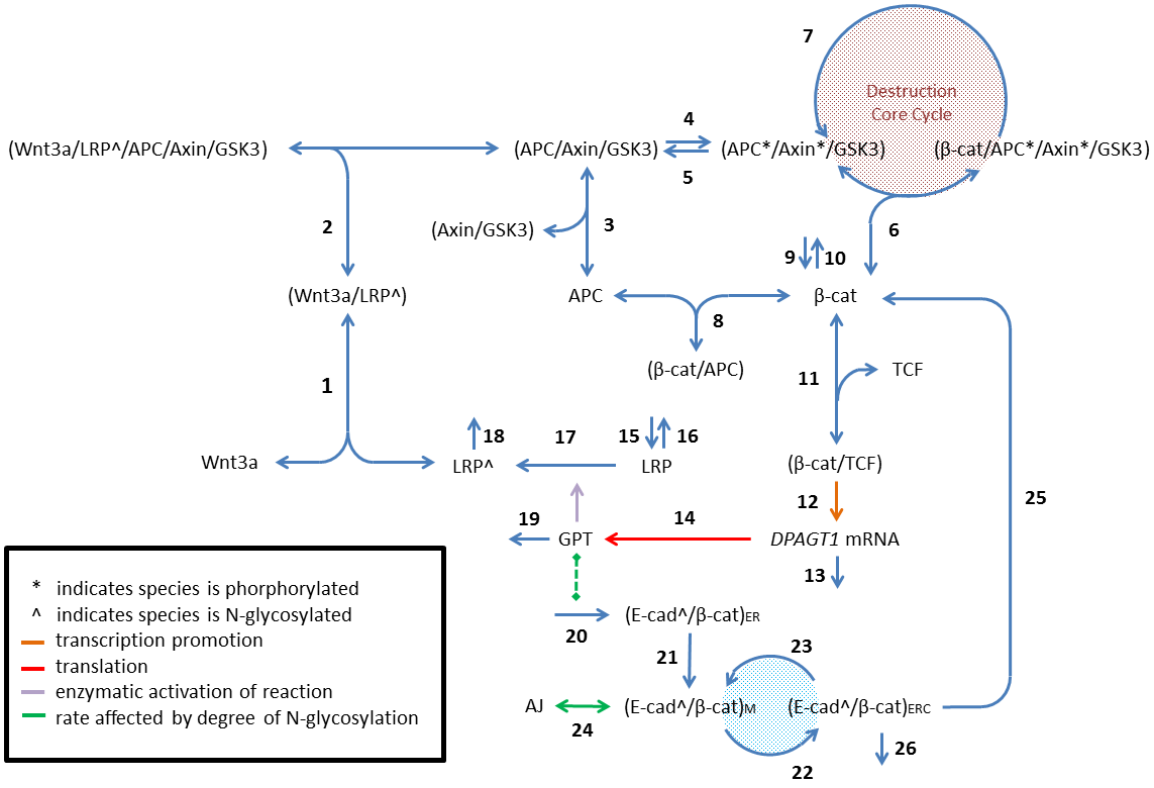

Figure 5-2: Reaction scheme

Protein complexes are enclosed in () with their components separated by /. Processes are numbered 1-26. Reactions 1-10 represent steps of Wnt/β-catenin signaling involved in active β-catenin regulation in the absence of Wnt3a. Reactions 11-19 represent regulation of Wnt3a binding by both genetic regulation of DPAGT1 and N-glycosylation. Reactions 20-26 represent E-cadherin dynamics and AJ formation. The abbreviations used are: APC, adenomatous polyposis coli; β-cat, β-catenin; E-cad, E-cadherin; ER, endoplasmic reticulum; ERC, endocytic recycling compartment; GSK3, glycogen synthase kinase 3β; LRP, lipoprotein receptor-related proteins; M, membrane; TCF, T-cell factor. Image partly adapted from (154).

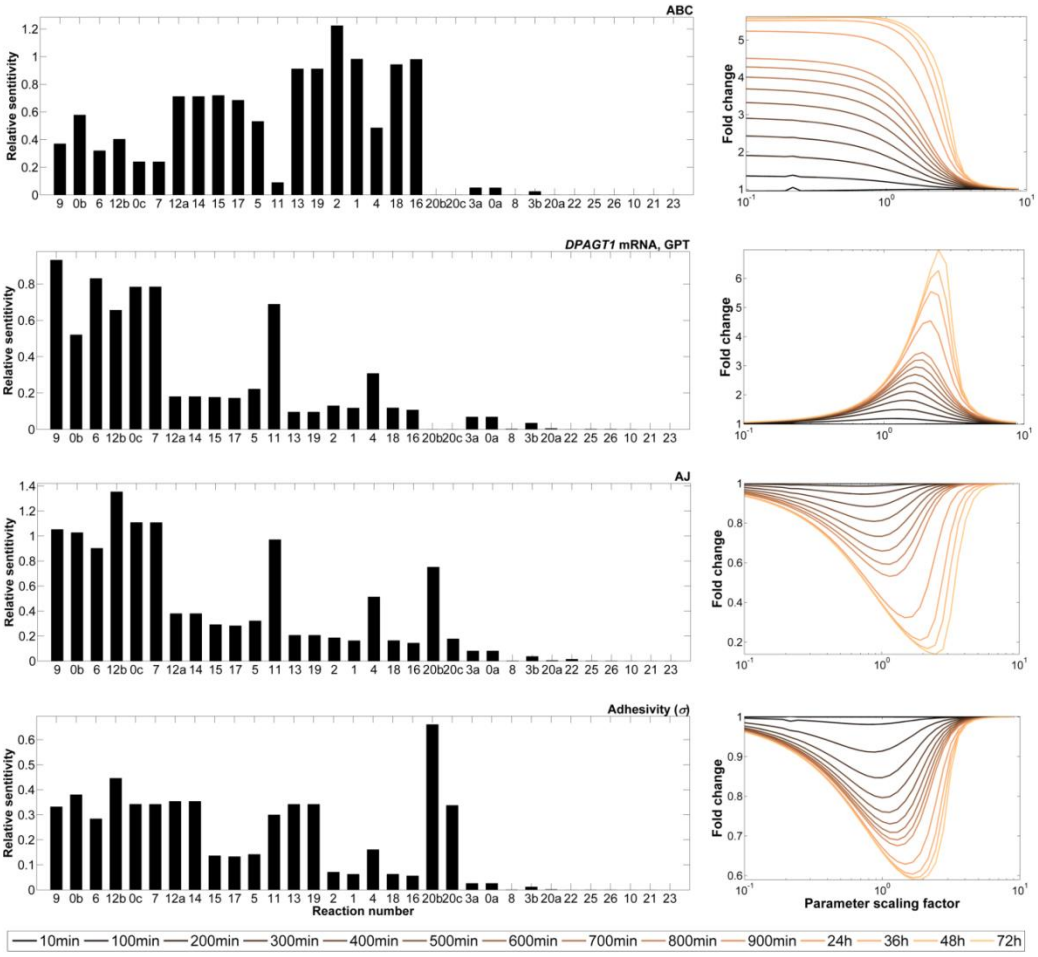

Figure 5-3: Sensitivities for select molecules in RCN

(LEFT) Sensitivity to changes in individual reactions of fold-change (upon activation of Wnt/β-catenin signaling) in ABC, *DPAGT1* mRNA and GPT, AJ, and E-cadherin adhesivity at steady-state. Reaction labels refer to numbering used in Figure 5-2; repeated numbers used for processes described by more than one parameter. Reaction labels along the horizontal axis are organized from left to right in order of decreasing impact on network concentrations. (RIGHT) Dependence of fold-change in chosen molecules in time to changes in reaction 11 (*i.e.* binding equilibrium of β-catenin and TCF). The horizontal axis represents the factor by which the parameter describing binding dynamics is scaled.

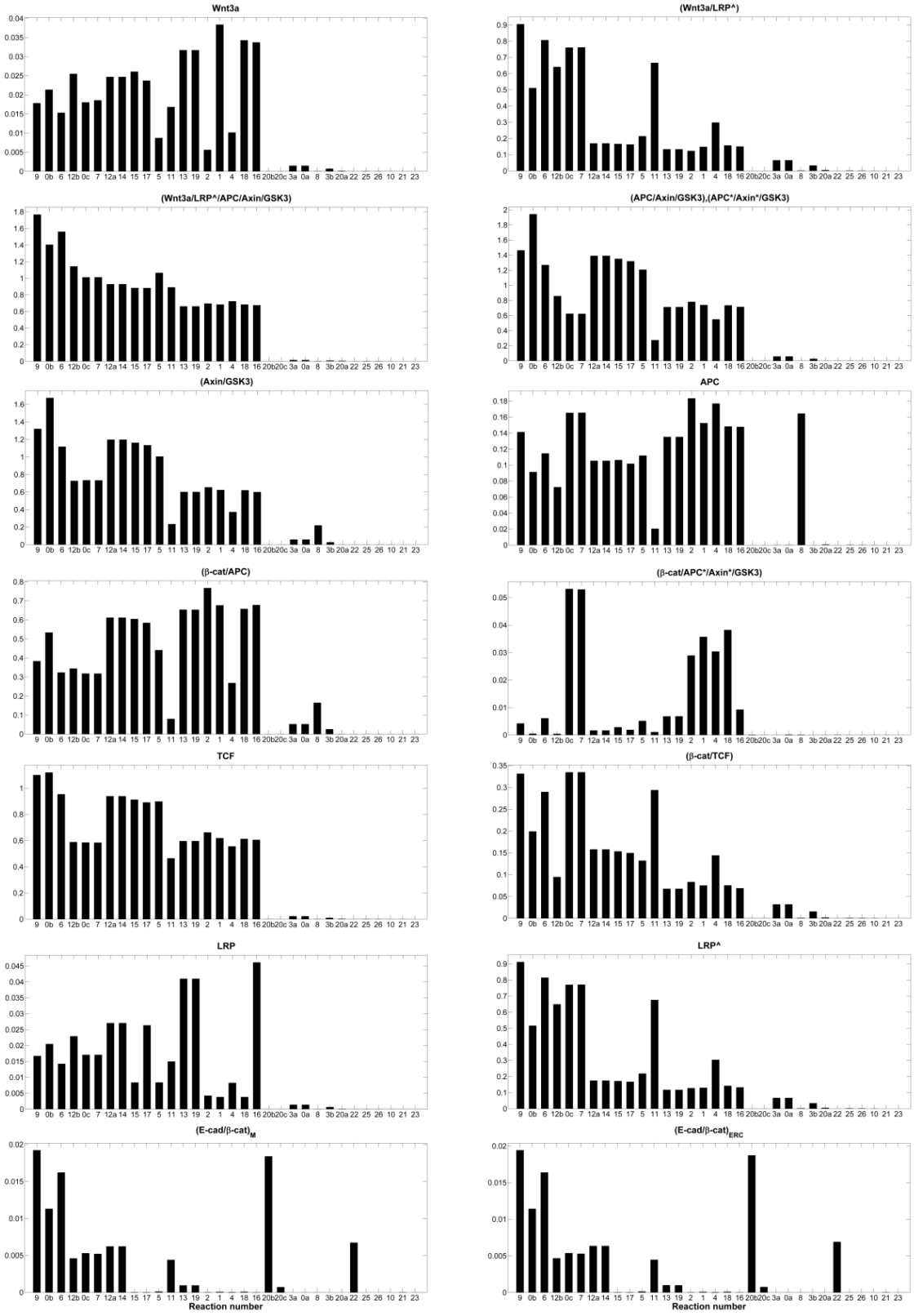
Wnt3a
(Wnt3a/LRP^)
(Wnt3a/LRP^/APC/Axin/GSK3)
(APC/Axin/GSK3),(APC*/Axin*/GSK3)
(Axin/GSK3)
APC
(β-cat/APC)
(β-cat/APC*/Axin*/GSK3)
TCF
(β-cat/TCF)
LRP
LRP^
(E-cad/β-cat)M
(E-cad/β-cat)ERC
9 0b 6 12b 0c 7 12a 14 15 17 5 11 13 19 2 1 4 18 16 20b20c 3a 0a 8 3b 20a 22 25 26 10 21 23
Reaction number

Figure 5-4**:** Relative sensitivity of all other molecules

Sensitivity of fold-change at steady-state to changes in individual reactions (upon activation with Wnt3a), except ABC, *DPAGT1* mRNA and GPT, AJ, and E-cadherin adhesivity (Figure 5-3). Reaction labels refer to numbering used in Figure 5-2; repeated numbers used for processes described by more than one parameter. Reaction labels along the horizontal axis are organized from left to right in order of decreasing impact on network concentrations.

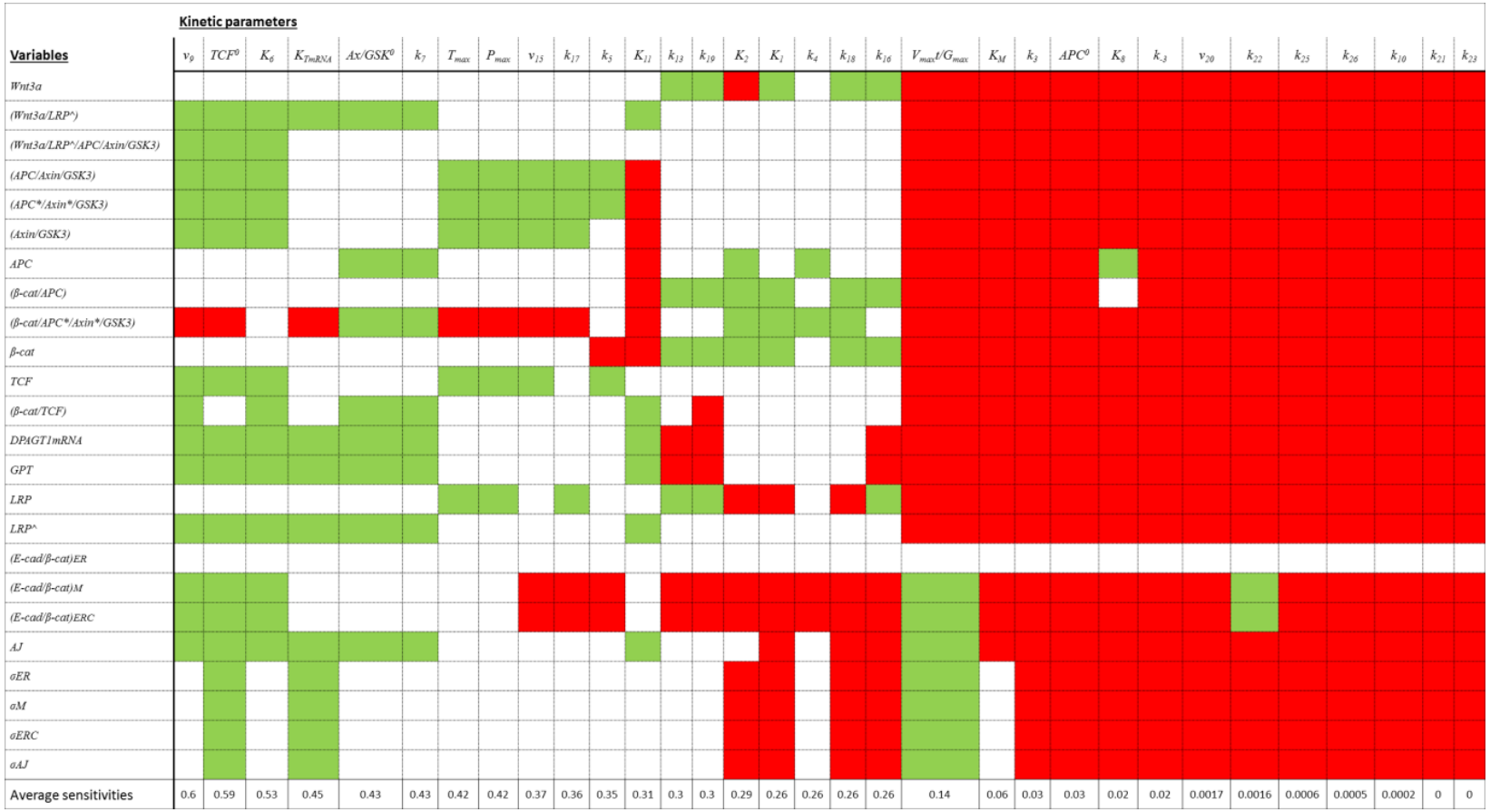

Figure 5-5: Parameters with most and least impact on each RCN molecule

Red signifies a relative sensitivity to a parameter (column) of fold-change in a variable (row), which is half of the average sensitivity of the variable to all parameters; green signifies a relative sensitivity to a parameter, which is half of the average to all parameters. Average sensitivities values in bottom row are the average relative sensitivity values of fold-change in all variables to a single parameter. All fold-change values are calculated based on concentrations at steady-state.

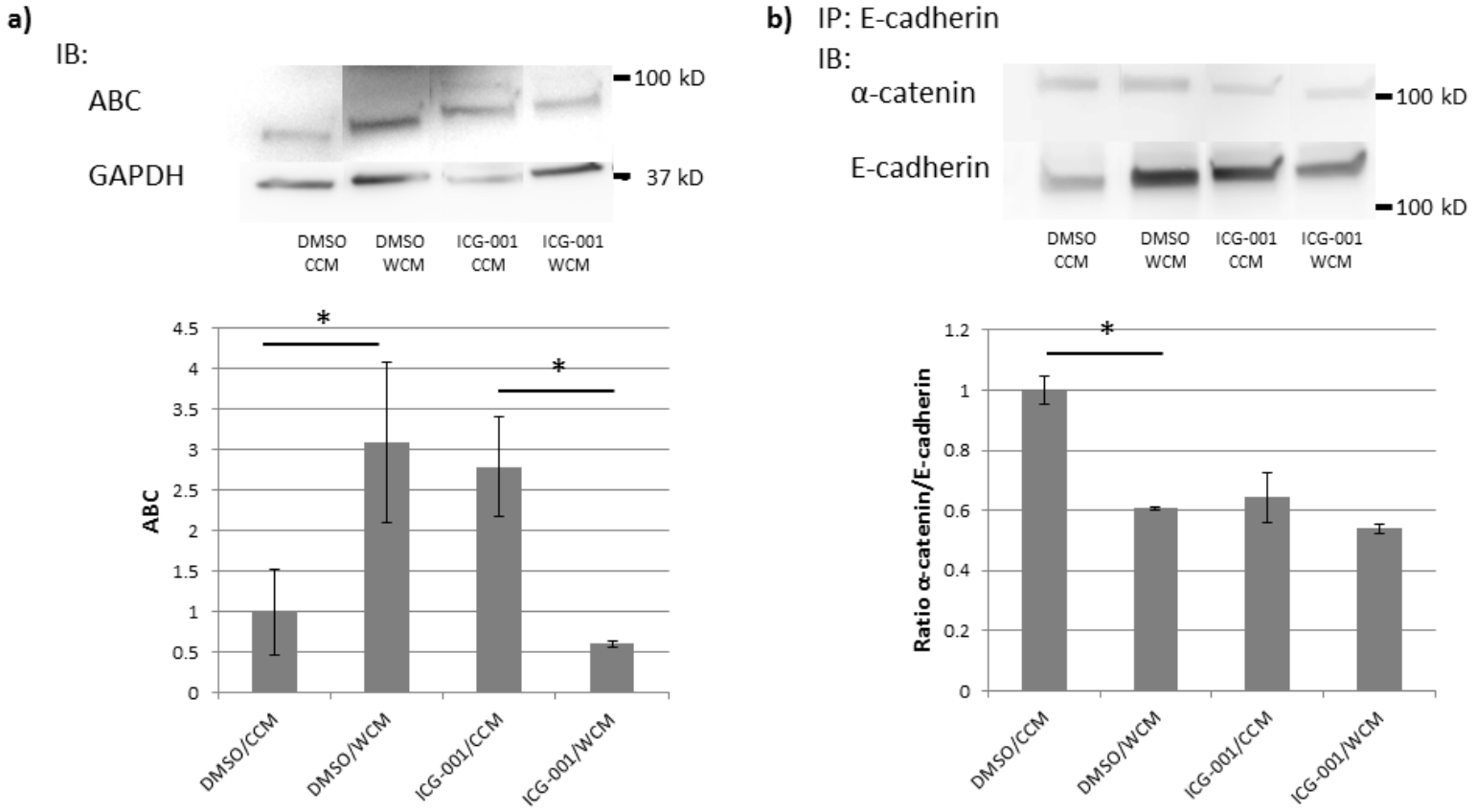

Figure 5-6: Representative immunoblots

MDCK cells were treated with: Either CCM or WCM, and either no inhibitor (DMSO) or ICG-001. a) Representative IBs of ABC in total cell lysates (TCLs). Quantified intensity values are averages; error bars represent standard error of the mean (N=4). b) Representative IBs of α-catenin and E-cadherin in precipitate from IP of E-cadherin from TCLs. Quantified intensity values are averages; error bars represent standard error of the mean (N=2). Blots were quantified and resulting values normalized to the DMSO/CCM condition. * represents statistically significant difference, $p<0.05$.

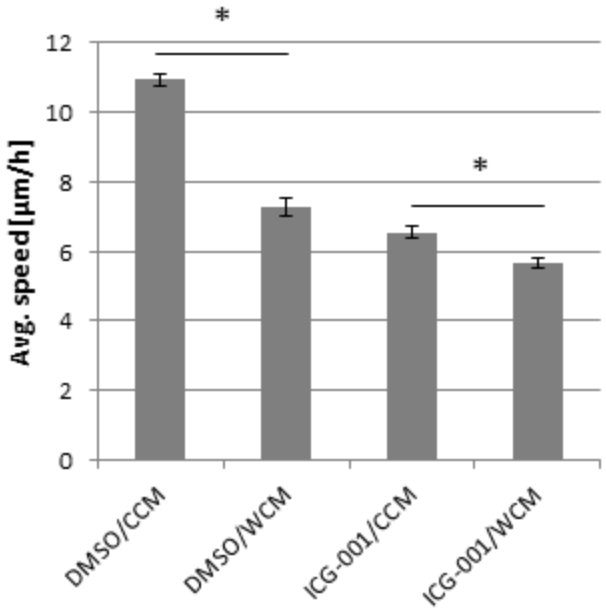

Figure 5-7: Average speed in an MDCK cell sheet

Average cellular speed in migrating MDCK cell sheets for cultures treated with: Either conditioned media with (WCM) or without (CCM) Wnt3a, and either no inhibitor (DMSO) or ICG-001.Values are the average (errors bars represent standard error of the mean) of three independent experiments for 27 time points in each (N=81). * represents statistically significant difference, $p<0.05$.

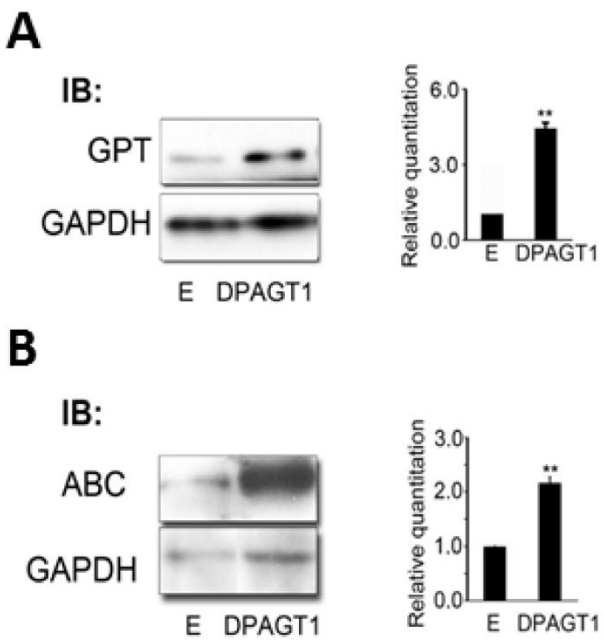

Figure 5-8: Blots displaying effects of *DPAGT1* upregulation

IBs of total cell lysates (TCLs) of MDCK cells transfected with an empty vector (E) or a *DPAGT1* transcript. A) Shows GPT levels and B) ABC levels. Blots were quantified and normalized to E condition. ** represents statistically significant difference, $p<0.01$.

CHAPTER 6. Multiscale Modeling of Collective Migration

Chapters 3 and 4 examined how migration relates to cluster-ECM interactions and epithelial disruption; however, dynamics of cells within clusters and the evolution of cell-cell junctions were left unaddressed. This chapter presents a multiscale model of cell clusters that incorporates a regulatory cell network (RCN) to account for variability in cellular speed in collective migration in 3D.

The resulting multiscale model is developed in parallel with an *in vitro* technique to create and observe mammalian epithelial cell clusters. By comparing the simulated dynamics to experimental measurements, the model provides insight into the independent contributions of physical forces and biochemical regulation to cellular cluster invasion.

By recording cellular positions in time, and matching average nuclear displacement and cluster size (*i.e.* number of cells) to simulated conditions, the model provides information on the physical interactions between neighboring cells. Further analysis on migration dynamics and simulated adherens junction (AJ) expression, reveals the relation between cluster shape, directionality, degree of collectivity, and adhesion.

6.1 Introduction

Cellular clusters of a few cells have been observed, *in vitro* and *in vivo*, to play a role during fetal development as well as in cancer metastasis (125, 126). Two defining characteristics of collective migration are sustained temporary or permanent cell-cell junctions and supracellular polarity (5). The nature of cell-cell junctions and cytoskeletal organization has been studied in two-dimensional *in vitro* models; phalloidin staining reveals the cytoskeletal arrangement, while force traction microscopy and PIV studies

provide insight into the contribution of adhesion and traction to collective behavior (21, 29, 30, 134).

In cluster migration specifically, given the dynamic nature of cell-cell boundaries, AJs are the principal link between cells. AJs constitute a protein complex, which has a cadherin molecule as the transmembrane protein binding to similar proteins on the membrane of neighboring cells. Particularly in epithelial tissues, E-cadherin forms homotypic bonds between cells (51). Only until recently have studies of 2D cell collectives looked beyond mechanotransduction and migration of the whole. E-cadherin expression at the membrane and the stability of AJs are shown to be dependent on regulation of gene expression and a related network of biochemical pathways (16, 54). This has not been studied in cell clusters in three-dimensional environments.

Most studies on collective dynamics in 3D have been performed either theoretically or on bacterial colonies or animal collectives (120, 179, 180). Despite the evident differences in the nature of units of these collectives, there are similarities in the observed patterns. This has led to the belief that these diverse systems can be described with common physical laws. SPP models have been successful in describing dynamics of bird and fish populations (120, 179, 180). SPP models, a subtype of agent-based models, restrict either direction of a particle, velocity, or both based on motion of neighboring particles (181). Recently, a SPP model was used to simulate the dynamics of a system of two distinct cell types on a two-dimensional surface (124). Nevertheless, no 3D SPP model has explored mammalian cell dynamics.

This chapter presents a first model of 3D mammalian cell clusters using SPP modeling. The model scales speed of the particles representing cells based on their degree of adhesion. By varying parameters representing influence of cells on their neighbors' preferred direction and mechanical attraction of repulsion between cells in contact, the model shows the influence of physical interactions between cells in cluster density, shape, and migration methods. These are quantities that have not been characterized for cell collectives in 3D and may be very revealing of invasive dynamics. In the case of density, for example, there are reports of crowding in 2D influencing collective motion (118).

By using an *in vitro* method for generation and observation of single cells in epithelial clusters in 3D, the multiscale model can be optimized to recreate cellular behavior. By incorporating a time regulation of formation of AJs, the model can then predict what is occurring in terms of cell-cell adhesion throughout the emergence of collective behavior. The experimental results reported in this chapter were obtained jointly with Dr. Yasha Sharma and reported in *Integrative Biology* (33).

6.2 Model Formulation

6.2.1 Self-propelled Particle (SPP) Model in 3D

Traditionally, SPP models assign a constant speed to a number N of particles initially placed at random in space. The direction of each particle is updated at every step based on an average of its neighbors' directions. This update rule is presented in Equation 6-1:

$$\theta_p^{t+1} = arg\left[\alpha \sum_{p\sim q} \boldsymbol{v}_q + \beta \sum_{p\sim q} \boldsymbol{f}_{pq} + N_p \eta \boldsymbol{u}_p^t\right] \quad (6\text{-}1)$$

where θ^{t+1} is the direction, $\boldsymbol{v}$ is the velocity, q are all neighbors within a specified radius of attraction, and η is a noise term. α and β are scaling factors taken from the work by Grégoire *et al.* (12); α scales the influence of the neighbors' velocities on the particle's preferred direction, while β scales the attraction or repulsion force ($\boldsymbol{f}_{pq}$) exerted on a particle p due to proximity to its neighbors q to ensure volume exclusion. N_p is the number of neighbors that influence a noise term η, a factor that scales a random unit vector $\boldsymbol{u}$.

The number of neighbors (N_p) is defined as number of particles within an equilibrium distance r_e = 20 μm. This value was selected because it is roughly equivalent to 1 cell diameter in 3D. The N_p value is set at a maximum of 12, which corresponds to maximal packing number assuming perfect spheres.

The model was adapted to 3D by making position, velocity, force, and noise vectors three-dimensional. The particles are seeded randomly onto positions of a 3D cube of dimensions L^3 with periodic boundaries. Each particle is assigned an initial direction by random assignment of a direction vector (θ,φ), where θ is the direction in the xy-plane, and φ is the angle from the z-axis. The range of these quantities is the following: $\theta \in [-\pi\ \pi]$ and $\varphi \in [0\ \pi]$. The direction vector (θ,φ) of any particle p at time step ($t+1$) can be converted to Cartesian coordinates ($\boldsymbol{C}_p\ (C_{x,p}\ ,\ C_{y,p}\ ,\ C_{z,p})$) by Equations 6-2 and 6-3:

$$\theta_p^{t+1} = arg\left(C_{x,p}^{t+1} + iC_{y,p}^{t+1}\right) \quad (6\text{-}2)$$

$$\varphi_p^{t+1} = arccos\left(\frac{C_{z,p}^{t+1}}{\sqrt[2]{\left(C_{x,p}^{t+1}\right)^2+\left(C_{y,p}^{t+1}\right)^2+\left(C_{z,p}^{t+1}\right)^2}}\right) \tag{6-3}$$

Equation 6-4 display the components of $\boldsymbol{C}_p$:

$$\begin{bmatrix} C_{x,p}^{t+1} = \alpha \sum_{p\sim q} v_{q,x} + \beta \sum_{p\sim q} f_{pq,x} + N_p \eta \cos\theta \sin\varphi \\ C_{y,p}^{t+1} = \alpha \sum_{p\sim q} v_{q,y} + \beta \sum_{p\sim q} f_{pq,y} + N_p \eta \sin\theta \sin\varphi \\ C_{z,p}^{t+1} = \alpha \sum_{p\sim q} v_{q,z} + \beta \sum_{p\sim q} f_{pq,z} + N_p \eta \cos\varphi \end{bmatrix} \tag{6-4}$$

The attraction/repulsion force term $\boldsymbol{f}_{pq}$, is described in Equation 6-5. This is essentially a modified Lennard-Jones potential:

$$\boldsymbol{f}_{pq} = \boldsymbol{e}_{pq} \begin{cases} -\infty & if\ r_{pq} < r_c \\ \frac{1}{4}\frac{r_{pq}-r_e}{r_a-r_e} & if\ r_c < r_{pq} < r_a \\ 1 & if\ r_a < r_{pq} < r_0 \\ 0 & if\ r_{pq} > r_0 \end{cases} \tag{6-5}$$

where $\boldsymbol{e}_{pq}$ is the unit vector along the direction between the two particles. This piecewise function assigns a magnitude to the force between neighboring particles based on the distance between them (r_{pq}). The different radii determining the limits of the different interactions are: r_c is the *core repulsion radius*, below which the force is repulsive. r_a is the *attraction radius*. r_0 is the *limit of interaction*, above which particles do not affect each other.

6.2.2 Scaling Parameters and Cell Speed Based on Adhesion

To emulate cellular systems the distances defining particle interactions and speed of the particles were scaled proportionally to experimental observations. To define the attraction and repulsion forces (Equation 6-5): r_c was set to 8 μm, a typical nucleus diameter; r_a was set to 32 μm, approximately 1.5 times a cell diameter; r_0 was set to 36 μm.

Taking each SPP step (*i.e.* simulation step) to correspond to 10min in real time, the maximum displacement in a single step was set to 2 μm. This means the maximum speed of the particles if they are not interacting with any other particle is 0.2 μm/min.

Because cells in collectives have been seen to move slower than single cells in 2D (125), the assumption was made that in 3D cluster migration cell-cell adhesion prevents cells from moving as fast as they would individually. Based on this, the migration step for each step is scaled based on each cell's expression of AJs. A linear scaling is chosen because of its simplicity and justified with the fact that each step corresponds to 10 minutes, an interval significantly larger than single E-cadherin bond lifetime (18); homotypic E-cadherin bonds are persistent and do not vary in strength based on intercellular forces. This relation is displayed in Equation 6-6:

$$\left|\boldsymbol{v}_p\right| = \left[\frac{-0.14}{\langle AJ_{eq}\rangle} AJ_p + 1\right] v_{max} \tag{6-6}$$

The magnitude of the speed for a particle p (v_p), is determined by scaling the maximum possible speed v_{max} = 0.2 μm/min by the scaling factor contained in straight

brackets. AJ_p stands for the AJ expression by particle p, while $<AJ_{eq}>$ is the approximate expression of AJs at equilibrium. The value of $<AJ_{eq}>$ is 1.43×10^{-4} nM, and it is determined from the RCN model presented in Chapter 5. The value -0.14 was chosen because the average cellular speed for cells in epithelial clusters was observed to be 0.172 μm/min, that is a 14% drop compared to v_{max}.

6.2.3 Integration of Regulatory Cell Network (RCN)

To combine both the cellular and intracellular scales in a multiscale model, the RCN model was incorporated into the modified SPP model in 3D. This consists in solving the RCN model within each SPP step with a shorter time step (*i.e.* RCN step). While the SPP step corresponds to 10 min of real time, the RCN step corresponds to 1 min. This means that for each SPP step, the RCN system is solved for ten steps.

After updating the direction of the simulated cells (*i.e.* particles in SPP model) according to Equations 6-2 and 6-3, the RCN is solved discounting formation and disassembly of AJs to determine the number of E-cadherin/β-catenin complexes expressed by each cell on the membrane. This requires a calculation of all neighboring relations. Then, based on E-cadherin/β-catenin expression for each pair of cells and adhesivity, as defined by degree of N-glycosylation (see Chapter 5), the number of AJs formed is determined for each pair of cells. The formed AJs with each neighbor are averaged (AJ_p) and the velocity is scaled as specified in Equation 6-6.

With the direction and speed determined, the position of each cell is updated. Before carrying on with the subsequent SPP step, AJs and adhesivity are updated for each cell given the new neighboring relations after displacement. This updates the

concentration of free membrane E-cadherin/β-catenin complexes (*i.e.* not forming AJs) available for recycling; in this way the SPP step affects what occurs inside the cell as well. A schematic of this relationship is presented as Figure 6-1.

6.2.4 Model Implementation and Simulated Conditions

The model is implemented in MATLAB (Mathworks, Natick MA). In between SPP steps, the differential algebraic equations (DAEs) describing the RCN are solved using the implicit solver ode15i. The system of equations is solved sequentially for groups of N/N_{node} cells; each group is addressed simultaneously by using MATLAB's parallel computing toolbox. Each simulation is run in a computer cluster with N_{node} nodes per core. A *parfor* (*i.e.* parallel for loop) structure is used to do this.

In order to quantify the impact of adding adhesion to a SPP model, two separate setups are implemented. First, the scaled SPP model is ran without integration of the RCN. A different setup consists of the multiscale SPP model, also referred to as the *variable speed SPP* model, because of scaling of particle speed as specified in Equation 6-6.

In the case of the first setup (*i.e.* scaled SPP model with no RCN), the system is initialized with N = 512 cells in a space of L = 1280 μm. Periodic boundaries are implemented. The simulations are run for 20,000 SPP steps. A single simulation was run for all possible combinations of the two following sets of α and β values: α-range (0, 0.01, 0.03, 0.05, 0.07, 0.1, 0.3, 0.5, 0.7, 1, 3, 5, 7, 10) and β-range (0, 0.01, 0.03, 0.05, 0.07, 0.1, 0.3, 0.5, 0.7, 1, 3, 5, 7, 10).

For the second setup (*i.e.* variable speed SPP model), the system is initialized with

N = 100 cells in a space of L = 743 μm; the particle density (*i.e. N/L*) is the same in both setups. Periodic boundaries are implemented. The simulations are run for 100,000 SPP steps, because more time is needed for AJ concentration to reach equilibrium. A single simulation was run for all possible combinations of the two following sets of α and β values: α-range (0, 0.01, 0.03, 0.1, 0.3, 1, 3, 10) and β-range (1, 2, 3, 6, 10, 20, 30, 60, 100). η, in Equation 6-1 and 6-4, is set to a value of 1 for most simulations, but varied for selected conditions deemed representative of behavior observed *in vitro*.

6.3 Experimental Validation

6.3.1 In vitro *3D Model of Epithelial Cell Clusters*

MDCK Type II epithelial cells are grown on tissue culture treated plastic at 37°C, 5% CO_2, and 70% humidity. Cells are cultured in DMEM media supplemented with 10% FBS and 1% penicillin/streptomycin. Cells are stably transfected to express nuclear localization signal (NLS) bound to GFP. Transfection is accomplished by a GFP-NLS plasmid (Clontech, Takara Bio, Japan) inserted with Lipofectamine 2000 (Invitrogen, Life Technologies, Grand Island, NY). To maintain high fluorescence in the cell population, cells with the plasmid are selected by adding 0.5 mg/ml G418 (Fisher Scientific, Pittsburgh, PA) to the media. Fluorescence activated cell sorting (FACS) selects for the brightest 1% of cells.

Clusters are formed by growing cells in suspension. Cells are trypsinized (Trypsin-EDTA solution, Sigma Aldrich, Saint Louis MO), passed through a 40 μm cell strainer (BD Biosciences, San Jose, CA) to be grown as single cells when seeded onto a

10 cm diameter Ultra Low Attachment Dish (Corning, Corning NY) in 10 ml media. After ~48 hours, clusters are extracted by passing the solution through either a 100 µm or a 70 µm cell strainer followed by a 40 µm cell strainer to select for clusters of 10-20 cells. These are re-suspended and centrifuged at 800 rpm, and then immersed in a 2 mg/ml collagen solution for 3D culture and imaging.

The 2 mg/ml collagen solution is prepared by mixing equal volumes of Type I collagen stock solution (BD Biosciences, San Jose, CA) and neutralizing buffer (100mM Hepes in 2× PBS, pH 7.3). Cell clusters are added to the 2 mg/ml collagen solution; 500 µl of this cluster-collagen suspension is seeded onto each well of a 24-well plate (MatTek, Ashland MA). The plates are incubated at 37°C, 5% CO_2 and ~ 70% humidity for 2 hours until the collagen has polymerized, after which ~1-2 ml of growth media is added to each well.

6.3.2 Image Acquisition

Images are acquired using a DMI600B Microscope (Leica, Solms, Germany) and ImagEM EM-CCD Camera (Hamamatsu Photonics, Hamamatsu, Japan) using a Spinning disk confocal setup (Yokogawa, Tokyo, Japan). Micro-Manager 1.4 Software (182) employs a 10× 0.3 NA objective lens to image multiple ~560 × 560 × 100 μm^3 fields of view. 3D stacks are acquired in the xy-plane with a z-step of 4 µm. Images of each FOV are taken every 10 minutes for 48-72 hours. Acquisition and analysis is restricted to cells clusters located at >100 µm from the glass bottom; this excludes cells that can sense the substrate beneath the 3D matrix behaving differently and proliferating as on a 2D substrate (183).

6.4 Quantifying Emergent Collective Dynamics

6.4.1 Cell Tracking

The raw data capturing the fluorescent nuclei are identified by using a 3D *feature finding algorithm* designed for concentrated fluorescent spheres in colloidal systems (184). The different parameters controlling the algorithm are optimized for nucleus tracking such that the number of features detected (N_F) matches visual examination and does output is not dependent on parameter. This last criterion is described by Equation 6-7:

$$\frac{dN_F}{dParameter} \cong 0 \tag{6-7}$$

Within the range of values explored, changing either expected nuclear diameter in the xy-plane or Z-direction did not alter N_F by more than 10% for an *xy-diameter* of 8 μm and *z-diameter* of 5 μm. The *mask* value is significantly larger and set at 13 μm for xy and 7 μm for z. The algorithm automatically discriminates between features separated by a minimum distance of half a diameter.

After identifying the features at individual FOVs at a single point in time, the different nuclei are associated in time, effectively tracking nuclei in space. The *tracking algorithm* searches for nearest neighbors at the subsequent image in time to find the feature that most likely represents the next position in the trajectory of a nucleus. Two input parameters optimized for are: minimum track duration $min(T_{track})$ and the maximum

distance traveled between consecutive time points $max(d_{cons})$. The most features were retained for a $min(T_{track})$ value of 6 μm and a $max(d_{cons})$ value of 5 μm (not shown). Therefore these values are established for the tracking algorithm. Features are retained in a track if they are missing for up to 3 time frames (half the minimal track duration).

Next, a *de-drifting algorithm* is implemented on the resulting tracks from the tracking algorithm; this de-drifting removes any motion common to all features in the frame (185). Drift is eliminated over 1 hour because externally induced stage drift occurs over a period of few hours.

In a last step before finalizing the nuclear tracks, a linear interpolation is used to *fill in missing positions* (*i.e.* gaps in time). This is not expected to affect analysis since features are only considered the same if gaps are no longer than 3 time steps.

6.4.2 Cluster Identification

With the tracks in place, the next step is the grouping of cells into clusters. For this a *clustering algorithm* developed by Sharma *et al.* is used (33). This algorithm uses a recursive function that labels cells with a cluster ID based on distance between cell nuclei. A *radius of interaction* (r_i) is used as the limit below which cells are considered part of the same cluster. It was determined heuristically that a values of r_i = 30 μm leads to proper cluster identification.

A cluster's identity also has to be assigned properly across time points. This *cluster correlation algorithm* assigns clusters that are believed to be the same in consecutive with the same cluster ID by maximizing cell retention (33). This algorithm handles events where two or more clusters merge.

6.4.3 Order Parameter

The degree of collectivity can be quantified through order parameters, determining the relative order of a system. These are system variables that change significantly marking phase transitions, they describe the degree of symmetry of the system (186). Mathematically, an order parameter adopts a value of 0 is the system is disordered, and a non-zero value in a different phase. For collective motion, a natural choice for the order parameter is normalized velocity (φ). Normalized velocity is defined in Equation 6-8:

$$\phi(t) = \frac{\left|\sum_{p=1}^{N} \boldsymbol{v}_p(t)\right|}{\sum_{p=1}^{N} |\boldsymbol{v}_p(t)|} \tag{6-8}$$

where p is an individual cells in a system, N the total number of cells, and $\boldsymbol{v}_p(t)$ is the velocity at time t.

6.4.4 Inertia Tensor

In addition to quantifying the order of the system, the change in shape is also analyzed. This is done by calculating the *inertia tensor* as if each nucleus corresponded to a rigid sphere in a body of multiple spherical units, and using the evolution in time of the eigenvector of the tensor to characterize orientation. The inertia tensor is described by Equation 6-9:

$$\bar{\bar{T}} = \sum_{p=1}^{N} m\left((\boldsymbol{r}_p \cdot \boldsymbol{r}_p)\bar{\bar{I}} - \boldsymbol{r}_p \otimes \boldsymbol{r}_p\right)$$

where $\bar{\bar{T}}$ is the inertia tensor, p is a unit, N the total number of units, m is a mass of each unit (taken to be 1 for all units, as all cells are considered equal), $\bar{\bar{I}}$ is the identity tensor, $\boldsymbol{r}_p$ is the position vector of particle p, and $\otimes$ is the tensor product.

Mathematically, the small eigenvector corresponds to the axis of the object along which most units are closest (*i.e.* the long axis); this is the axis with the least torque making rotation of the rigid body along this axis in particular more difficult. As a cell cluster is not a rigid body, this is only an approximation, but nonetheless, change in angle is indicative of change in orientation.

Change in shape is measured by calculating the average distance of cells in a cluster to the center of mass (CoM) of the cluster. Actual mass distribution for each cell is unknown, but similarly to calculation of the inertia tensor, the approximation is done by assuming the nuclei represent the position of the mass of the cell. This quantity does not represent shape directly, as it linearly increases with number of cells.

6.4.5 Interval Selection

In order to narrow down the periods at which the cluster migration is analyzed as well as removing any subjectivity to the analysis of collective behavior, the cell displacement was used to isolate the time periods over which clusters displayed collective behavior (*i.e.* motility events) as opposed to random motion.

Cell displacement was quantified as the average cellular speed over one hour; this quantity was squared to highlight instances of high motility. For selection of intervals of analysis, the median of the average speed for all cells in the cluster was used; this quantity is referred to as squared displacement median (SDM). Peaks in SDM were identified by first using MATLAB's peak finding algorithm, next merging peaks based on proximity to identify isolated motility events, and finally, using a threshold to isolate significant events. The details of this selection process can be found in Sharma *et al.* (33). A sample set displacement data from an MDCK cluster with the different steps in interval selection highlighted is presented in Figure 6-2.

6.5 Results

6.5.1 MDCK Clusters Display Temporal Heterogeneity

A total of twelve clusters found in two different collagen gels and five independent FOVs were tracked. These clusters were composed of 4-31 cells. Clusters were dynamic and exhibit spatial and temporal heterogeneity. An example of the total displacement observed over 48h for multiple clusters is presented in the planar projections and three-dimensional renderings of five clusters in two FOVs (Figure 6-3). Recorded displacements are in the order of 10-20 μm; these would not be considered relevant in two-dimensional studies but are in 3D.

This heterogeneity in motion was seen in that behavior included seemingly random movement, collective rotation, and collective translation. For cells translating collectively, the order parameter (*i.e.* normalized velocity) is high and close to 1. Instead,

for cells rotating collectively this parameter is low, ranging between 0 and 0.5: When rotating about an axis in the center of the cohort, the order parameter is 0, while for clusters rotating about an off-center axis, the order parameter is higher. In this way the order parameter is used to classify the different motility events identified according to the method presented in section 6.4.5.

Heterogeneity in collective motion is also evident from the different number of motility events that occurred in the 48-hour interval in which the cells were tracked. The SDM and order parameter for six clusters in the same gel are presented in Figure 6-4; the number of motility events varies between 3 and 11 for clusters found in the same environment. Rotation events seems to occur in short bursts, with a duration <2 hours. Meanwhile, translation events occur for up to 6 hours.

This behavior seems to be independent of external driving agents, as experiments were conducted under no externally imposed stimuli, such as a nutrient gradient. No internal gradient is believed to be imposed as the observed movement of clusters seems to occur at random. Figure 6-3 (panels C and D) presents a case of two clusters merging; however, there are examples of other similarly sized clusters that move in opposite directions (not shown).

6.5.2 SPP Models Can Recreate Mammalian Cell Cluster Dynamics

The scaled SPP model (without incorporating RCN dynamics) produced a wide ranging set of behaviors in the simulated clusters with varying values of parameters α and β. Figure 6-5 shows the end configurations of the system for select pairs of α and β values. This figure shows how behaviors ranged from random migration of all cells as

individuals (*e.g.* Figure 5-1a), through globular clusters similar to those observed *in vitro* (*e.g.* Figure 5-1e), to highly organized chain migration (*e.g.* Figure 5-1i).

It is apparent that for low values of α and β few clusters are formed. For high value of either α or β multiple clusters are formed, but some cells remain detached from any others throughout the whole simulation. In the case of both high α and high β, chain migration is observed.

A set of criteria was used to select conditions within the $\alpha\beta$-parameter space that may recreate cluster migration as observed in epithelial cell clusters. Three criteria were used: First, a median cluster size between 4-31 cells; second, a relatively high (*i.e.* between 0.6 and 1) average median order parameter (φ) over 1 hour; third, a median net cellular displacement between 3-7 μm over 1 hour. Table 6-1 shows what conditions in the $\alpha\beta$-parameter space met these criteria.

These results suggest that for the scaled SPP model the simulations with an α–range of (0.1, 1) and a β–range of (1, 10) can potentially emulate clusters observed *in vitro*.

The corresponding analysis of the variable speed SPP model with the same three criteria is presented in Table 6-2. In contrast to the simpler scaled SPP model, fewer conditions could emulate epithelial clusters. Specifically, (α,β)-pairs that meet all criteria are (3,20), (3,30), (3,100), and (10,60). This indicates that variable speed creates a finer balance between the need for attraction and guidance in cellular clusters. All values of both α and β are outside the range obtained from the simpler scaled SPP model. This indicates that by slowing down cells with adhesion both higher influence from neighbors

and attraction between cells is required for clusters to form.

Having further narrowed the area in $\alpha\beta$-parameter space, the effect of noise (η) was explored. This parameter was varied over two orders of magnitude, one below and one above the reference value $\eta = 1$. The resulting cellular configurations were parsed using the same criteria as in other simulations. The classification of simulated output is presented in Table 6-3. Specifically, (α,β,η)-sets that meet all criteria are (1, 1, 0.2), (3, 3, 0.1), (3, 20, 0.5), (3, 20, 1), (10, 60, 0.2), (10, 60, 1), and (10, 60, 5). This increased the number of cases that emulated *in vitro* clusters. This suggests a stochastic component is an important part of cluster formation in cellular systems. Specifically, lowering the noise lowered the value of β for which simulations emulated experiments; with less noise, attraction is not as important. Meanwhile, increasing the noise had little effect in getting more conditions that emulate *in vitro* clusters. Table 6-3 indicates that above a certain level, noise causes the displacement to no longer match with experimentally observed values, meaning the change in direction is no longer realistic.

Additionally, the number of clusters and the median size of the clusters (*i.e.* number of cells) were quantified for the different conditions in both scaled SPP and variable speed SPP simulations. The resulting plots displaying the values as colors on a plane covering the whole $\alpha\beta$-parameter space are called *phase plots*, due to their similarity with phase plots displaying phase transitions in physical systems. The phase plots for cluster number and size are displayed in Figure 6-6.

In the scaled SPP model, number of clusters has a biphasic relationship when α and β rise together; first the number of clusters rises and then drops. A balance of high α

with low β or alternatively, low α with high β, will lead to cluster formation. At low values of both parameters, the system remains as single cells, while at high values of both all cells will come together into very few chains. This suggests that to form clusters cells must find a balance between attraction and cues causing leader-follower relations to arise.

For the variable speed SPP model, phase plots for cluster number and size are also displayed in Figure 6-6. The dependence of these quantities on α and β is similar but less clear than in the scaled SPP model; variable speed adds stochasticity that seems characteristic of *in vitro* cellular migration.

6.5.3 α Determines Rise of Collectivity While β Determines Transition Dynamics

The order parameter was calculated for each individual cluster formed for the different conditions defined by choice of α and β, and the median was retrieved. The resulting phase plots are displayed in Figure 6-7. Comparison of normalized velocity calculations for all cells in the system and only for cells within each cluster, demonstrates the resulting heterogeneity that can arise with each condition.

These results show how a high value of α is enough to increase normalized velocity, indicating high collectivity independent of β. The system seems to undergo a phase transition with increasing α. This phase transition changes from what resembles a first order (*i.e.* displaying a discontinuity in φ) at high β values to a second order with decreasing β.

This is particularly true in the case of the scaled SPP model, where velocity is constant. Figure 6-7b indicates that a disordered system only occurs in the area of low α and high β; in this region, it is likely that with the contribution of neighbors' velocities

being negligible, cells may collide and repel each other. The attraction force is insufficient to counteract the constant velocity, especially if cells may move at random and more frequently away from each other compared to a condition with higher α. Comparing Figures 6-7b and 6-7d, suggests that this is true for the variable speed SPP model as well; however, after the increase in normalized velocity with α, there is a sharp drop when $\beta > 20$. This can be attributed to the high repulsion felt once the cells come too close due to increased α values. The difference with the simpler scaled SPP model is that the variable speed causes the attached cells to slow down, increasing the likelihood of them experiencing repulsion.

Adding dynamic regulation of adhesion makes the transition into an ordered phase more difficult. This explains the reduction in number of motility events that meet all the criteria determining whether the model emulates the behavior observed in epithelial clusters *in vitro*.

6.5.4 Adherent Cells Form Clusters with a Dense Core and Shifting Orientation

Figure 6-5 is a reminder of the diversity of cluster geometries that resulted from the different combinations of α and β. After looking at collectivity, the next step in characterization is to look at shape, orientation, and *internal diffusion* (*i.e.* movement of cells within a cluster).

Figure 6-8 displays the distance to the CoM for each cluster averaged over all existing clusters for each condition. As expected, the values are larger for the scaled SPP model compared to the variable speed SPP model, since more cells were included in the first setup. This highlights the necessity to take into account the size of the clusters when

looking at this metric. Despite the fact that clusters in the scaled SPP model relative to the multiscale model are twice as large (Figure 6-6), the distance to the CoM is five times as large. Further analysis of density will show that this is evidence of more tight packing inside the clusters with variable speed.

The phase plots showing distance to the CoM in Figure 6-8 appear monotonic; this means that this metric cannot be used to define clear phases. Chain migration, however, shows as peaks in the plots. Table 6-4 contains the measurements of distance to the CoM in MDCK clusters; the average distance was 20 ± 7 μm; this supports the choice of the conditions defined by (α,β) pairs (3,20) and (10, 60), excluding those with $\eta \neq 1$ as they are not shown in Figure 6-8c, as those best emulating *in vivo* clusters.

Next the orientation of the clusters in the different conditions was analyzed by looking at the change in angle in consecutive time points for the shortest principal eigenvector of the inertia tensor. The results are presented in Figure 6-8. The angle ranges between ~0.1 and ~1.5 rad in both the scaled SPP and variable speed SPP models. Some relations between shape and angle are expected; for example, chain migration displays the lowest changes in orientation. In contrast, conditions defined by low α and low β values, where clusters are transiently formed by very few cells that randomly collide, are characterized by the largest angles.

The more interesting are the low α / high β conditions and high α / low β conditions; both show a large change in orientation. Low α / high β conditions have high changes in orientation due to the strong repulsion and attraction forces, causing constant fluctuations in shape. High α / low β conditions, instead, change orientation due to cluster

size; with a few cells, there is less resistance to a change in orientation. Without a large value of β, however, it is less likely repulsion or attraction will cause the cluster to change orientation. This explains why for variable speed SPP, the change in orientation between these two sets of conditions is more similar than in the scaled SPP model.

The angle between consecutive eigenvectors as a metric did not help directly compare MDCK clusters with specific simulated conditions; *in vitro* clusters have a change in orientation of 1 ± 1 rad, as shown in Table 6-4. This is a wide range that includes all simulated values.

In addition to change in orientation and average distance to CoM, the number of neighbors at the center and edge of each cluster were quantified. The center and edge of cluster were defined as the cells in the cluster that are closest and farthest from the CoM respectively. Additionally, if the same cell remained in either position in consecutive time points, the identities of the neighbors were checked to see how many neighboring relations were kept in time for the different conditions defined by α and β. Figure 6-9 shows these results for the scaled SPP model, and Figure 6-10 shows them for the variable speed SPP model.

Figure 6-9 shows no evident difference in number of neighbors in the center and the edge of the cluster. Meanwhile, Figure 6-10 shows how with variable speed, the number of neighbors at the edge is lower. This indicates that the cluster is denser near its center in the variable speed case. There is little dependence of number of neighbors on α and β; similarities between phase plots for median cluster size (Figure 6-6) and number of neighbors show that the latter is probably dependent on size.

Regarding conservation of neighbors as indicative of *internal diffusion*, comparison of Figures 6-9 and 6-10 reveals the reversal of trend between center and edge between scaled SPP and variable speed SPP models. While in the scaled SPP model more neighbors are conserved at the edge, in the variable speed SPP model more neighbors are conserved at the center. This can be attributed to adhesion causing cells to slow down once attached, delaying any internal diffusion. Also, increased density of the cluster near the center will make movement more difficult given that the model incorporates volume exclusion.

Number of neighbors and conserved neighbors at the center and edge for MDCK clusters are reported in Table 6-5. Number of neighbors is lower in *in vitro* clusters than in simulated clusters. This is partly because of the size of the clusters; MDCK clusters ranged from 4-31 cells, and simulated clusters with comparable normalized velocity were larger. Another factor determining this is that cells in fibrous environments have log extensions that create more interactions with cells despite apparent distance.

Nonetheless, there are similarities between experimental and simulated results. Simulated results from the scaled SPP model match experimental observations in the equal number of neighbors at the edge in comparison to the center of the cluster. Also, simulated results from the variable speed SPP model match experimental observations in the lower number of conserved neighbors at the edge in comparison to the center of the cluster. Together, these similarities indicate that adhesion may be properly scaling speed, but the attraction/repulsion force could be scaled differently to prevent a denser core from forming in simulated clusters while maintaining realistic neighboring relations.

6.5.5 Decreased Cell-cell Adhesion Occurs During Motility Events

In the multiscale model, or variable speed SPP model, AJs were used to nominally quantify adhesion and, more importantly, scale speed. Average AJ expression for each cluster formed was calculated, then averaged for the clusters in each condition, and displayed in Figure 6-11.

A comparison with Figure 6-7d, presenting the median order for the same conditions, shows some similarity. Most disordered clusters appear to have low adhesion. This explains why AJ expression seems to increase with α, at least up to $\alpha < 3$. Increased collectivity gives cells a chance to stay together and form junctions. There is a significant difference between phase plots for median order and AJ expression; at high α of and low β values AJ expression is low despite the high degree of collectivity. This, in turn, is explained by the low number of conserved neighbors (Figure 6-10d).

In cases with relatively high β values, repulsion plays a significant role in emerging dynamics. This exemplifies how the non-equilibrium nature of SPP systems (*i.e.* input of energy at every SPP step with migration) will cause this repulsion to prevent stable AJ formation. Nevertheless, for all explored β values, with increasing α value the average expression of AJs increases before dropping.

AJ distribution was tracked during motility events for conditions that are believed to most closely emulate MDCK clusters. The median concentration and upper and lower quartiles are displayed in Figure 6-12. Despite increasing adhesion with continued cell-cell contacts, a drop in AJ expression is observed in the four motility events analyzed in Figure 6-12. This suggests that reduced adhesion contributes to emergence of collective

migration in variable speed SPP systems.

Simultaneously, the distribution of active β-catenin (ABC) was also tracked, along with other molecules revealed as relevant to E-cadherin mediated adhesion in Chapter 5 (not shown). There was no significant change in expression with changing values of α and β. This is explained by the results of the analysis on the RCN performed in Chapter 5 revealing that the RCN is insensitive to E-cadherin recycling (Section 5.5.6). Given that no protein concentration is changed inside the simulated cells, the only change in concentration occurs at the cell surface.

6.6 Discussion

The study of collective migration is important to the understanding of many biological processes. The diversity of environments through which cells move present both a challenge to understanding migration, but also provide insight into the mechanisms involved. The occurrence of cluster migration through EMT in development and metastasis suggest that it can occur regardless of some environmental cue. The techniques presented in this chapter provide not only a model *in vitro* system that consistently displays epithelial cluster migration but also permit probing of collective dynamics. These dynamics are compared to theoretical studies, to discern between physical and biological contributions to collective invasion in 3D.

Here, theoretical studies include a traditional SPP model expanded to 3D and a multiscale model that takes into account protein bonding dynamics describing the formation of AJs. Analysis of real and simulated clusters showed that displacement of the cluster can be emulated by the SPP models. The stochastic motion that is characteristic of

cellular migration, in both 2D and 3D, was recreated and quantified. The models demonstrate that two major physical parameters are enough to recreate multiple migration modes: single cell, globular cluster, and chain migration. The two factors were effect of neighbors on direction (*i.e.* α) and attraction-repulsion strength (*i.e.* β). With normalized velocity as the chosen order parameter, change in alpha was found to cause a phase transition. Similarly, measurements of neighboring relationships within clusters also show dependence of transition order on this parameter. Comparing the standard SPP model with a variable speed one intended to model adhesive cellular systems showed that biological factors contribute to the emergent dynamics observed in real cellular systems in 3D.

The linear equation (Equation 6-6) chosen to describe the relation between velocity and adhesion is representative of a biological component. It represents regulation of velocity of each cell based on recent history of adhesion. This factor narrowed down the conditions for which simulated clusters resembled real clusters. Further inclusion of biological factors such as adhesion regulation through the RCN, presented in Chapter 5, can potentially play a role given external stimuli such as changing extracellular ligand availability. As discussed in Chapter 4, a diffusion-based gradient can be implemented to test the effects of paracrine signaling. Additionally, the behavior of a cluster in a pathological condition can also be modeled with the multiscale SPP model here presented; this would correspond to simulation of a dysregulated intracellular network as presented in Chapter 5.

6.7 Tables

↓α/β→	0	0.01	0.03	0.05	0.07	0.1	0.3	0.5	0.7	1	3	5	7	10
0	✓ ✓	✓ ✓	✓ ✓	✓ ✓	✓ ✓	✓ ✓	✓ ✓	✓ ✓	✓ ✓	✓	✓	✓	✓	✓
0.01	✓ ✓	✓ ✓	✓ ✓	✓ ✓	✓ ✓	✓ ✓	✓ ✓	✓ ✓	✓ ✓	✓	✓	✓	✓	✓
0.03	✓ ✓	✓ ✓	✓ ✓	✓ ✓	✓ ✓	✓ ✓	✓ ✓	✓ ✓	✓ ✓	✓ ✓	✓	✓	✓ ✓	✓ ✓
0.05	✓ ✓	✓ ✓	✓ ✓	✓ ✓	✓ ✓	✓ ✓	✓ ✓	✓ ✓	✓ ✓	✓	✓	✓	✓	✓
0.07	✓ ✓	✓ ✓	✓ ✓	✓ ✓	✓ ✓	✓ ✓	✓ ✓	✓ ✓	✓ ✓	✓ ✓	✓	✓ ✓	✓ ✓	✓ ✓
0.1	✓ ✓	✓ ✓	✓ ✓	✓ ✓	✓ ✓	✓ ✓	✓ ✓	✓ ✓	✓ ✓	✓ ✓	✓	✓	✓	✓ ✓
0.3	✓ ✓	✓ ✓	✓ ✓	✓ ✓	✓ ✓	✓ ✓	✓ ✓	✓ ✓	✓ ✓	✓ ✓ ✓	✓ ✓	✓ ✓	✓ ✓ ✓	✓ ✓
0.5	✓ ✓	✓ ✓	✓ ✓	✓ ✓	✓ ✓	✓ ✓	✓ ✓	✓ ✓	✓ ✓	✓ ✓ ✓	✓ ✓ ✓	✓ ✓ ✓	✓ ✓ ✓	✓ ✓ ✓
0.7	✓ ✓	✓	✓	✓ ✓	✓ ✓	✓ ✓	✓ ✓	✓ ✓	✓ ✓	✓ ✓ ✓	✓ ✓ ✓	✓ ✓ ✓	✓ ✓ ✓	✓ ✓ ✓
1	✓	✓	✓	✓	✓	✓	✓	✓	✓ ✓	✓ ✓ ✓	✓ ✓ ✓	✓ ✓ ✓	✓ ✓ ✓	✓ ✓ ✓
3	✓	✓	✓	✓	✓	✓	✓	✓ ✓	✓	✓	✓	✓	✓ ✓	✓ ✓
5	✓	✓	✓	✓	✓	✓ ✓	✓ ✓	✓	✓	✓	✓ ✓	✓	✓ ✓	✓
7	✓	✓	✓	✓ ✓	✓ ✓	✓ ✓	✓	✓	✓	✓	✓	✓	✓	✓
10	✓	✓	✓	✓ ✓	✓ ✓	✓	✓	✓	✓ ✓	✓	✓	✓ ✓	✓	✓

Table 6-1: Scaled SPP simulations compared with *in vitro* clusters

Simulated conditions in the *αβ*-parameter space compared to *in vitro* cluster migration: Black checkmark indicates a median cluster size between 4-31 cells. Blue checkmark indicates a relatively high (*i.e.* between 0.6 and 1) average median order parameter (φ) over 1 hour. Red checkmark indicates a median net cellular displacement between 3-7 μm over 1 hour.

↓α/β→	1	2	3	6	10	20	30	60	100
0	✓ ✓	✓	✓		✓	✓	✓	✓	
0.01	✓ ✓	✓	✓	✓	✓	✓	✓		
0.03	✓ ✓	✓	✓	✓	✓	✓	✓	✓	
0.1	✓ ✓	✓	✓	✓	✓	✓	✓	✓	
0.3	✓ ✓	✓	✓	✓	✓	✓	✓	✓	✓
1	✓ ✓	✓ ✓	✓ ✓	✓ ✓	✓ ✓	✓ ✓	✓ ✓	✓ ✓	✓ ✓
3	✓ ✓	✓ ✓	✓ ✓	✓	✓	✓ ✓ ✓	✓ ✓ ✓	✓ ✓	✓ ✓ ✓
10	✓	✓	✓	✓ ✓	✓ ✓	✓ ✓	✓	✓ ✓ ✓	✓ ✓

Table 6-2: Variable speed SPP simulations compared with in vitro clusters

Simulated conditions in the *αβ*-parameter space compared to *in vitro* cluster migration: Black checkmark indicates a median cluster size between 4-31 cells. Blue checkmark indicates a relatively high (*i.e.* between 0.6 and 1) average median order parameter (φ) over 1 hour. Red checkmark indicates a median net cellular displacement between 3-7 μm over 1 hour.

α	↓β/ η→	0.1	0.2	0.5	1	2	5	10
1	1	✓ ✓	✓ ✓ ✓	✓ ✓	✓ ✓	✓ ✓	✓ ✓	✓ ✓
3	3	✓ ✓ ✓	✓ ✓	✓ ✓	✓ ✓	✓ ✓	✓ ✓	✓ ✓
3	20	✓	✓	✓ ✓ ✓	✓ ✓ ✓	✓ ✓	✓ ✓	✓
10	60	✓	✓ ✓ ✓	✓ ✓	✓ ✓ ✓		✓ ✓ ✓	✓ ✓
1	3	✓	✓	✓	✓ ✓	✓	✓	✓ ✓
3	1	✓	✓ ✓	✓	✓ ✓	✓	✓ ✓	✓ ✓

Table 6-3: Effect of noise on variable speed SPP simulations

Simulated conditions in the *αβ*-parameter space compared to *in vitro* cluster migration: Black checkmark indicates a median cluster size between 4-31 cells. Blue checkmark indicates a relatively high (*i.e.* between 0.6 and 1) average median order parameter (φ) over 1 hour. Red checkmark indicates a median net cellular displacement between 3-7 μm over 1 hour.

Cluster	**distance to CoM (µm)**	**Δangle eigenvector**
Gel I FOV 1 C1	20.9 ± 7.1	0.5 ± 0.9
Gel I FOV 1 C2	22 ± 8	1 ± 1
Gel I FOV 1 C3	20.5 ± 7.1	1.1 ± 1.4
Gel II FOV 1 C1	15.54 ± 5.27	0.9 ± 1.3
Gel II FOV 1 C2	22 ± 8	1 ± 1
Average ± SD	20 ± 7	1 ± 1

Table 6-4: Distance to center of mass and change in orientation in MDCK clusters

Distance to center of mass (CoM) approximated from nuclear positions. Angle values (in radians) correspond to change between consecutive time points for smallest principal eigenvector. Average values and standard deviation for MDCK clusters calculated for measurements every 10 min for 48 hours (N = 288).

Cluster	Number in center	Number in edge	Conserved in center	Conserved in edge
Gel I FOV 1 C1	5.2 ± 1.9	5.1 ± 2.1	5.1 ± 1.5	4.3 ± 1.7
Gel I FOV 1 C2	5 ± 2	5 ± 2	4 ± 2	3 ± 2
Gel I FOV 1 C3	3.7 ± 1.7	3.9 ± 2.1	3 ± 1.5	2.7 ± 0.8
Gel II FOV 1 C1	2.5 ± 0.9	2.5 ± 0.9	2.5 ± 0.8	1.7 ± 0.5
Gel II FOV 1 C2	4 ± 1	4 ± 1	3 ± 2	3 ± 1
Average ± SD	4 ± 2	4 ± 2	4 ± 2	3 ± 1

Table 6-5: Number of neighbors in MDCK clusters

Second and third columns contain number of neighbors to cell closest and farthest from the CoM for each cluster, respectively. Fourth and fifth columns contain number of neighbors of cells closest and farthest from CoM, respectively, conserved between consecutive time points for each cluster. Average values and standard deviation for MDCK clusters calculated for measurements every 10 min for 48 hours (N = 288).

6.8 Figures

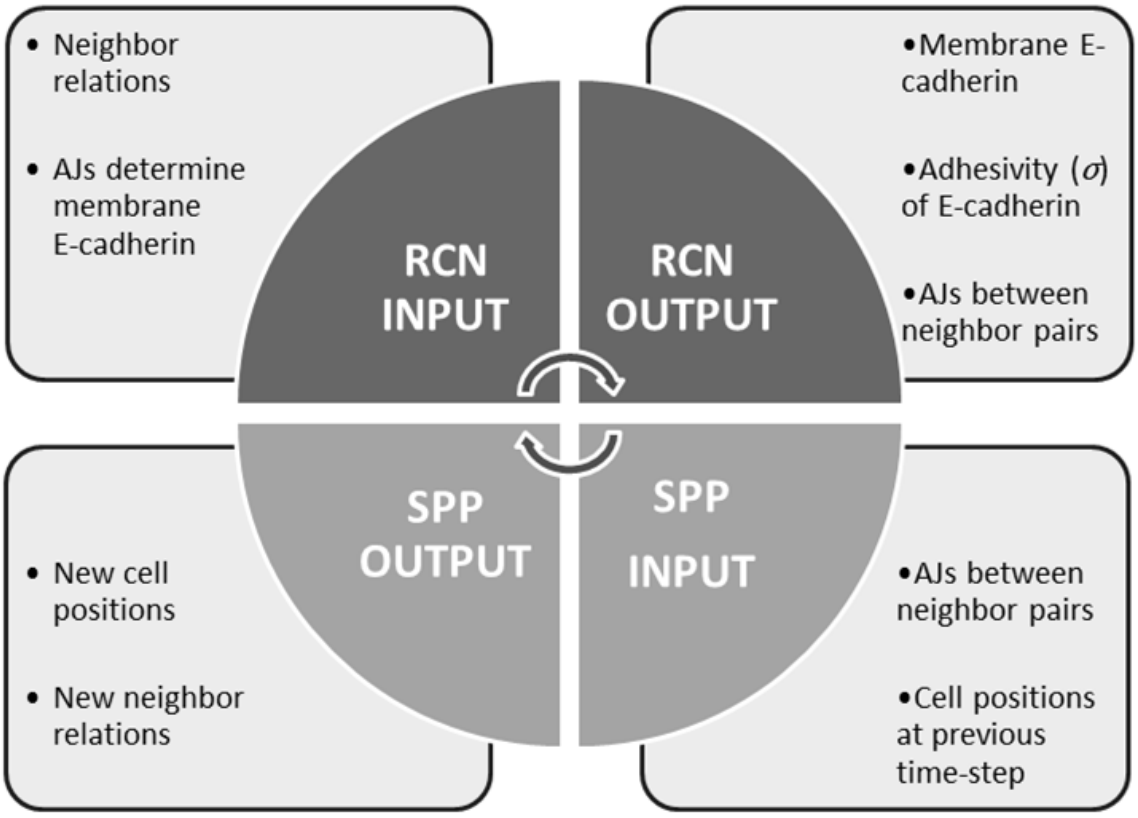

Figure 6-1: Schematic of integration of multiple scales

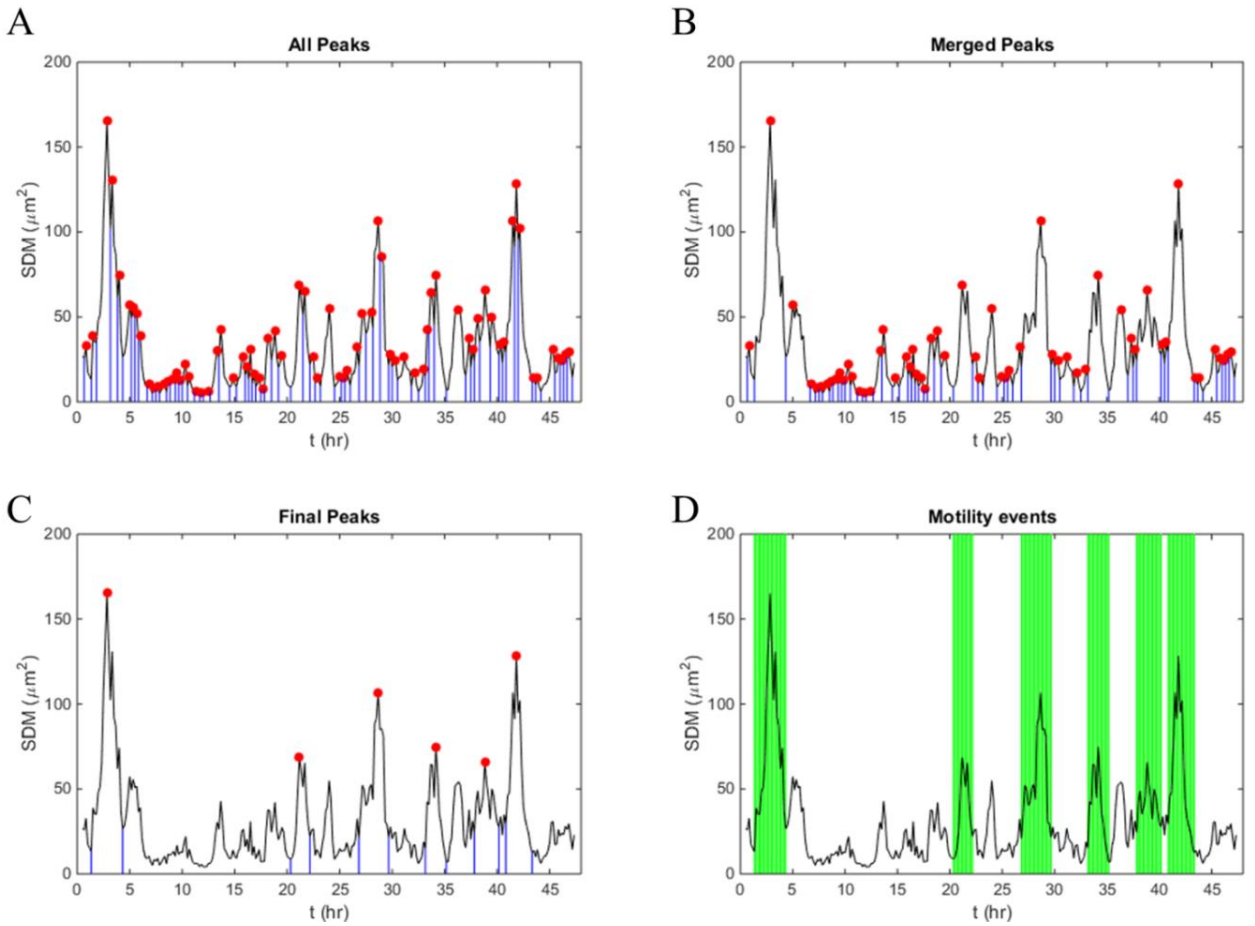

Figure 6-2: Interval selection algorithm

SDM data vs. time for a single MDCK cluster tracked over 48 h. SDM is depicted in all four panels representing the stages in the interval selection algorithm: A) All peaks (red dots) and their borders (blue) identified by MATLAB's peak finding algorithm. B) Peaks remaining after merging step. C) Peaks remaining after applying a threshold on the magnitude. D) Final identified motility events are shaded in green.

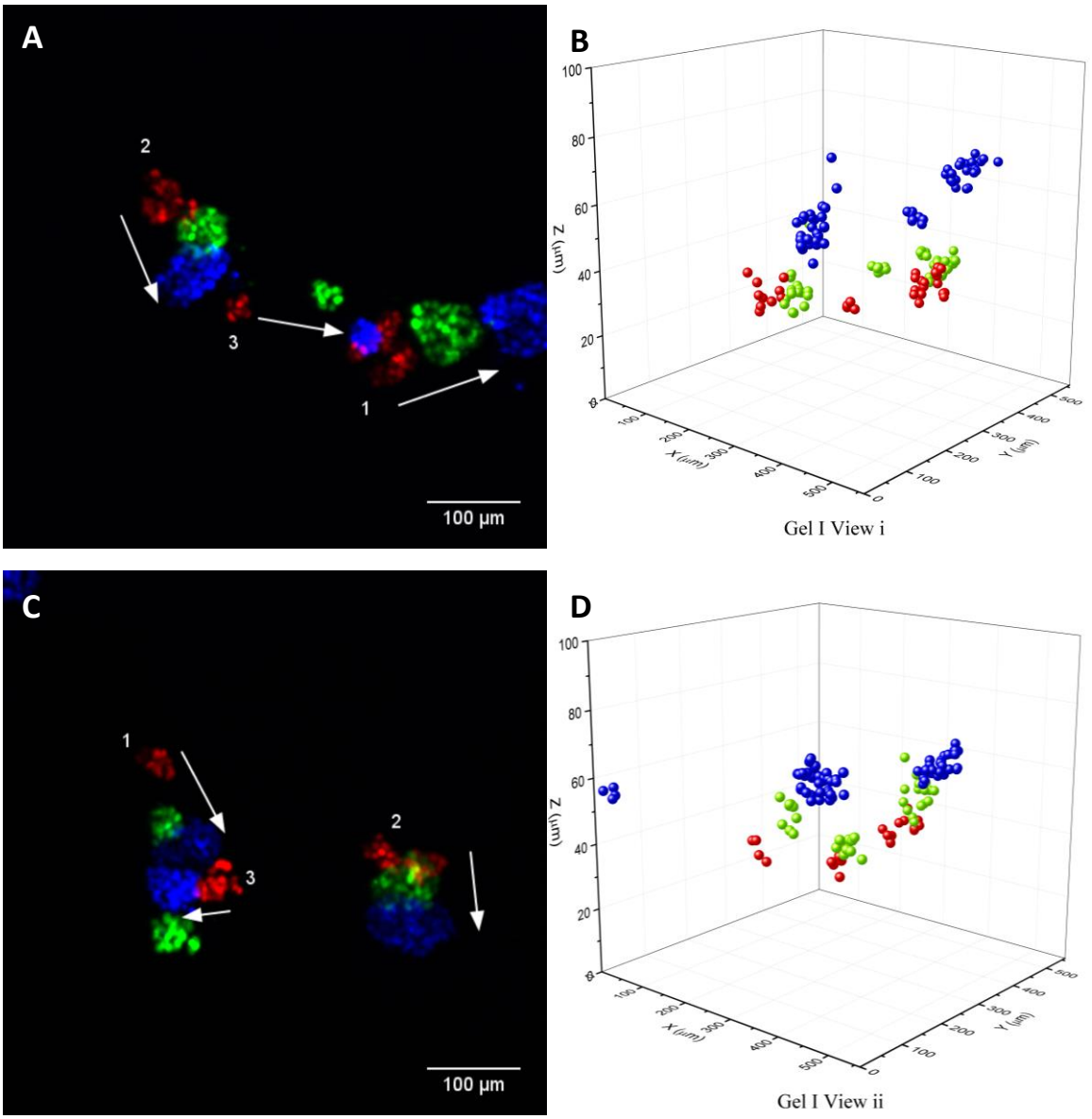

Figure 6-3: Examples of MDCK cluster migration over 48h

Panels A and C show z-projections of two FOVs from the same 3D collagen gel at 0 h (red), 24 h (green) and 48 h (blue). Panels B and D are 3D renderings of nuclear tracking corresponding to Panel A and C respectively. The numbers in white indicate cohort number as determined by a clustering algorithm. Image taken from Sharma et al. (33).

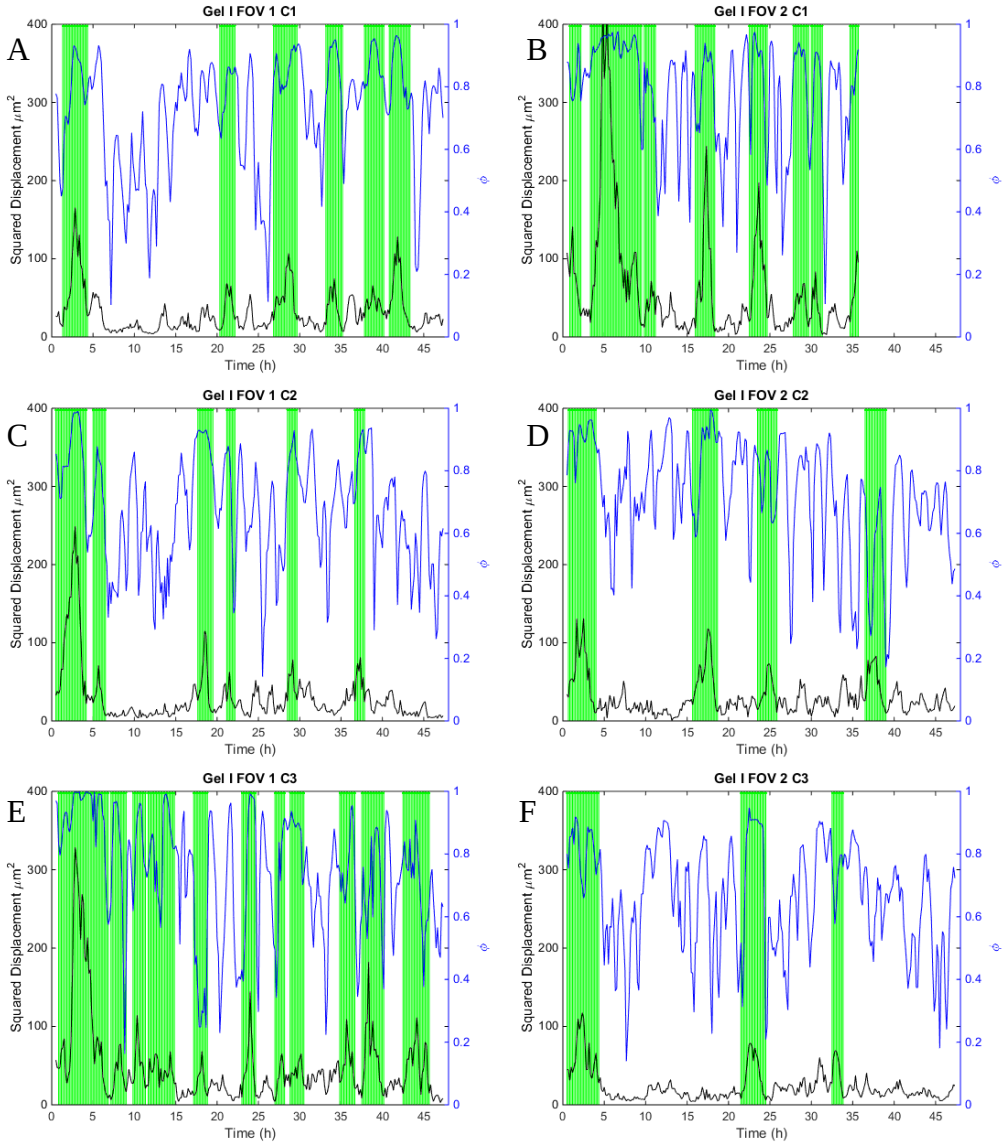

Figure 6-4: Motility events for individual clusters in the same gel

The left vertical axis, correponding to the black lines in plots, mark the SDM. The right verticl axis, corresponding to blue lines in the plots, mark the order parameter (φ). Green shaded regions mark identified motility events. Each plot is for an individual cellular cluster.

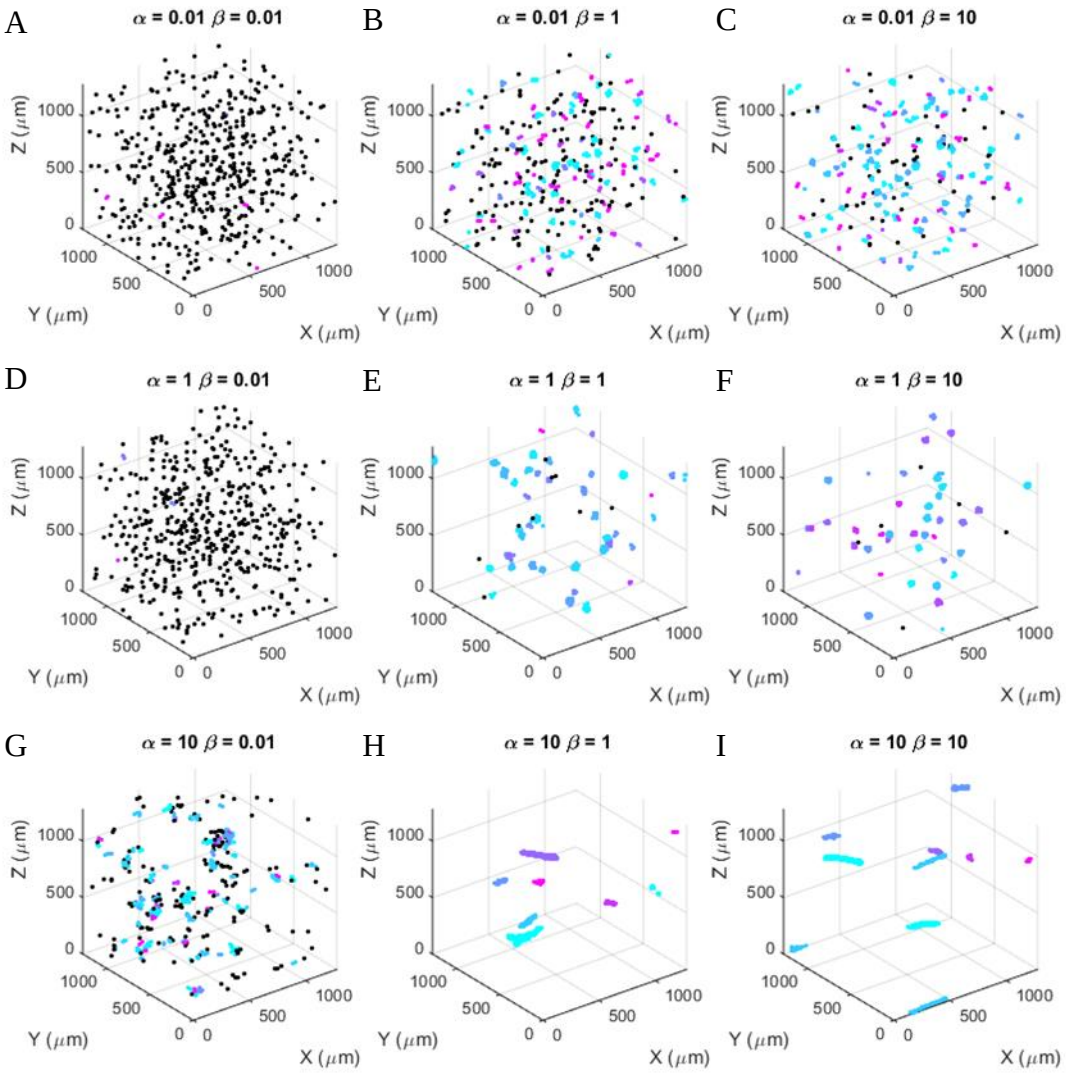

Figure 6-5: Visualization of scaled SPP model for select (α, β) values

Endpoint (t = 20,000 steps) positions for scaled SPP simulations for select (α,β) values. Simulated cells belonging to a single cluster are assigned the same color different from black; black represents single cells.

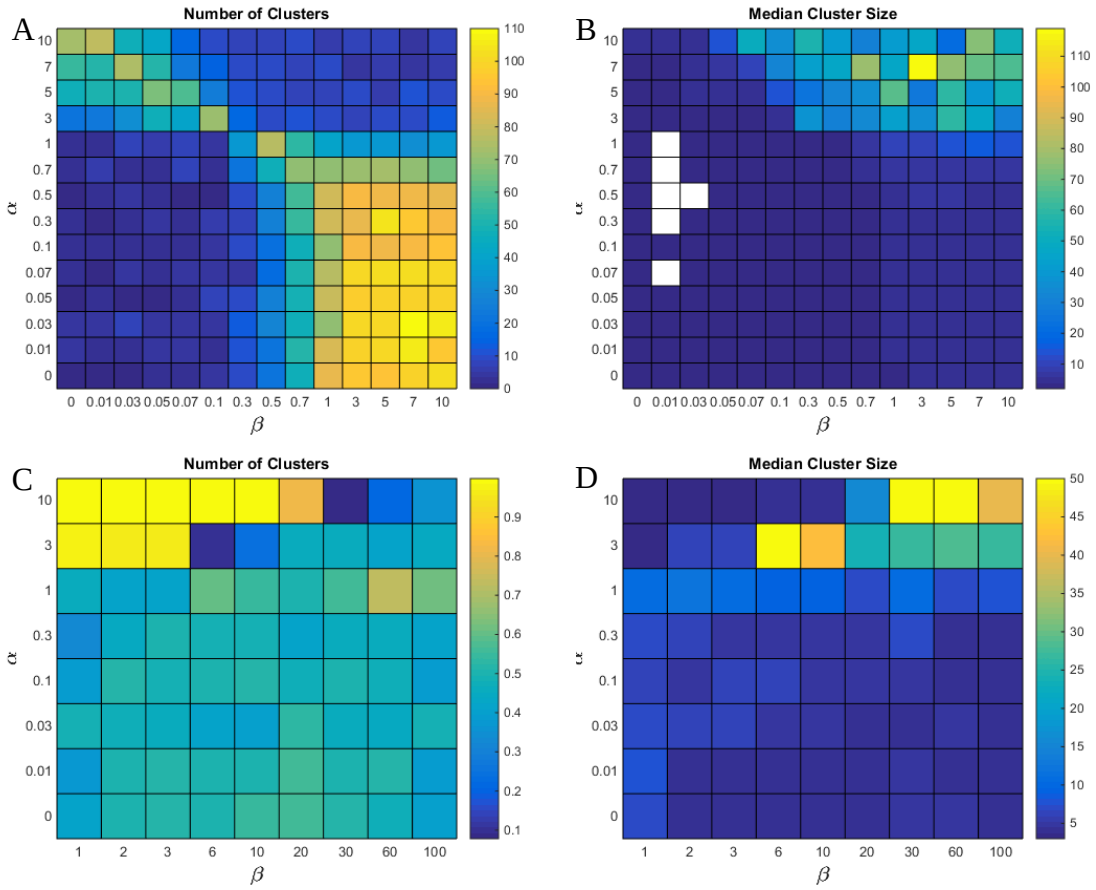

Figure 6-6: Simulated number of clusters and median cluster size

Number of clusters and median cluster size (*i.e.* number of cells) averaged over the last 288 time steps (*i.e.* 48h in real time) for the different conditions defined by $\alpha\beta$-parameter values. Panels A and B display results for scaled SPP model; simulations are run with N = 512 cells. Panels C and D display results for variable speed SPP model; simulations are run with N = 100 cells.

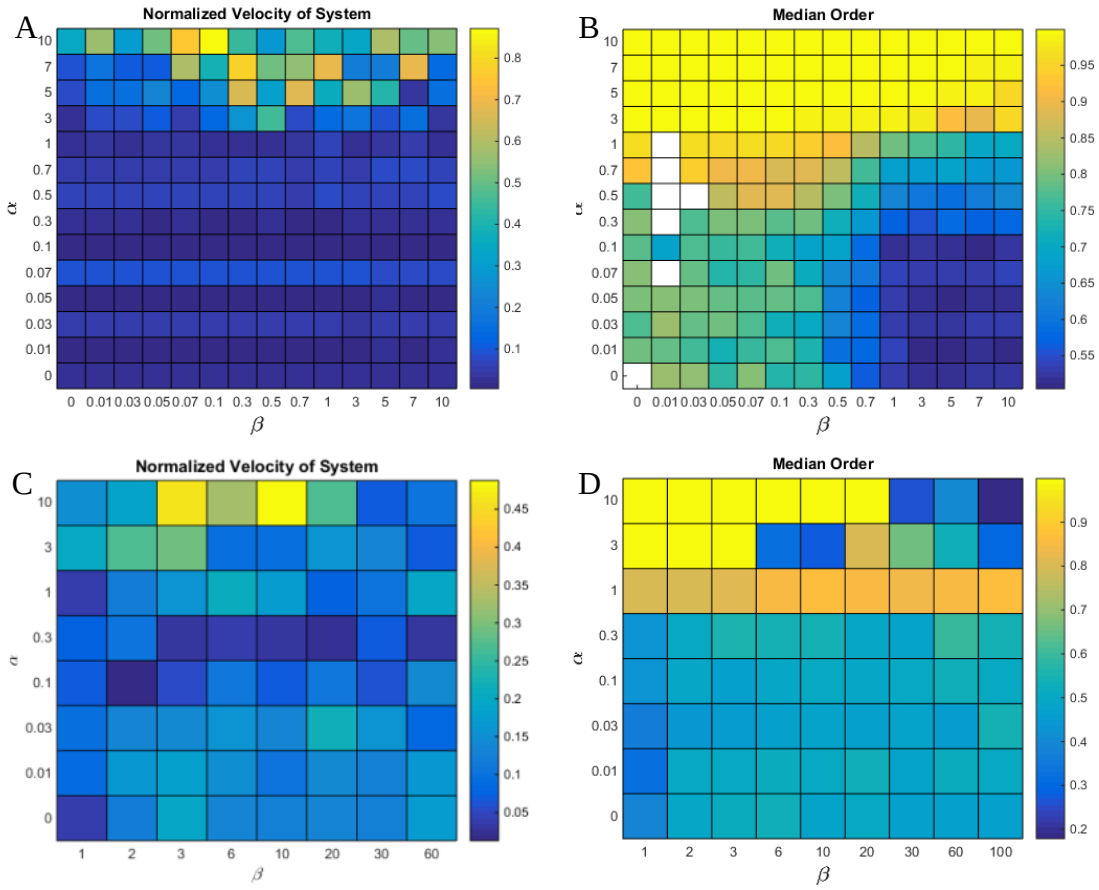

Figure 6-7: Order parameter for SPP models

The order parameter (*i.e.* normalized velocity) is calculated for all cells in the system as well as for each individual cluster per condition defined by $\alpha\beta$-parameter values. The median is reported for all clusters in each condition. Panels A and B display results for scaled SPP model; simulations are run with N = 512 cells. Panels C and D display results for variable speed SPP model; simulations are run with N = 100 cells. Boxes left white occur when clusters either do not exist.

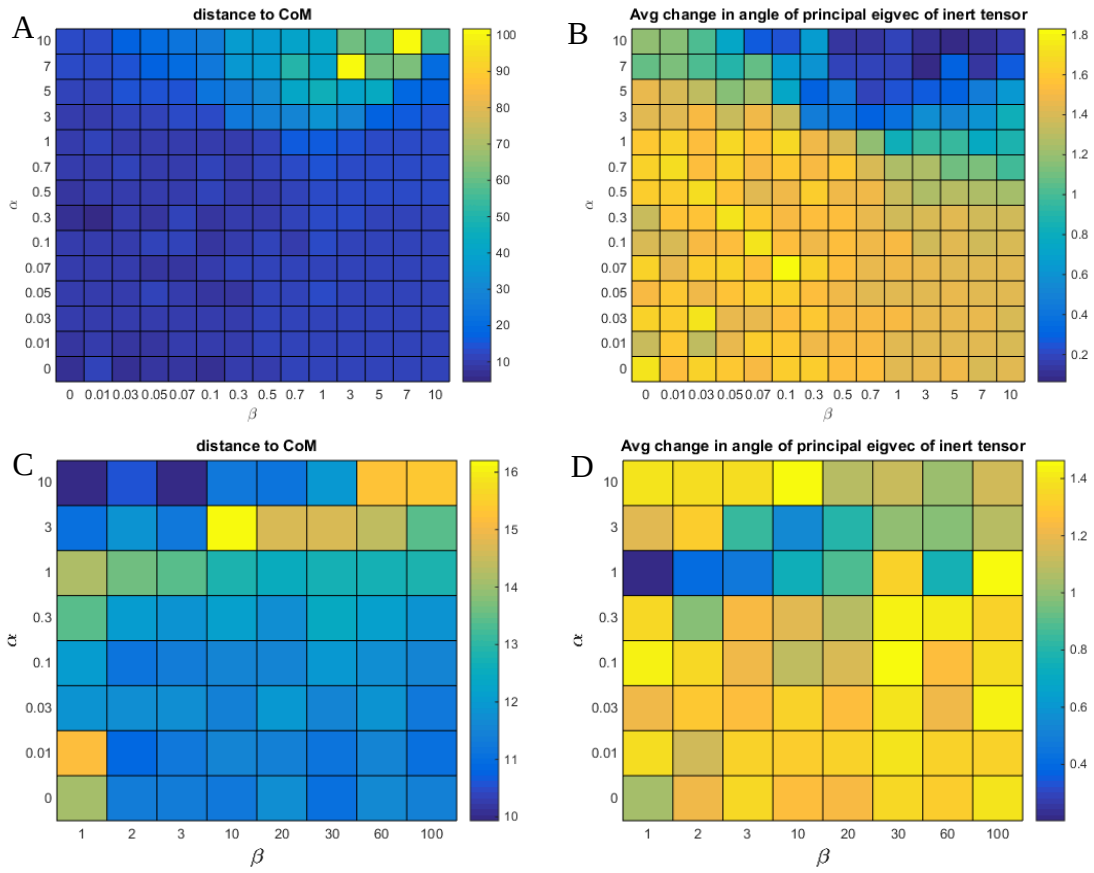

Figure 6-8: Shape and orientation in simulated clusters

Distance of cells to the CoM of each cluster (approximated by average nuclear position) and angle between principal eigenvector of inertia tensor between consecutive time points; both quantities are averaged over the last 288 time steps (*i.e.* 48h in real time) for the different conditions defined by $\alpha\beta$-parameter values. Panels A and B display results for scaled SPP model; simulations are run with N = 512 cells. Panels C and D display results for variable speed SPP model; simulations are run with N = 100 cells.

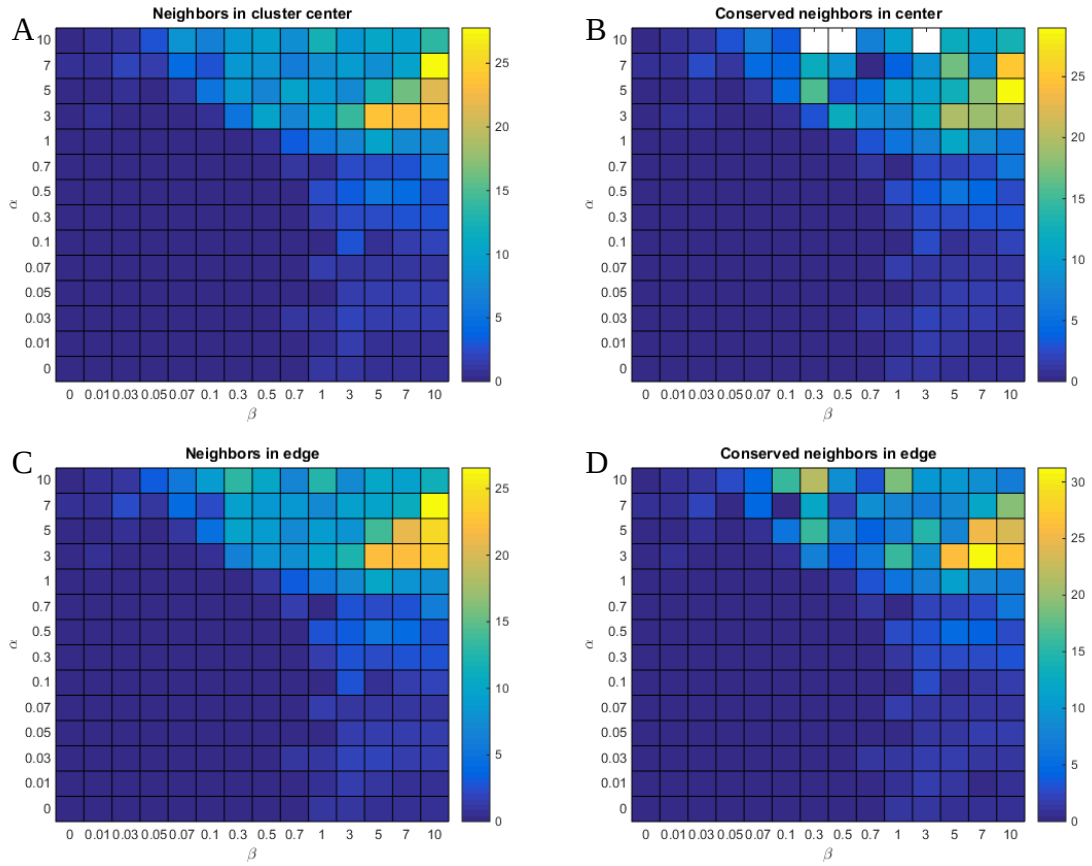

Figure 6-9: Number of neighbors in clusters in scaled SPP model

Results for scaled SPP model; simulations are run with N = 512 cells. Panels A and C display number of neighbors to cell closest (*i.e.* cluster center) and farthest (*i.e.* edge) from the CoM for each cluster, respectively. Panels B and D display number of neighbors of cells closest and farthest from CoM, respectively, conserved between consecutive time points for each cluster. Both quantities are averaged over the last 288 time steps (*i.e.* 48h in real time) for the different conditions defined by $\alpha\beta$-parameter values.

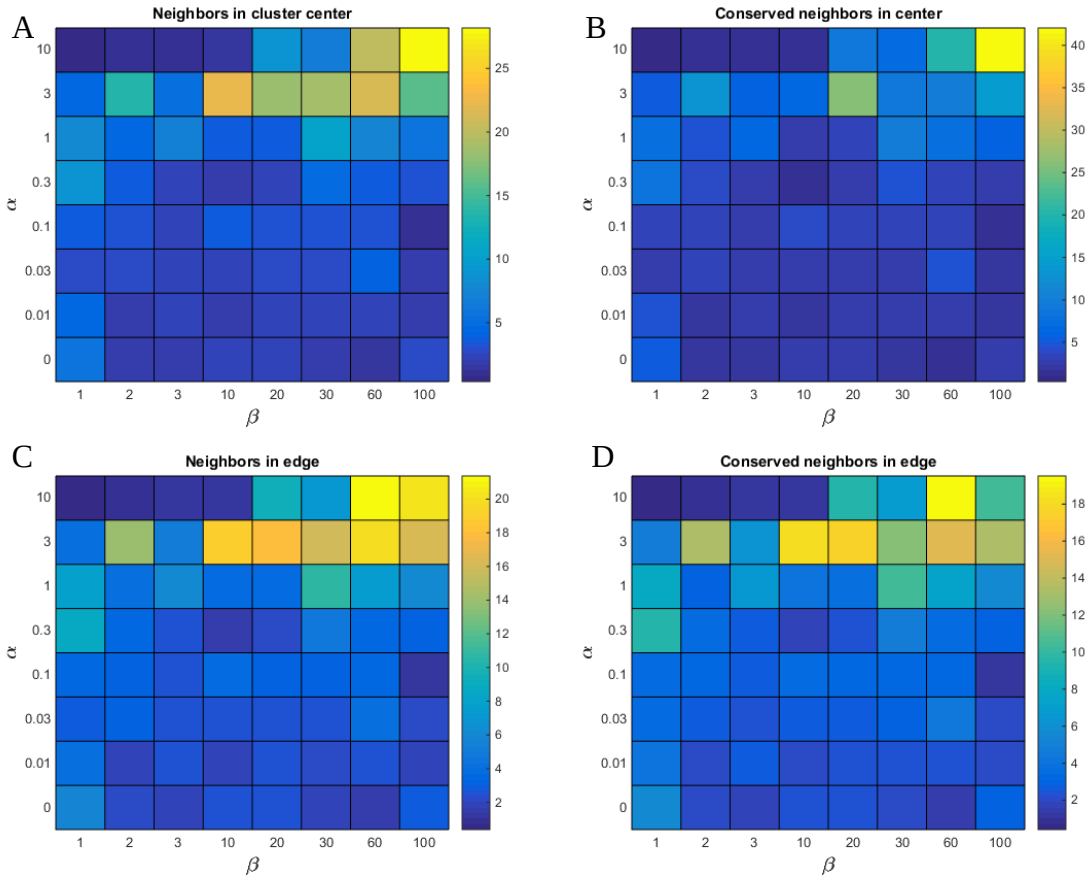

Figure 6-10: Number of neighbors in clusters in variable speed SPP model

Results for variable speed SPP model; simulations are run with N = 100 cells. Panels A and C display number of neighbors to cell closest (*i.e.* cluster center) and farthest (*i.e.* edge) from the CoM for each cluster, respectively. Panels B and D display number of neighbors of cells closest and farthest from CoM, respectively, conserved between consecutive time points for each cluster. Both quantities are averaged over the last 288 time steps (*i.e.* 48h in real time) for the different conditions defined by $\alpha\beta$-parameter values.

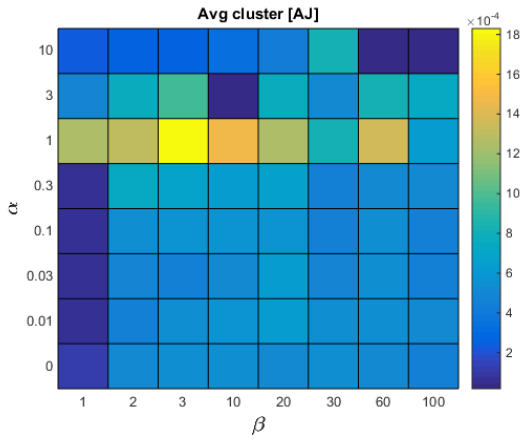

Figure 6-11: Adhesion in simulated clusters

Adherens junction (AJ) expression is averaged for all cells in each cluster formed in each simulation. AJ values are taken at the last time point (*i.e.* t = 48h). In turn, AJ values are averaged for clusters formed in each condition as defined by $\alpha\beta$-parameter values.

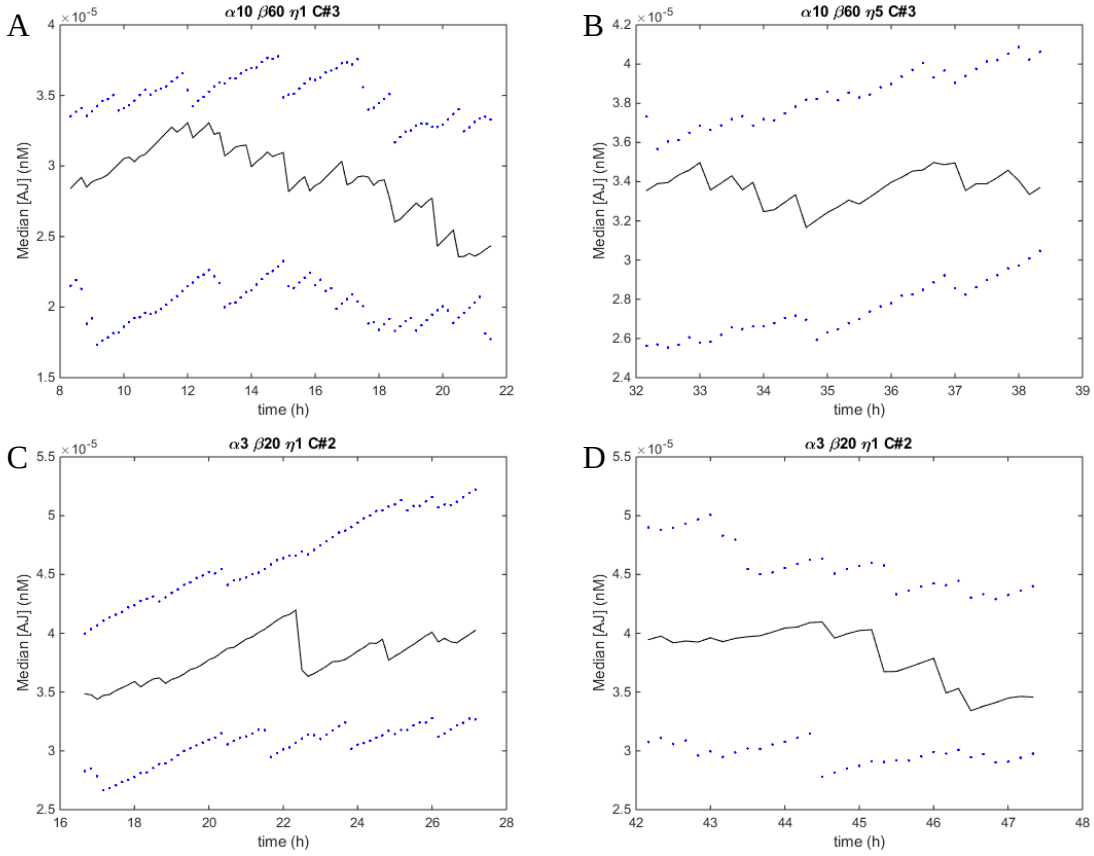

Figure 6-12: Adherens junction expression during motility events

The black lines indicate the median AJ concentration for cells in the cluster for clusters simulated with the variable speed SPP model during motility events. The blue dotted lines indicate the upper and median quantiles of the AJ distribution. Time intervals selected flank motility events with ~2 hours on each side.

CHAPTER 7. Conclusions

7.1 Effect of Cluster Shape and Environment

7.1.1 Scientific Contributions

Regarding the question: *Does the geometry of a cell collective play a role in its interaction with the surroundings?*- This dissertation presents evidence that shape can drastically affect speed due to influence of the environment; therefore, this effect can be overcome by affecting the environment.

The rigid cluster model presented in Chapter 3 explored the effect of shape of a cluster in its velocity and interaction with the ECM, particularly through MMPs. This model does raise questions pertaining to the contributions of physical factors to migration such as: What percentage of the protrusion force is exerted by the leader cell?

Physical constrains of the cluster by the environment affects collective migration. These results demonstrate that the changing shape of a collective must be accounted for to characterize collective migration. This contributes to the field by justifying the use of a more flexible representation of cell collectives, which can be achieved through agent-based modeling.

7.1.2 Future Investigations

In the simulations described in Chapter 3, only ligand concentration, MMP activity, and force modulation (*i.e.* proportionality constants) were altered. However, parameters such as cell number, cluster geometry, number of trailing cells, number of leader cells, and cluster division could also be used to make additional predictions.

Although the effect of cell number and geometry was already more effectively studied with the SPP models in 3D presented in Chapter 6, the work presented may be better utilized to add MMP degradation to the agent based models presented in Chapters 4 or 6.

7.2 Epithelial Disruption and Transitioning into a Cluster

7.2.1 Scientific Contributions

Regarding the question: *What drives the formation of cellular clusters?* - The EMT model presented in Chapter 4 weighed the contributions of regulation of cell-cell adhesion and cell protrusive force in epithelial membrane disruption and cellular invasion. This model demonstrates that the increase in migratory phenotype has a much larger impact on overall layer disruption compared to cell detachment. This can create tumor like cell agglomerations, but clusters can only arise if cell-cell junctions are lost. This model shows how the process of cluster formation is gradual requires increased cell-cell attachment after a detachment phase. Together with the SPP models presented in Chapter 6, this work contributes by suggesting the possibility that a cluster a cluster recruits rather than detach.

This work also contributes to the knowledge about EMT by presenting theoretical evidence that either mutating towards a more migratory phenotype or undergoing the cadherin switch is enough for EMT to occur, but that both occurring together act to amplify the total effect. It also gives reason to ask whether the *cadherin switch* is more fundamental to EMT step in than an acquired aggressive migratory phenotype. This works complements existing *in vitro* and *in vivo* models in developing a quantitative,

rigorous and multi-scale understanding of complex EMT related processes in cancer metastasis, neural crest delamination, and other developmental processes.

7.2.2 Future Investigations

The EMT model motivated inclusion of more complex regulation of cell-cell adhesion in collective models. It is because of the results presented in Chapter 4 that the study of the RCN was done. It is only natural to incorporate the RCN in the EMT model in a way similar to how it was incorporated in an SPP model in Chapter 6.

Even before expansion of the model, it can be used to answer remaining questions. Chapter 4 mostly concerns itself with quantifying single cell behavior in terms of speed and penetration depth into the ECM. The model can be used to study collective behavior in the context of epithelial sheets. Some of the metrics presented in Chapter 6, such as order parameter and conserved neighbor number, can also apply to this *in silico* system.

The EMT model has the potential for using a grid in space as a continuum to track the diffusion of substances in the intercellular space because diffusion of small particles is much faster than cellular motion. Concentrations of extrinsic signals that trigger EMT, such as transforming growth factor β (TGFβ) or members of epidermal growth factor (EGF) family could be included in the model.

Finally, the EMT model is the first model that uses a discrete ECM for simulations of such a large number of cells. Future work on how ECM orientation and organization affects EMT would be valuable. The model can also be expanded to account nearby migrating endothelial cells can communicating through mechanical signals across

a stiff ECM, a phenomenon reported by Reinhart-King et al (187). The novel notion of modeling a discrete ECM can be used to track the effect of cells on each other when coming in contact with the same fiber.

7.3 Dynamic Regulation of Adherens Junctions

7.3.1 Scientific Contributions

Chapter 5 contains the most complete model of Wnt/β-catenin signaling to date. In an effort to capture the complex behavior observed in many different biological studies on epithelial discohesion in cancer and development, the RCN model spans three biological scales: molecular, cellular, and multicellular. The model contributes to the body of knowledge on Wnt/β-catenin signaling by providing a quantitative relation to N-glycosylation. By using a numerical approach, it provides a way to simulate dysregulation of a single process, something rare in a biological system, thus revealing the relative importance of the different processes and consequently the corresponding component pathways. Although the predictions performed by the model are not validated in their entirety, the framework is in place to formulate experiments that can provide conclusive evidence of significant effects downstream of Wnt target genes.

Regarding the question: *Does post-translational modification of junctional proteins have a direct impact on regulation of cell-cell interactions in migrating clusters?*- The RCN model predicts a significant change in intercellular adhesion with inhibition of N-glycosylation. Given the indirect link between adhesion and migration, it cannot be stated that this dissertation conclusively solves this question. This dissertation

does, however, provide a mechanism by which N-glycosylation (*i.e.* a post-translational modification) can affect adhesion and shows evidence of its effect by tracking migration in a cell sheet in populations treated with an inhibitor shown to decrease adhesion.

7.3.2 Future Investigations

In Chapter 5, when exploring the dynamics of the network formed by the multiple pathways, the study focused on adhesion. There are many other molecules in the network that have significant effect on other aspects of cell behavior, such as proliferation. *DPAGT1* expression can be studied not only through an IP assay, but gene expression could be measured through use of fluorescent genetic reporters or real-time polymerase chain reaction (qPCR).

The mathematical model also needs further refinement in terms of parameter estimation. Parameters were estimated based on studies performed on different cell types and organisms. The mathematical model provides a flexible way to estimate parameter values based on measured results on different experimental systems. The results obtained in this dissertation are enough to refine the equilibrium constant used for binding of β-catenin and TCF in MDCK cells specifically.

Experiments on cell sheets looking at speed together with results on network dynamics provided a window into the cross-reactivity of the component pathways. This relation between network dynamics and population behavior can be further explored. In the future, experiments with fewer cells and live fluorescent reporters can be used to test the time evolution of the RCN.

7.4 Cluster Dynamics

7.4.1 Scientific Contributions

This work as whole outlines the path to the single goal of dissecting a cellular cluster and putting it back together in a way that it will still migrate. The task is difficult given the emergent nature of collective behavior. Chapter 6 presents the most complete attempt, in which isolated clusters in *in vitro* are studies and their behavior recreated with a certain degree of success.

Two major contributions of this work to the study of cluster dynamics are: First, the development of consistent methods to study and analyze mammalian clusters *in vitro* consistently (33). Second, formulation of the first variable speed SPP model in 3D.

With the development of an *in vitro* system for the study of cell collectives in 3D, the field can move on to implement techniques that have been successful in 2D such as traction force microscopy and correlation studies.

Regarding the question: *Does regulation of junctional proteins affect specific physical characteristics and migrating dynamics?*- This question was addressed by this dissertation in its comparison of the scaled SPP model and the variable speed SPP model, both presented in Chapter 6. The latter model just differs from the former in its consideration of cell-cell adhesion; the parallel comparisons of internal diffusion, cluster density, and normalized velocity show that just this regulation does affect migrating dynamics.

7.4.2 Future Investigations

The analysis of cluster dynamics was very revealing but incomplete. No temporal studies other than duration of motility events were performed. Sharma *et al.* have looked at time correlation studies beginning to probe the question of leadership within the clusters (33). The computational model can be used to extend these studies to include adhesion and migration.

Integration of the RCN to the SPP model (*i.e.* multiscale model) can also provide additional information beyond AJ expression during cluster migration. By changing specific parameters, physiological and pathological conditions can be modeled. Additionally, the multiscale model can be used to model cell sheets and contribute to the existing body of knowledge about 2D monolayer migration and collective dynamics.

Experimentally, predictions of relation between migration and adhesion will have to be validated. This could be achieved through real-time E-cadherin visualization in clusters. The effect of specific changes in RCN dynamics could also be tackled experimentally through the use of inducible cell lines, transfection, calcium chelators, small molecule inhibitors (*e.g.* ICG-001).

BIBLIOGRAPHY

1. Pan P, Hall EM, Bonner JT (1975) Determination of the active portion of the folic acid molecule in cellular slime mold chemotaxis. *Journal of Bacteriology* 122:185–191.

2. Ewald AJ, Brenot A, Duong M, Chan BS, Werb Z (2008) Collective epithelial migration and cell rearrangements drive mammary branching morphogenesis. *Developmental Cell* 14:570–81.

3. Kegel WK (2000) Direct Observation of Dynamical Heterogeneities in Colloidal Hard-Sphere Suspensions. *Science* 287(5451):290–293.

4. Mori H, Kawasaki K (1962) Theory of Dynamical Behaviors of Ferromagnetic Spins. *Progress of Theoretical Physics* 27:529–570.

5. Friedl P, Gilmour D (2009) Collective cell migration in morphogenesis, regeneration and cancer. *Nature Reviews. Molecular Cell Biology* 10:445–57.

6. THE TOP TEN CAUSES OF DEATH: The 10 leading causes of death by broad income group (2011) *World Health Organization Fact Sheet.* Available at: http://www.who.int/mediacentre/factsheets/fs310_2008.pdf [Accessed August 9, 2015].

7. What is non-small cell lung cancer? (2014) *American Cancer Association*. Available at: http://www.cancer.org/cancer/lungcancer-non-smallcell/detailedguide/non-small-cell-lung-cancer-what-is-non-small-cell-lung-cancer [Accessed September 8, 2015].

8. Garay T et al. (2013) Cell migration or cytokinesis and proliferation? - Revisiting the “go or grow” hypothesis in cancer cells in vitro. *Experimental Cell Research* 319(20):3094–3103.

9. Jamal B et al. (2012) Aberrant amplification of the crosstalk between canonical Wnt signaling and N-glycosylation gene DPAGT1 promotes oral cancer. *Oral Oncology* 48(6):523–529.

10. Macklin P et al. (2009) Multiscale modelling and nonlinear simulation of vascular tumour growth. *Journal of Mathematical Biology* 58:765–98.

11. Wise SM, Lowengrub JS, Frieboes HB, Cristini V (2008) Three-dimensional multispecies nonlinear tumor growth--I Model and numerical method. *Journal of Theoretical Biology* 253:524–43.

12. Grégoire G, Chaté H, Tu Y (2003) Moving and staying together without a leader. *Physica. D, Nonlinear Phenomena* 181:157–170.

13. Ramis-conde I, Drasdo D, Anderson ARA, Chaplain MAJ (2008) Modeling the Influence of the E-Cadherin-b-Catenin Pathway in Cancer Cell Invasion : A Multiscale Approach. *Biophysical Journal* 95:155–165.

14. Harjanto D, Zaman MH (2010) Computational study of proteolysis-driven single cell migration in a three-dimensional matrix. *Annals of Biomedical Engineering* 38:1815–25.

15. Drasdo D, Höhme S (2005) A single-cell-based model of tumor growth in vitro: monolayers and spheroids. *Physical Biology* 2:133–47.

16. Nita-Lazar M et al. (2009) Overexpression of DPAGT1 Leads to Aberrant N-Glycosylation of E-Cadherin and Cellular Discohesion in Oral Cancer. *Cancer Research* 69:5673–5680.

17. Leckband DE, le Duc Q, Wang N, de Rooij J (2011) Mechanotransduction at cadherin-mediated adhesions. *Current Opinion in Cell Biology* 23:523–530.

18. Evans E, Calderwood D (2007) Forces and Bond Dynamics in Cell Adhesion. *Science* 316(5828):1148–1154.

19. Dupont S et al. (2011) Role of YAP/TAZ in mechanotransduction. *Nature* 474:179–83.

20. Serna-Marquez N et al. (2012) Role of LOXs and COX-2 on FAK activation and cell migration induced by linoleic acid in MDA-MB-231 breast cancer cells. *Cellular Oncology (Dordrecht)* 36(1):65–77.

21. Das T et al. (2015) A molecular mechanotransduction pathway regulates collective migration of epithelial cells. *Nature Cell Biology* 17(3):276–287.

22. Berrier AL, Yamada KM (2007) Cell-matrix adhesion. *Journal of Cellular Physiology* 213:565–573.

23. Bosman FT, Stamenkovic I (2003) Functional structure and composition of the extracellular matrix. *Journal of Pathology* 200:423–8.

24. Hynes RO (2009) The extracellular matrix: not just pretty fibrils. *Science* 326:1216–1219.

25. Luo B-H, Carman C V, Springer TA (2007) Structural basis of integrin regulation and signaling. *Annual Review of Immunology* 25:619–47.

26. Geiger B, Bershadsky A, Pankov R, Yamada KM (2001) Transmembrane crosstalk between the extracellular matrix--cytoskeleton crosstalk. *Nature Reviews.*

Molecular Cell Biology 2:793–805.

27. Wolf K et al. (2009) Collagen-based cell migration models in vitro and in vivo. *Seminars in Cell & Developmental Biology* 20:931–41.

28. Friedl P, Wolf K (2010) Plasticity of cell migration: a multiscale tuning model. *Journal of Cell Biology* 188:11–19.

29. Serra-Picamal X et al. (2012) Mechanical waves during tissue expansion. *Nature Physics* 8:628–634.

30. Tambe DT et al. (2011) Collective cell guidance by cooperative intercellular forces. *Nature Materials* 10(6):469–475.

31. Phillips R, Kondev J, Theriot J, Garcia H (2012) *Physical Biology of the Cell* (Garland Science). 2nd Ed.

32. Kolega J (1981) The movement of cell clusters in vitro: morphology and directionality. *Journal of Cell Science* 49:15–32.

33. Sharma Y et al. (2015) Collective Motion of Mammalian Cell Cohorts in 3D. *Integrative Biology* Epub ahead of print.

34. Sixt M (2012) Cell migration: fibroblasts find a new way to get ahead. *Journal of Cell Biology* 197:347–9.

35. Stroka KM et al. (2014) Water permeation drives tumor cell migration in confined microenvironments. *Cell* 157:611–623.

36. Mi H-Y et al. (2015) Electrospinning of unidirectionally and orthogonally aligned thermoplastic polyurethane nanofibers: fiber orientation and cell migration. *Journal of Biomedical Materials Research. Part A* 103:593–603.

37. Lauffenburger DA, Horwitz AF (1996) Cell Migration: A Physically Integrated Molecular Process. *Cell* 84:359–369.

38. Yamada KM, Pankov R, Cukierman E (2003) Dimensions and dynamics in integrin function. *Brazilian Journal of Medical and Biological Research* 36:959–966.

39. Diz-Muñoz A et al. (2010) Control of Directed Cell Migration In Vivo by Membrane-to-Cortex Attachment. *PLoS Biology* 8:e1000544.

40. Fackler OT, Grosse R (2008) Cell motility through plasma membrane blebbing. *Journal of Cell Biology* 181:879–84.

41. Even-Ram S, Yamada KM (2005) Cell migration in 3D matrix. *Current Opinion in Cell Biology* 17:524–32.

42. Harrison CA, Dalley AJ, Neil SMAC (2005) A simple in vitro model for investigating epithelial / mesenchymal interactions : keratinocyte inhibition of fibroblast proliferation and fibronectin synthesis. *Wound Repair and Regeneration* 13(6):543–550.

43. Curran S, Murray G. (2000) Matrix metalloproteinases: molecular aspects of their roles in tumor invasion and metastasis. *European Journal of Cancer* 36:1621–1630.

44. Noël A, Jost M, Maquoi E (2008) Matrix metalloproteinases at cancer tumor-host interface. *Seminars in Cell & Developmental Biology* 19:52–60.

45. Friedl P et al. (1997) Migration of Highly Aggressive MV3 Melanoma Cells in 3-Dimensional Collagen Lattices Results in Local Matrix Reorganization and Shedding of {alpha}2 and {beta}1 Integrins and CD44. *Cancer Research* 57:2061–2070.

46. Artym V V., Zhang Y, Seillier-Moiseiwitsch F, Yamada KM, Mueller SC (2006) Dynamic Interactions of Cortactin and Membrane Type 1 Matrix Metalloproteinase at Invadopodia: Defining the Stages of Invadopodia Formation and Function. *Cancer Research* 66:3034–3043.

47. Sloane BF, Sameni M, Podgorski I, Cavallo-Medved D, Moin K (2006) Functional imaging of tumor proteolysis. *Annual Review of Pharmacology and Toxicology* 46:301–15.

48. Dejana E (2004) Endothelial cell-cell junctions: happy together. *Nature Reviews. Molecular Cell Biology* 5:261–70.

49. Garrod D, Chidgey M (2008) Desmosome structure, composition and function. *Biochimica et Biophysica Acta* 1778:572–87.

50. Vitorino P, Meyer T (2008) Modular control of endothelial sheet migration. *Genes and Development* 22:3268–81.

51. Pertz O et al. (1999) A new crystal structure, Ca2+ dependence and mutational analysis reveal molecular details of E-cadherin homoassociation. *EMBO Journal* 18:1738–47.

52. Yap a S, Brieher WM, Gumbiner BM (1997) Molecular and functional analysis of cadherin-based adherens junctions. *Annual Review of Cell and Developmental Biology* 13:119–46.

53. Gumbiner BM (1996) Cell Adhesion: The Molecular Basis of Tissue Architecture and Morphogenesis. *Cell* 84:345–357.

54. Varelas X, Bouchie MP, Kukuruzinska MA (2014) Protein N-glycosylation in oral cancer : dysregulated cellular networks among DPAGT1 , E-cadherin adhesion and canonical Wnt signaling. *Glycobiology* 24:579–591.

55. Le TL, Yap a S, Stow JL (1999) Recycling of E-cadherin: a potential mechanism for regulating cadherin dynamics. *Journal of Cell Biology* 146:219–32.

56. Riggleman B, Schedl P, Wieschaus E (1990) Spatial expression of the Drosophila segment polarity gene armadillo is posttranscriptionally regulated by wingless. *Cell* 63:549–60.

57. Korinek V et al. (1998) Depletion of epithelial stem-cell compartments in the small intestine of mice lacking Tcf-4. *Nature Genetics* 19:379–83.

58. Funayama N, Fagotto F, McCrea P, Gumbiner BM (1995) Embryonic axis induction by the armadillo repeat domain of beta-catenin: evidence for intracellular signaling. *Journal of Cell Biology* 128:959–68.

59. van Es JH et al. (2005) Notch/gamma-secretase inhibition turns proliferative cells in intestinal crypts and adenomas into goblet cells. *Nature* 435:959–63.

60. Sussman DJ et al. (1994) Isolation and characterization of a mouse homolog of the Drosophila segment polarity gene dishevelled. *Developmental Biology* 166:73–86.

61. Clevers H, Nusse R (2012) Wnt/β-catenin signaling and disease. *Cell* 149:1192–205.

62. Langer MD, Guo H, Shashikanth N, Pierce JM, Leckband DE (2012) N-glycosylation alters cadherin-mediated intercellular binding kinetics. *Journal of Cell Science* 125(10):2478–2485.

63. Pinho SS et al. (2011) Modulation of E-cadherin function and dysfunction by N-glycosylation. *Cellular and Molecular Life Sciences* 68:1011–20.

64. Aebi M (2013) N-linked protein glycosylation in the ER. *Biochimica et Biophysica Acta* 1833:2430–7.

65. Dennis JW, Granovsky M, Warren CE (1999) Protein glycosylation in development and disease. *Bioessays* 21:412–21.

66. Kornfeld R, Kornfeld S (1985) Assembly of asparagine-linked oligosaccharides. *Annual Review of Biochemistry* 54:631–664.

67. Helenius A (2001) Intracellular Functions of N-Linked Glycans. *Science* 291(5512):2364–2369.

68. Pinho SS et al. (2009) Role of E-cadherin N-glycosylation profile in a mammary tumor model. *Biochemical and Biophysical Research Communications* 379:1091–

1096.

69. Mendelsohn RD, Helmerhorst EJ, Cipollo JF, Kukuruzinska MA (2005) A hypomorphic allele of the first N-glycosylation gene, ALG7, causes mitochondrial defects in yeast. *Biochimica et Biophysica Acta* 1723:33–44.

70. Nita-Lazar M, Rebustini I, Walker J, Kukuruzinska MA (2010) Hypoglycosylated E-cadherin promotes the assembly of tight junctions through the recruitment of PP2A to adherens junctions. *Experimental Cell Research* 316:1871–84.

71. Bryant DM, Stow JL (2004) The ins and outs of E-cadherin trafficking. *Trends in Cell Biology* 14:427–34.

72. D. Hanahan RW (2000) Hallmarks of cancer. *Cell* 100:57–70.

73. Gupta GP, Massagué J (2006) Cancer metastasis: building a framework. *Cell* 127:679–95.

74. Langley RR, Fidler IJ (2007) Tumor cell-organ microenvironment interactions in the pathogenesis of cancer metastasis. *Endocrine Reviews* 28:297–321.

75. Skobe M, Fusenig NE (1998) Tumorigenic conversion of immortal human keratinocytes through stromal cell activation. *Proceedings of the National Academy of Sciences of the United States of America* 95:1050–5.

76. Condeelis J, Segall JE (2003) Intravital imaging of cell movement in tumours. *Nature Reviews. Cancer* 3:921–30.

77. Polacheck WJ, Charest JL, Kamm RD (2011) Interstitial flow influences direction of tumor cell migration through competing mechanisms. *Proceedings of the National Academy of Sciences of the United States of America* 108:11115–20.

78. Chung S, Sudo R, Vickerman V, Zervantonakis IK, Kamm RD (2010) Microfluidic Platforms for Studies of Angiogenesis, Cell Migration, and Cell–Cell Interactions. *Annals of Biomedical Engineering* 38:1164–1177.

79. Singh T, Katiyar SK (2013) Honokiol Inhibits Non-Small Cell Lung Cancer Cell Migration by Targeting PGE2-Mediated Activation of β-Catenin Signaling. *PLoS One* 8:e60749.

80. Tozluoğlu M et al. (2013) Matrix geometry determines optimal cancer cell migration strategy and modulates response to interventions. *Nature Cell Biology* 15:751–62.

81. Zhu Y et al. (2012) Dvl2-Dependent Activation of Daam1 and RhoA Regulates Wnt5a-Induced Breast Cancer Cell Migration. *PLoS One* 7:e37823.

82. Geiger T, Sabanay H, Kravchenko-balasha N, Geiger B, Levitzki A (2008) Anomalous features of EMT during keratinocyte transformation. *PLoS One* 3(2):e1574.

83. Grünert S, Jechlinger M, Beug H (2003) Diverse cellular and molecular mechanisms contribute to epithelial plasticity and metastasis. *Nature Reviews. Molecular Cell Biology* 4:657–65.

84. Yilmaz M, Christofori G (2009) EMT, the cytoskeleton, and cancer cell invasion. *Cancer Metastasis Reviews* 28:15–33.

85. Theveneau E, Mayor R (2012) Neural crest delamination and migration: from epithelium-to-mesenchyme transition to collective cell migration. *Developmental Biology* 366:34–54.

86. Brabletz T et al. (2005) Invasion and metastasis in colorectal cancer: epithelial-mesenchymal transition, mesenchymal-epithelial transition, stem cells and beta-catenin. *Cells, Tissues, Organs* 179:56–65.

87. Sarrió D et al. (2008) Epithelial-mesenchymal transition in breast cancer relates to the basal-like phenotype. *Cancer Research* 68:989–97.

88. Sengupta PK, Bouchie MP, Kukuruzinska M a (2010) N-glycosylation gene DPAGT1 is a target of the Wnt/beta-catenin signaling pathway. *Journal of Biological Chemistry* 285:31164–73.

89. Schwarz US, Bischofs IB (2005) Physical determinants of cell organization in soft media. *Medical Engineering & Physics* 27:763–72.

90. Lo CM, Wang HB, Dembo M, Wang YL (2000) Cell movement is guided by the rigidity of the substrate. *Biophysical Journal* 79:144–52.

91. Bischofs IB, Schwarz US (2003) Cell organization in soft media due to active mechanosensing. *Proceedings of the National Academy of Sciences of the United States of America* 100:9274–9.

92. Sanz-Herrera JA, Moreo P, García-Aznar JM, Doblaré M (2009) On the effect of substrate curvature on cell mechanics. *Biomaterials* 30:6674–86.

93. Carter S (1967) Haptotaxis and the mechanism of cell motility. *Nature* 213:256–260.

94. Baker EL, Zaman MH (2010) The biomechanical integrin. *Journal of Biomechanics* 43:38–44.

95. Zaman MH, Kamm RD, Matsudaira P, Lauffenburger DA (2005) Computational model for cell migration in three-dimensional matrices. *Biophysical Journal*

89:1389–97.

96. DiMilla PA, Barbee K, Lauffenburger DA (1991) Mathematical model for the effects of adhesion and mechanics on cell migration speed. *Biophysical Journal* 60:15–37.

97. Lepzelter D, Bates O, Zaman M (2012) Integrin clustering in two and three dimensions. *Langmuir* 28:5379–86.

98. Kim T, Hwang W, Lee H, Kamm RD (2009) Computational analysis of viscoelastic properties of crosslinked actin networks. *PLoS Computational Biology* 5:e1000439.

99. Zaman MH, Kamm RD, Matsudaira P, Lauffenburger DA (2005) Computational model for cell migration in three-dimensional matrices. *Biophysical Journal* 89:1389–97.

100. Dawes AT, Edelstein-Keshet L (2007) Phosphoinositides and Rho proteins spatially regulate actin polymerization to initiate and maintain directed movement in a one-dimensional model of a motile cell. *Biophysical Journal* 92:744–68.

101. Schülter DK, Ramis-conde I, Chaplain MAJ (2012) Computational modeling of single cell migration: The leading role of extracellular matrix fibers. *Biophysical Journal* 103:1141–1151.

102. Scianna M, Preziosi L (2012) Modeling the influence of nucleus elasticity on cell invasion in fiber networks and microchannels. *Journal of Theoretical Biology* 317:394–406.

103. Szabó A, Merks RMH (2013) Cellular potts modeling of tumor growth, tumor invasion, and tumor evolution. *Frontiers in Oncology* 3:87.

104. Gerisch A, Chaplain MAJ (2008) Mathematical modelling of cancer cell invasion of tissue: local and non-local models and the effect of adhesion. *Journal of Theoretical Biology* 250:684–704.

105. Painter KJ (2008) Modelling cell migration strategies in the extracellular matrix. *Journal of Mathematical Biology* 58:511–543.

106. Jiao Y, Torquato S (2011) Emergent behaviors from a cellular automaton model for invasive tumor growth in heterogeneous microenvironments. *PLoS Computational Biology* 7:e1002314.

107. Tanaka S, Sichau D, Iber D (2015) LBIBCell: a cell-based simulation environment for morphogenetic problems. *Bioinformatics* 31:2340–2347.

108. Schaller G (2004) Kinetic and dynamic Delaunay tetrahedralizations in three dimensions. *Computer Physics Communications* 162:9–23.

109. Kabla AJ Collective Cell Migration : Leadership , Invasion and Segregation.

110. Turner S, Sherratt JA (2002) Intercellular adhesion and cancer invasion: a discrete simulation using the extended Potts model. *Journal of Theoretical Biology* 216:85–100.

111. Gatenby RA (1995) Models of tumor-host interaction as competing populations: implications for tumor biology and treatment. *Journal of Theoretical Biology* 176:447–55.

112. Bearer EL et al. (2009) Multiparameter computational modeling of tumor invasion. *Cancer Research* 69:4493–501.

113. Trucu D, Lin P, Chaplain MAJ, Wang Y (2013) A multiscale moving boundary model arising in cancer invasion. *Multiscale Modeling & Simulation* 11:309–335.

114. Anderson AR a (2005) A hybrid mathematical model of solid tumour invasion: The importance of cell adhesion. *Mathematical Medicine and Biology* 22:163–186.

115. Jeon J, Quaranta V, Cummings PT (2010) An off-lattice hybrid discrete-continuum model of tumor growth and invasion. *Biophysical Journal* 98:37–47.

116. Kabla AJ (2012) Collective cell migration: leadership, invasion and segregation. *Journal of the Royal Society, Interface* 9:3268–3278.

117. Tanner K, Mori H, Mroue R, Bruni-Cardoso A, Bissell MJ (2012) Coherent angular motion in the establishment of multicellular architecture of glandular tissues. *Proceedings of the National Academy of Sciences of the United States of America* 109:1973–8.

118. Doxzen K et al. (2013) Guidance of collective cell migration by substrate geometry. *Integrative Biology* 5:1026–35.

119. Czirók A, Barabási A-L, Vicsek T (1999) Collective Motion of Self-Propelled Particles: Kinetic Phase Transition in One Dimension. *Physical Review Letters* 82:209–212.

120. Mishra S, Tunstrøm K, Couzin ID, Huepe C (2012) Collective dynamics of self-propelled particles with variable speed. *Physical Review. E, Statistical, Nonlinear, and Soft Matter Physics* 86:011901.

121. Vicsek T, Czirók A, Ben-Jacob E, Cohen I, Shochet O (1995) Novel Type of Phase Transition in a System of Self-Driven Particles. *Physical Review Letters* 75:1226–1229.

122. Szabó B et al. (2006) Phase transition in the collective migration of tissue cells: Experiment and model. *Physical Review. E, Statistical, Nonlinear, and Soft Matter Physics* 74:061908.

123. Couzin ID, Krause J, James R, Ruxton GD, Franks NR (2002) Collective Memory and Spatial Sorting in Animal Groups. *Journal of Theoretical Biology* 218:1–11.

124. Belmonte JM, Thomas GL, Brunnet LG, de Almeida RMC, Chaté H (2008) Self-Propelled Particle Model for Cell-Sorting Phenomena. *Physical Review Letters* 100:248702.

125. Friedl P et al. (1995) Migration of coordinated cell clusters in mesenchymal and epithelial cancer explants in vitro advances in brief migration of coordinated cell clusters in mesenchymal and epithelial cancer in vitro. *Cancer Research* 55(20): 4557–4560.

126. Ilina O, Friedl P (2009) Mechanisms of collective cell migration at a glance. *Journal of Cell Science* 122:3203–3208.

127. Cukierman E, Pankov R, Stevens DR, Yamada KM (2001) Taking cell-matrix adhesions to the third dimension. *Science* 294(5547):1708–1712.

128. Brown A (1982) Neutrophil granulocytes: adhesion and locomotion on collagen substrata and in collagen matrices. *Journal of Cell Science* 58:455–467.

129. Friedl P, Wolf K (2003) Tumour-cell invasion and migration: diversity and escape mechanisms. *Nature Reviews. Cancer* 3:362–74.

130. Geisbrecht ER, Montell DJ (2002) Myosin VI is required for E-cadherin-mediated border cell migration. *Nature Cell Biology* 4:616–20.

131. Farooqui R, Fenteany G (2005) Multiple rows of cells behind an epithelial wound edge extend cryptic lamellipodia to collectively drive cell-sheet movement. *Journal of Cell Science* 118:51–63.

132. Sabeh F et al. (2004) Tumor cell traffic through the extracellular matrix is controlled by the membrane-anchored collagenase MT1-MMP. *Journal of Cell Biology* 167:769–81.

133. Friedl P, Wolf K (2008) Tube travel: the role of proteases in individual and collective cancer cell invasion. *Cancer Research* 68:7247–9.

134. Maruthamuthu V, Sabass B, Schwarz US, Gardel ML (2011) Cell-ECM traction force modulates endogenous tension at cell-cell contacts. *Proceedings of the National Academy of Sciences of the United States of America* 108:4708–13.

135. Legant WR et al. (2010) Measurement of mechanical tractions exerted by cells in three-dimensional matrices. *Nature Methods* 7:969–971.

136. Polio SR, Rothenberg KE, Stamenović D, Smith ML (2012) A micropatterning and image processing approach to simplify measurement of cellular traction forces. *Acta Biomaterialia* 8:82–88.

137. Gjorevski N, S. Piotrowski A, Varner VD, Nelson CM (2015) Dynamic tensile forces drive collective cell migration through three-dimensional extracellular matrices. *Scientific Reports* 5:11458.

138. Theveneau E, Mayor R (2012) Cadherins in collective cell migration of mesenchymal cells. *Current Opinion in Cell Biology* 24(5):677–684.

139. Hirohashi S, Kanai Y (2003) Cell adhesion system and human cancer morphogenesis. *Cancer Science* 94:575–581.

140. Geiger T, Sabanay H, Kravchenko-Balasha N, Geiger B, Levitzki A (2008) Anomalous features of EMT during keratinocyte transformation. *PLoS One* 3:e1574.

141. Wildenberg GA et al. (2006) p120-catenin and p190RhoGAP regulate cell-cell adhesion by coordinating antagonism between Rac and Rho. *Cell* 127:1027–39.

142. Vargas D a., Bates O, Zaman MH (2013) Computational model to probe cellular mechanics during epithelial- mesenchymal transition. *Cells, Tissues, Organs* 197:435–444.

143. Schaller G, Meyer-Hermann M (2005) Multicellular tumor spheroid in an off-lattice Voronoi-Delaunay cell model. *Physical Review. E, Statistical, Nonlinear, and Soft Matter Physics* 71(5 Pt 1):051910.

144. Harjanto D, Maffei JS, Zaman MH (2011) Quantitative Analysis of the Effect of Cancer Invasiveness and Collagen Concentration on 3D Matrix Remodeling. *PLoS One* 6:e24891.

145. Phillips RJ, Deen WM, Brady JF (1989) Hindered transport of spherical macromolecules in fibrous membranes and gels. *AIChE Journal* 35:1761–1769.

146. Zervantonakis IK, Kothapalli CR, Chung S, Sudo R, Kamm RD (2011) Microfluidic devices for studying heterotypic cell-cell interactions and tissue specimen cultures under controlled microenvironments. *Biomicrofluidics* 5:13406.

147. Krishnan R et al. (2012) Fluidization, resolidification, and reorientation of the endothelial cell in response to slow tidal stretches. *American Journal of Physiology. Cell Physiology* 303:C368–375.

148. Cavalcante FSA et al. (2005) Mechanical interactions between collagen and proteoglycans: implications for the stability of lung tissue. *Journal of Applied Physiology* 98:672–679.

149. Bordeleau F, Tang LN, Reinhart-King C a (2013) Topographical guidance of 3D tumor cell migration at an interface of collagen densities. *Physical Biology* 10:065004.

150. Haslehurst AM et al. (2012) EMT transcription factors snail and slug directly contribute to cisplatin resistance in ovarian cancer. *BMC Cancer* 12:91.

151. Galle J, Loeffler M, Drasdo D (2005) Modeling the effect of deregulated proliferation and apoptosis on the growth dynamics of epithelial cell populations in vitro. *Biophysical Journal* 88:62–75.

152. Masamizu Y et al. (2006) Real-time imaging of the somite segmentation clock: revelation of unstable oscillators in the individual presomitic mesoderm cells. *Proceedings of the National Academy of Sciences of the United States of America* 103:1313–1318.

153. Sengupta PK, Bouchie MP, Nita-Lazar M, Yang H-Y, Kukuruzinska M a (2013) Coordinate regulation of N-glycosylation gene DPAGT1, canonical Wnt signaling and E-cadherin adhesion. *Journal of Cell Science* 126:484–96.

154. Lee E, Salic A, Krüger R, Heinrich R, Kirschner MW (2003) The roles of APC and Axin derived from experimental and theoretical analysis of the Wnt pathway. *PLoS Biology* 1:E10.

155. Benary U, Kofahl B, Hecht A, Wolf J (2013) Modeling Wnt/β-Catenin Target Gene Expression in APC and Wnt Gradients Under Wild Type and Mutant Conditions. *Frontiers in Physiology* 4:21.

156. Chen W et al. (2003) Dishevelled 2 recruits beta-arrestin 2 to mediate Wnt5A-stimulated endocytosis of Frizzled 4. *Science* 301:1391–1394.

157. Aberle H, Bauer a, Stappert J, Kispert a, Kemler R (1997) Beta-Catenin Is a Target for the Ubiquitin-Proteasome Pathway. *EMBO Journal* 16:3797–804.

158. Chen Y-T (1999) Coupling Assembly of the E-Cadherin/beta -Catenin Complex to Efficient Endoplasmic Reticulum Exit and Basal-lateral Membrane Targeting of E-Cadherin in Polarized MDCK Cells. *Journal of Cell Biology* 144:687–699.

159. Kam Y, Quaranta V (2009) Cadherin-bound beta-catenin feeds into the Wnt pathway upon adherens junctions dissociation: evidence for an intersection between beta-catenin pools. *PLoS One* 4:e4580.

160. Salic a, Lee E, Mayer L, Kirschner MW (2000) Control of beta-catenin stability: reconstitution of the cytoplasmic steps of the wnt pathway in Xenopus egg extracts. *Molecular Cell* 5:523–532.

161. Shore EM, Nelson WJ (1991) Biosynthesis of the Cell Adhesion Molecule Uvomorulin (E-Cadherin) in MAdin-Darby Canine Kidney Epithelial Cells. *Journal of Biological Chemistry* 266:19672–19680.

162. Goentoro L, Kirschner MW (2009) Evidence that fold-change, and not absolute level, of beta-catenin dictates Wnt signaling. *Molecular Cell* 36:872–884.

163. Zhang Y, Rundell, A (2006) Comparative study of parameter sensitivity analyses of the TCR-activated Erk-MAPK signalling pathway. *Systems Biology* 153:201–211.

164. Emami KH et al. (2004) A small molecule inhibitor of beta-catenin/CREB-binding protein transcription [corrected]. *Proceedings of the National Academy of Sciences of the United States of America* 101:12682–12687.

165. Rasband WS Image J. US National Institutes of Health, Bethesda, MD, USA.

166. Tseng Q et al. (2012) Spatial organization of the extracellular matrix regulates cell-cell junction positioning. *Proceedings of the National Academy of Sciences of the United States of America* 109:1506–1511.

167. Liwosz A, Lei T, Kukuruzinska MA (2006) N-glycosylation affects the molecular organization and stability of E-cadherin junctions. *Journal of Biological Chemistry* 281:23138–23149.

168. Takahashi-Yanaga F, Kahn M (2010) Targeting Wnt signaling: can we safely eradicate cancer stem cells? *Clinical Cancer Research* 16:3153–3162.

169. Ng MR, Besser A, Danuser G, Brugge JS (2012) Substrate stiffness regulates cadherin-dependent collective migration through myosin-II contractility. *Journal of Cell Biology* 199:545–563.

170. Brabletz T et al. (2001) Variable beta-catenin expression in colorectal cancers indicates tumor progression driven by the tumor environment. *Proceedings of the National Academy of Sciences of the United States of America* 98:10356–10361.

171. Näthke IS (2004) The adenomatous polyposis coli protein: the Achilles heel of the gut epithelium. *Annual Review of Cell and Developmental Biology* 20:337–366.

172. Hardy RG, Meltzer SJ, Jankowski JA (2000) ABC of colorectal cancer. Molecular basis for risk factors. *BMJ: British Medical Journal* 321(7265):886–889.

173. Satoh S et al. (2000) AXIN1 mutations in hepatocellular carcinomas, and growth suppression in cancer cells by virus-mediated transfer of AXIN1. *Nature Genetics* 24:245–250.

174. Giles RH, van Es JH, Clevers H (2003) Caught up in a Wnt storm: Wnt signaling in cancer. *Biochimica et Biophysica Acta - Reviews on Cancer* 1653:1–24.

175. Miyashita K et al. (2009) An Emerging Strategy for Cancer Treatment Targeting Aberrant Glycogen Synthase Kinase 3β. *Anti-cancer Agents in Medicinal Chemistry* 9:1114–1122.

176. Biechele TL, Moon RT (2008) Assaying beta-catenin/TCF transcription with beta-catenin/TCF transcription-based reporter constructs. *Methods in Molecular Biology* 468:99–110.

177. Wawrzak D et al. (2007) Wnt3a binds to several sFRPs in the nanomolar range. *Biochemical and Biophysical Research Communications* 357:1119–1123.

178. McCrea PD, Gumbiner BM (1991) Purification of a 92-kDa cytoplasmic protein tightly associated with the cell-cell adhesion molecule E-cadherin (uvomorulin). Characterization and extractability of the protein complex from the cell cytostructure. *Journal of Biological Chemistry* 266:4514–4520.

179. Cavagna A, Duarte Queirós SM, Giardina I, Stefanini F, Viale M (2013) Diffusion of individual birds in starling flocks. *Proceedings. Biological Sciences / The Royal Society* 280:20122484.

180. Attanasi A et al. (2014) Information transfer and behavioural inertia in starling flocks. *Nature Physics* 10:615–698.

181. Yates CA, Baker RE, Erban R, Maini PK (2010) Refining self-propelled particle models for collective behaviour. *Canadian Applied Mathematics Quarterly* 18(3):299–350.

182. Edelstein AD et al. (2014) Advanced methods of microscope control using μManager software. *Journal of Biological Methods* 1:10.

183. Leong WS et al. (2010) Thickness sensing of hMSCs on collagen gel directs stem cell fate. *Biochemical and Biophysical Research Communications* 401:287–92.

184. Gao Y, Kilfoil ML (2009) Accurate detection and complete tracking of large populations of features in three dimensions. *Optics Express* 17:4685.

185. Pelletier V, Gal N, Fournier P, Kilfoil ML (2009) Microrheology of Microtubule Solutions and Actin-Microtubule Composite Networks. *Physical Review Letters* 102:188303.

186. Vicsek T, Zafeiris A (2012) Collective motion. *Physics Reports* 517:71–140.

187. Reinhart-King CA, Dembo M, Hammer DA (2008) Cell-cell mechanical communication through compliant substrates. *Biophysical Journal* 95:6044–6051.

VITA